



## **University of Huddersfield Repository**

Allen, Charlotte E.

A systematic study of the corrosion layers on excavated coins from varying historical periods

### **Original Citation**

Allen, Charlotte E. (2016) A systematic study of the corrosion layers on excavated coins from varying historical periods. Masters thesis, University of Huddersfield.

This version is available at <http://eprints.hud.ac.uk/id/eprint/30281/>

The University Repository is a digital collection of the research output of the University, available on Open Access. Copyright and Moral Rights for the items on this site are retained by the individual author and/or other copyright owners. Users may access full items free of charge; copies of full text items generally can be reproduced, displayed or performed and given to third parties in any format or medium for personal research or study, educational or not-for-profit purposes without prior permission or charge, provided:

- The authors, title and full bibliographic details is credited in any copy;
- A hyperlink and/or URL is included for the original metadata page; and
- The content is not changed in any way.

For more information, including our policy and submission procedure, please contact the Repository Team at: [E.mailbox@hud.ac.uk](mailto:E.mailbox@hud.ac.uk).

<http://eprints.hud.ac.uk/>

**A SYSTEMATIC STUDY OF THE CORROSION  
LAYERS ON EXCAVATED COINS FROM VARYING  
HISTORICAL PERIODS**

**CHARLOTTE ELIZABETH ALLEN**

A thesis submitted to the University of Huddersfield in partial fulfilment of the requirements  
for the degree of Master of Science by Research

The University of Huddersfield

January 2016

#### Copyright statement

- i. The author of this thesis (including any appendices and/or schedules to this thesis) owns any copyright in it (the "Copyright") and s/he has given The University of Huddersfield the right to use such copyright for any administrative, promotional, educational and/or teaching purposes.
- ii. Copies of this thesis, either in full or in extracts, may be made only in accordance with the regulations of the University Library. Details of these regulations may be obtained from the Librarian. This page must form part of any such copies made.
- iii. The ownership of any patents, designs, trademarks and any and all other intellectual property rights except for the Copyright (the "Intellectual Property Rights") and any reproductions of copyright works, for example graphs and tables ("Reproductions"), which may be described in this thesis, may not be owned by the author and may be owned by third parties. Such Intellectual Property Rights and Reproductions cannot and must not be made available for use without the prior written permission of the owner(s) of the relevant Intellectual Property Rights and/or Reproductions.

## **Abstract**

This research presents the results of a scientific study of archaeological copper and silver coins from three collections belonging to Roman, Medieval and Modern periods discovered in the UK. The morphology of the corrosion products was studied using Optical Microscopy (OM) and Scanning Electron Microscopy (SEM) to understand the formation of corrosion. Morphologically it was found that the surface corrosion of both metals was similar, a uniform layer of corrosion was identified with a general attack of the surface. Both copper and silver coins demonstrated a distinct layering with a metal core followed by an initial oxide layer and an external layer bearing soil markers and secondary corrosion products where present. X-ray diffraction, X-ray fluorescence and SEM-EDS were employed to characterise the corrosion products and determine the basic elemental composition of the corrosion layers. The study successfully identified the primary corrosion products present on the copper coins as copper, cuprite and quartz with the inclusion of other compounds such as kaolinite, cassiterite and malachite across some samples. Silver and Chlorargyrite were identified as the main components of all silver surfaces in the study with hexagonal silver oxide present in certain samples. The elemental composition, pH and texture of soil samples from the areas of excavation in Brough, Nottinghamshire, England were studied alongside the excavated coins and the direct influence the burial environment had on the corrosion process discussed. A novel technique in the field of corrosion studies on artefacts, Medium Energy Ion Scattering, was developed with the intention of attaining information about the structure and composition of the samples surface; preliminary results could only provide compositional information already attainable using existing techniques. This study provides valuable information to both scientists and conservators to maintain and protect archaeological objects; as well as providing significant information for corrosion science.

# Acknowledgements

There are several people to thank for their help and support throughout this thesis.

Firstly, I would like to thank Professor Sue Kilcoyne for her ongoing guidance and support throughout this process, from her assistance with XRF in the lab to data analysis and manipulation. She has been a pivotal part of my growth this past year; not only has she assisted me academically but she has been there for a chat and her support has enabled me to have faith in myself to tackle things I never thought I could.

I would also like to thank Reverend Dr Paul Wilcock for his guidance and support throughout and allowing me to have the opportunity to learn hands on about firearms and weapons throughout history – an absolutely fascinating experience I will never forget.

A special thanks goes to Andy Morris for his kind donations of coin samples and soil samples without which this thesis would literally not have been able to be written.

I would also like to thank Dr. Howard Williams for training me to use the SEM-EDS machine and for all his help when it was required, as well as Laura Thwaites for her training and help in using the XRD desktop diffractometer. Ibriham George, a special thanks for the training on the OM and for all your guidance and assistance in the lab. Thanks to Professor Jaap van den Berg for his expertise knowledge and assistance with the MEIS experiments and data analysis.

Samantha Rowe – thanks a million for your help with all things archaeological (and for the chats and brews)! Thanks to the guys in the office for making me laugh on a daily basis, and for all their help throughout the year.

Finally I would like to thank my family for being a constant support unit throughout not only this thesis but in everything I do.

# Table of Contents

Abstract .....	3
Acknowledgements .....	4
Table of Contents .....	5
List of Abbreviations.....	9
List of Figures .....	10
List of Tables.....	13
Chapter 1 - Aims.....	15
Chapter 2 - Introduction .....	16
2.1 The Interface of Science and Archaeology .....	16
2.1.1 The Importance of Artefact Analysis .....	16
2.2 An Introduction to the Study of Coins .....	17
2.3 Corrosion in coins.....	17
2.4 Corrosion formation.....	18
2.4.1 The Electrochemical nature of Corrosion.....	18
2.4.2 The burial corrosion mechanism.....	19
2.4.3 Corrosion cells .....	20
2.4.4 Predicting which corrosion products will form.....	21
2.4.5 Corrosion types.....	24
2.5 Copper corrosion .....	26
2.5.1 Copper oxide formation.....	26
2.5.2 Secondary corrosion product formation .....	27
2.6 Silver corrosion.....	29
2.6.1 Visual characterisation of silver corrosion .....	29
2.6.2 Corrosion products and mechanisms.....	29
2.7 Corrosion in alloys.....	31
Chapter 3 - Samples and Sites.....	32
3.1 Choice of materials for the study .....	32
3.1.1 Coin samples .....	32

3.1.2	Soil samples .....	34
3.2	Background of the areas in the study .....	35
3.2.1	Roman finds .....	35
3.2.2	Medieval finds.....	37
3.2.3	Modern finds .....	38
Chapter 4 -	Methodology.....	40
4.1	X-ray Diffraction .....	40
4.2	X-ray Fluorescence .....	41
4.3	SEM-EDS.....	42
4.4	Optical Microscopy.....	43
4.5	MEIS .....	43
4.5.1	Chemical etching procedure.....	43
4.5.2	Experimental analysis and parameters.....	43
4.6	Soil analysis .....	45
4.6.1	Visual analysis procedure .....	45
4.6.2	pH analysis procedure.....	46
Chapter 5 -	Copper Coinage Results .....	47
5.1	Copper Coinage corrosion with adhering soil samples.....	48
5.1.1	Burial environment D.....	48
5.1.2	Modern coin - Coin D .....	51
5.1.3	Conclusion of the burial environment's influence on the corrosion products ..	57
5.2	Primary copper corrosion products .....	59
5.2.1	Identification .....	59
5.2.2	Results from XRF analysis .....	60
5.2.3	Visual characterisation .....	61
5.2.4	SEM-EDS results .....	62
5.2.5	XRD results .....	65
5.2.6	Conclusion .....	66
5.3	Secondary copper corrosion products.....	67
5.3.1	Identification .....	67
5.3.2	Results from XRF analysis .....	68

5.3.3	Visual characterisation .....	69
5.3.4	SEM-EDS results .....	70
5.3.5	XRD results .....	72
5.3.6	Conclusion .....	73
5.4	Summary of Copper Coinage Results .....	74
Chapter 6 -	Silver Coinage Results .....	76
6.1	Silver Coinage corrosion with adhering soil samples.....	77
6.1.1	Burial environment A.....	77
6.1.2	Roman coin - Coin B.....	80
6.1.3	Conclusion of the burial environment's influence on the corrosion products ..	87
6.2	Silver Coinage corrosion.....	89
6.2.1	Identification .....	89
6.2.2	XRF analysis results.....	90
6.2.3	Visual characterisation .....	91
6.2.4	SEM-EDS results .....	92
6.2.5	XRD results .....	95
6.2.6	Conclusion .....	95
6.3	Silver alloy Coinage corrosion .....	97
6.3.1	Identification .....	97
6.3.2	XRF analysis results.....	98
6.3.3	Visual characterisation .....	99
6.3.4	SEM-EDS results .....	101
6.3.5	XRD results .....	104
6.3.6	Conclusion .....	105
6.4	Summary of Silver Coinage Results .....	106
Chapter 7 -	MEIS analysis .....	108
7.1	Copper coinage .....	108
7.2	Silver coinage .....	110
7.3	Conclusion of MEIS studies .....	112
Chapter 8 -	Conclusion .....	113
8.1	Future Work .....	115



References.....	117
Appendices .....	121
Appendix A - Principles of techniques .....	123
Appendix B - Derivation of the Kinematic factor.....	127
Appendix C - Averaging and error equations .....	130
Appendix D - Raw soil sample data, average and error calculations.....	131
Appendix E - Raw XRF data, average and error calculations .....	133
Appendix F - Results pages .....	160

Word Count: 27,228

## **List of Abbreviations**

EDS	Energy Dispersive X-ray Spectroscopy
IIAA	International Institute for Accelerator Applications
MEIS	Medium Energy Ion Scattering
OM	Optical Microscopy
SEM	Scanning Electron Microscopy
SEM-EDS	Scanning Electron Microscopy in combination with Energy Dispersive X-ray Spectroscopy
UHV	Ultra-high Vacuum
XRD	X-ray Diffraction
XRF	X-ray Fluorescence

## List of Figures

Figure 2.1: Corrosion cell in action.....	18
Figure 2.2: Galvanic series in seawater .....	20
Figure 2.3: Potential v. pH for the decomposition of water .....	22
Figure 2.4: Pourbaix diagram for the corrosion of iron in water .....	23
Figure 2.5: Schematic summary of some forms of corrosion expected on buried metal artefacts .....	24
Figure 2.6: Variations in the shape of pits.....	25
Figure 3.1: OM images of all the coin samples in the study .....	32
Figure 3.2: Map indicating the location of the soil samples.....	34
Figure 3.3: Magic Map indicating the location of the Roman Settlement Crocalana and the Fosse Way .....	36
Figure 3.4: Google Earth Map showing the location of the Roman Settlement Crocalana and the Fosse Way .....	36
Figure 3.5: Magic Map indicating the location of the Medieval village of Langford .....	37
Figure 3.6: Google Earth Map showing the location of the Medieval village of Langford.....	38
Figure 3.7: Google Earth Map indicating the location of all coin samples .....	39
Figure 3.8: Google Earth Map indicating the location of the coin samples densely populated in Nottinghamshire.....	39
Figure 4.1: Procedure for determining the texture of a soil matrix .....	45
Figure 5.1: XRF pattern of soil D .....	48
Figure 5.2: XRD pattern of soil D .....	49
Figure 5.3: Stability diagram for copper .....	51
Figure 5.4: OM image of the obverse of coin D, x50 magnification .....	52, 54
Figure 5.5: OM image of the reverse of coin D, x50 magnification.....	52
Figure 5.6: Photograph of the obverse of coin D .....	54
Figure 5.7: SEM image of area 1 on the obverse of coin D demonstrating site 3 of analysis .. .....	55
Figure 5.8: SEM image of area 1 on the reverse of coin D demonstrating site 1 of analysis ... .....	55
Figure 5.9: SEM image of area 1 on the reverse of coin D demonstrating site 2 of analysis ... .....	56
Figure 5.10: XRD pattern of the reverse of coin D.....	57
Figure 5.11: OM image of the obverse of coin R06, x50 magnification .....	59, 61
Figure 5.12: OM image of the reverse of coin R06, x50 magnification .....	59, 61
Figure 5.13: Photograph of the obverse of R06 .....	61
Figure 5.14: Photograph of the reverse of R06 .....	61

Figure 5.15: SEM image of area 3 on the reverse of R06 demonstrating site 3 of analysis ....	62
Figure 5.16: SEM image of area 3 on the reverse of R06 demonstrating site 2 of analysis ....	63
Figure 5.17: SEM image of area 2 on the reverse of R06 demonstrating site 1 of analysis ....	64
Figure 5.18: XRD pattern of the obverse of coin R06.....	65
Figure 5.19: OM image of the obverse of coin R02, x50 magnification .....	67, 69
Figure 5.20: OM image of the reverse of coin R02, x30 magnification .....	67, 69
Figure 5.21: Photograph of the obverse of R02 .....	69
Figure 5.22: Photograph of the reverse of R02 .....	69
Figure 5.23: SEM image of area 4 on the reverse of R02 demonstrating site 1 of analysis ....	70
Figure 5.24: SEM image of area 4 on the reverse of R02 demonstrating site 2 of analysis ....	71
Figure 5.25: SEM image of area 2 on the obverse of R02 demonstrating site 3 of analysis....	71
Figure 5.26: SEM image of area 2 on the obverse of R02 demonstrating site 1 of analysis....	72
Figure 5.27: XRD pattern of the obverse of coin R02.....	72
Figure 6.1: XRF pattern of soil A .....	77
Figure 6.2: XRD pattern of soil A .....	78
Figure 6.3: Stability diagram for silver in seawater at varying reduced sulfur concentrations .....	79
Figure 6.4: OM image of the obverse of coin B, x50 magnification .....	80, 82
Figure 6.5: OM image of the reverse of coin B, x50 magnification .....	80
Figure 6.6: Photograph of the obverse of coin B .....	82
Figure 6.7: SEM image of area 3 on the reverse of coin B demonstrating site 1 of analysis ...	83
Figure 6.8: SEM image of area 3 on the reverse of coin B demonstrating site 2 of analysis ...	84
Figure 6.9: SEM image of area 2 on the reverse of coin B demonstrating site 1 of analysis ...	84
Figure 6.10: SEM image of area 2 on the obverse of coin B demonstrating analysis of site 3.	85
Figure 6.11: XRD pattern of the reverse of coin B.....	86
Figure 6.12: XRD pattern of the reverse of coin B showing lattice spacings .....	86
Figure 6.13: XRD pattern of Ag and AgCl nanoparticles .....	87
Figure 6.14: OM image of the obverse of coin M516, x50 magnification.....	89, 91

Figure 6.15: OM image of the reverse of coin M516, x50 magnification .....	89, 91
Figure 6.16: Photograph of the obverse of M516 .....	91
Figure 6.17: SEM image of area 1 on the obverse of M516 demonstrating site 1 of analysis.. .....	92
Figure 6.18: SEM image of area 1 on the obverse of M516 demonstrating site 3 of analysis.. .....	92
Figure 6.19: SEM image of area 3 on the reverse of M516 demonstrating site 1 of analysis.. .....	93
Figure 6.20: SEM image of area 3 on the reverse of M516 demonstrating site 2 of analysis.. .....	94
Figure 6.21: XRD pattern of the reverse of coin M516 .....	95
Figure 6.22: OM image of the obverse of coin V106, x50 magnification .....	97, 99
Figure 6.23: Image of the obverse of a George V Sixpence minted in 1934.....	97
Figure 6.24: OM image of the reverse of coin V106, x50 magnification.....	98, 100
Figure 6.25: Image of the reverse of a George V Sixpence minted in 1934 .....	98
Figure 6.26: Photograph of the obverse of V106.....	99
Figure 6.27: OM image of the black lumpy corrosion localised on the nose on the obverse of V106, x50 magnification .....	100
Figure 6.28: OM image of the cream corrosion near the lettering on the obverse of V106, x50 magnification .....	100
Figure 6.29: Photograph of the reverse of V106 .....	100
Figure 6.30: OM image of the brown lumps present on the acorn on the reverse of V106, x100 magnification.....	101
Figure 6.31: OM image of the cream sandy corrosion product on the reverse of V106, x100 magnification .....	101
Figure 6.32: SEM image of area 2 of the reverse of V106 .....	101
Figure 6.33: SEM image of area 3 of the obverse of V106.....	101
Figure 6.34: SEM image of area 2 on the reverse of V106 demonstrating site 1 of analysis.. .....	102
Figure 6.35: SEM image of area 2 on the reverse of V106 demonstrating site 2 of analysis.. .....	102
Figure 6.36: SEM image of area 3 of obverse of V106 demonstrating site 1 of analysis .....	103
Figure 6.37: SEM image of area 3 of obverse of V106 demonstrating site 2 of analysis .....	103
Figure 6.38: XRD pattern of the reverse of coin V106 .....	104
Figure 7.1: MEIS spectrum of coin V112.....	108
Figure 7.2: Higher energy part of the MEIS spectrum of coin V112 .....	110
Figure 7.3: MEIS spectrum of coin M804 .....	111

## List of Tables

Table 3.1: Highest and lowest units recorded in each month for the specified climate period from the Met office .....	35
Table 4.1: Diagnostic reflections and intensities for the crystalline corrosion product constituents of the patinas in this study .....	40
Table 4.2: Characteristic X-rays of elements graphically represented throughout this study ..	41
Table 4.3: Characteristic X-rays of elements lighter than Na .....	42
Table 4.4: Energies of the elements studied for identification from signals in the MEIS spectra .....	45
Table 5.1: Visual analysis of soil D.....	48
Table 5.2: pH measurements for soil D .....	48
Table 5.3: XRF Elemental Composition of soil D.....	48
Table 5.4: Average XRF Elemental Composition of green areas on coin D .....	53
Table 5.5: Average XRF Elemental Composition of orange areas on coin D.....	53
Table 5.6: SEM-EDS Elemental Composition of site 3 on area 1 of the obverse of coin D ...	55
Table 5.7: SEM-EDS Elemental Composition of site 1 on area 1 of the reverse of coin D ....	55
Table 5.8: SEM-EDS Elemental Composition of site 2 on area 1 of the reverse of coin D ....	56
Table 5.9: Average XRF Elemental Composition of metal areas on R06 .....	60
Table 5.10: Average XRF Elemental Composition of green areas on R06 .....	60
Table 5.11: SEM-EDS Elemental Composition of site 3 on area 3 of the reverse of R06 ....	62
Table 5.12: SEM-EDS Elemental Composition of site 2 on area 3 of the reverse of R06 ....	63
Table 5.13: SEM-EDS Elemental Composition of site 1 on area 2 of the reverse of R06 ....	64
Table 5.14: Average XRF Elemental Composition of green areas on R02.....	68
Table 5.15: Average XRF Elemental Composition of orange crust on R02.....	68
Table 5.16: SEM-EDS Elemental Composition of site 1 on area 4 of the reverse of R02 .....	70
Table 5.17: SEM-EDS Elemental Composition of site 2 on area 4 of the reverse of R02 .....	71
Table 5.18: SEM-EDS Elemental Composition of site 3 on area 2 of the obverse of R02 .....	71
Table 5.19: SEM-EDS Elemental Composition of site 1 on area 2 of the obverse of R02 .....	72
Table 5.20: Summary of composition and corrosion products of all copper coins in the study .....	74
Table 6.1: Visual analysis of soil A.....	77
Table 6.2: pH measurements for soil A.....	77
Table 6.3: XRF Elemental Composition of soil A.....	77
Table 6.4: Average XRF Elemental Composition of metal areas on coin B.....	81
Table 6.5: Average XRF Elemental Composition of dark grey areas on coin B .....	81
Table 6.6: SEM-EDS Elemental Composition of site 1 on area 3 of the reverse of coin B ....	83

Table 6.7: SEM-EDS Elemental Composition of site 2 on area 3 of the reverse of coin B ....	84
Table 6.8: SEM-EDS Elemental Composition of site 1 on area 2 of the reverse of coin B ....	84
Table 6.9: SEM-EDS Elemental Composition of site 3 on area 2 of the obverse of coin B....	85
Table 6.10: Average XRF Elemental Composition of cream areas on M516 .....	90
Table 6.11: Average XRF Elemental Composition of light grey/brown areas on M516 .....	90
Table 6.12: SEM-EDS Elemental Composition of site 1 on area 1 of the obverse of M516...	92
Table 6.13: SEM-EDS Elemental Composition of site 3 on area 1 of the obverse of M516...	92
Table 6.14: SEM-EDS Elemental Composition of site 1 on area 3 of the reverse of M516 ...	93
Table 6.15: SEM-EDS Elemental Composition of site 2 on area 3 of the reverse of M516 ...	94
Table 6.16: Average XRF Elemental Composition of metal areas on V106 .....	98
Table 6.17: Average XRF Elemental Composition of green areas on V106 .....	98
Table 6.18: SEM-EDS Elemental Composition of site 1 on area 2 of the reverse of V106.....	102
Table 6.19: SEM-EDS Elemental Composition of site 2 on area 2 of the reverse of V106.....	102
Table 6.20: SEM-EDS Elemental Composition of site 1 on area 3 of the obverse of V106 .....	103
Table 6.21: SEM-EDS Elemental Composition of site 2 on area 3 of the obverse of V106 .....	103
Table 6.22: Summary of composition and corrosion products of all silver coins in the study	106
Table 7.1: Average XRF Elemental Composition of multi-coloured corrosion on V112 .....	109
Table 7.2: Average XRF Elemental Composition of metal areas on M804.....	111

## **Chapter 1 - Aims**

The aim of this research is to study in detail the nature and morphology of corrosion products present on the surface of excavated copper and silver coins from varying historical periods in order to aid future conservation and preservation. The elemental composition of the corrosion products will be established using known techniques X-ray Fluorescence (XRF) and Scanning Electron Microscopy with Energy Dispersive X-ray Spectroscopy (SEM-EDS) with the identification of the exact corrosion products present on the surface determined by X-ray diffraction (XRD). The surface morphology will be studied with the use of SEM-EDS to understand the corrosion process and features of corrosion on buried metal. Optical Microscopy (OM) will play a major part in identifying the heritage of the coins as well as visualising the corrosion and mineral stratum present on the surface. The elemental composition, pH and texture of soil samples from the areas of excavation will be studied alongside the excavated coins in order to see the influence the burial environment has on the corrosion process. A novel technique in the field of corrosion studies on artefacts, Medium Energy Ion Scattering (MEIS) will be applied to obtain information about the structure and composition of the samples surface.



## **Chapter 2 - Introduction**

### **2.1 The Interface of Science and Archaeology**

Archaeology is a discipline that creates the chronological image of human evolution [1] from the perspective of economy, social life and interactions between civilisations evidenced in archaeological artefacts [2]. Artefacts may be subject to alteration once buried and a full characterisation of this alteration is required to interpret the present state of degradation for conservation purposes, as well as for their historical cultural heritage. To extract the maximum information from the archaeological objects a combination of analytical techniques is vital to give a full detailed account of the constituents of the artefacts. Analysis addresses questions directly related to archaeological interpretation allowing conclusions to be drawn about the life of the objects, as well as answering indirect questions critical in understanding the processes that acted upon the artefact in burial and the materials within [1, 3].

#### **2.1.1 The Importance of Artefact Analysis**

Archaeological artefacts are anything (created, used or manipulated by humans) that have a cultural significance ranging from stone tools to weapons to personal adornments. However in this report only the corrosion of metallic artefacts will be studied. Detailed studies of artefact degradation provides information for both scientists and conservators in and enables them to control and stop deterioration of ancient and historical metals in museums, and to select the ideal storage conditions to preserve them. The interface between science and conservation is of the utmost importance and is an area that is constantly expanding [3, 4].

The British Museum has been carrying out collaborative conservation research with scientists and conservators since 1919, and by doing so has contributed to the long term preservation of collections within the museum. One preventative conservation technique the museum has developed is the prevention of bronze disease in copper alloys achieved by controlling humidity levels to below 40%. Initially excavated copper alloys were stabilised by the removal of the corrosion layers through soaking or stripping. Controlling humidity meant that any nantokite present in the patina was unable to form paratacamite using moisture from the air, which if transpires leads to the ultimate destruction of the artefacts as bronze disease [5].

These, and other strategies are still in use today in museums [6]. The environment of the storage units is a major factor in controlling deterioration as storing objects is seen to physically protect them yet storage may harm the object or even catalyse corrosion further [7]. The British Museum developed an accelerated corrosion test in 1972 that screened

materials used for display to see if they were suitable for long term use and if the material would cause the object any further degradation. Within the museum all materials applied for storage have to pass this test which has made a huge impact towards stabilising and protecting collections [7]. These examples illustrate the significant input the scientist can provide to archaeology.

## **2.2 An Introduction to the Study of Coins**

Coins have been used for thousands of years, although the details of their invention is open to debate. Herodotus reported that the Lydians were the first to produce coins in approximately the 6<sup>th</sup> century BC; while the record of the Arundelian marbles states that Phido the Argive first struck silver coins in Aegina, Greece around the 5<sup>th</sup>-6<sup>th</sup> centuries BC [8, 9]. Generally the tradition of coinage is reported as a Greek one due to the earliest archaeological context of coinage coming from the Greek city of Ephesos. However it is important to acknowledge that coinage developed where Lydian and Greek cultures interacted and was not necessarily a 'Greek invention' [10].

The earliest coins (of 560BC [10]) found at the temple of Artemis at Ephesos were of electrum; a natural gold-silver alloy with trace amounts of other metals. These electrum coins were made to a weighed standard, some were marked and others unmarked. They were replaced with gold and silver coins in Lydia in the second half of the 6<sup>th</sup> century BC [9], the Persians also produced gold and silver coins and Greek cities started to produce silver exclusively. A tradition from North Etruscan emerged where a base metal (usually bronze) by weight was used for money; the Romans continued this tradition with slight modifications. Athens, Greece and many civilisations adopted bronze coinage while gold, silver and electrum were still being used [10]. Several different metals and metal alloys have been used throughout history to make coins, with modern coins in the United Kingdom also being made from differing alloys, the composition of which has been altered on various occasions by the Royal Mint (the body that controls the manufacture of coins in the UK) [11].

## **2.3 Corrosion in coins**

Ultimately the identification of ancient coins reveals their age and assists in dating historical events. Buried coins deteriorate via differing corrosion processes which will alter their appearance, structure and nature so much so that sometimes it is almost impossible to use them as historical evidence of previous social and economic activity. In some instances the corrosion that transpires may completely destroy the items, explaining why raw data collected on excavated coins such as weight, diameter and composition cannot be used for direct comparison. Studies are constantly being undertaken on the corrosion of coins retrieved from excavations to provide useful information on the corrosive media and corrosion processes for corrosion science and the conservation and preservation of

archaeological objects [12]. Not only is it important to study the finds themselves, it is also useful to study the soils and sediments of the archaeological deposit to provide evidence or context to the finds [1].

## 2.4 Corrosion formation

### 2.4.1 The Electrochemical nature of Corrosion

Corrosion is the spontaneous oxidation of metals usually by atmospheric oxygen, however water or atmospheric pollutants such as SO<sub>2</sub> can contribute [13]. Metallic corrosion processes are electrochemical involving electron transfer in an aqueous solution; therefore for corrosion to take place a corrosion cell is required. The corrosion cell consists of an anode where oxidation takes place, making this the positive more reactive electrode; a cathode where reduction takes place, the negative electrode; an electrolyte and a metallic path as shown below in figure 2.1. Corrosion takes place at the metal-solution interface providing the electrolyte and the creation of cathodic and anodic sites on the metals surface [14].

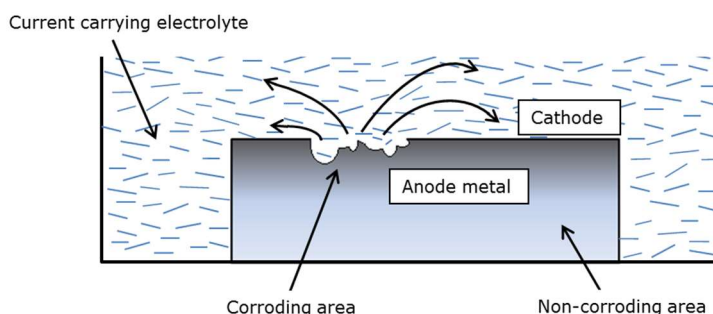
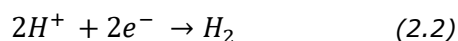


Figure 2.1: Corrosion cell in action adapted from p.10 [15]

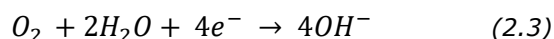
Metal is lost at the anode as metal ions enter the solution with electron transfer taking place simultaneously, the cathode then consumes these electrons as they move via a metallic path due to their insolubility in solution. An electrolyte is necessary to allow the current (in the form of positive ions) to flow from the anode to the cathode, with the flow of electrons in the opposite direction completing the circuit. The basic oxidation reaction that is required for corrosion is represented by the anodic reaction below:



where M represents the metal. The metal ions produced in the reaction will either form dissolved species, remaining as  $M^{n+}$ , or solid corrosion products. The cathode supplies the reduction reactions to support the anodic dissolution of metal, corrosion itself does not occur here [15]. There are only a few reduction reactions significant in corrosion, the simplest and most common of which is the reduction of hydrogen ions in acidic conditions:



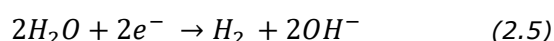
Another cathodic reaction coupled with metal oxidation is the reduction of dissolved oxygen observed most commonly in neutral and alkaline solutions exposed to ambient air:



The reduction of oxygen in acid solution exposed to ambient air is as follows:



Water may also be reduced by:



which is equivalent to (2.2), assuming that water dissociates into  $H^+$  and  $OH^-$  and the resulting equation is simplified [16].

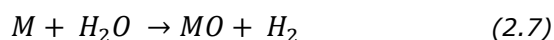
### **2.4.2 The burial corrosion mechanism**

An initial oxide layer will form on a coin gradually over time prior to burial, with the oxygen in the soil providing this layer if the reaction did not take place before burial. The burial corrosion mechanism begins with the leaching out or migration of certain metal ions from the alloy into the surface layer [12] with the metal-corrosion interface facilitating this anodic dissolution of the metal. The reduction of oxygen is conducted at the outermost electrically conducting material; in a copper containing alloy where cuprite ( $Cu_2O$ ) has already formed this would allow the cathodic reactions to ensue [14]. The probable reactions to take place when a metal reacts with oxygen and water are as follows.

Metal and oxygen:

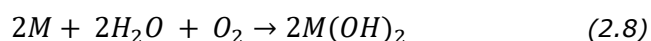


Metal and water:



The evolution of hydrogen gas as shown in equation 2.7 is highly unlikely unless the metal is very reactive or an acid is present.

Metal and oxygenated water:



In reaction (2.8) a corrosion product other than a metal oxide is formed that is likely to be powdery by nature rather than protective [17].

The oxidised surface layer of the metal is porous enabling the movement of water and the activity of corrosive ions from the soil, such as Cl, O and S which are key to the artefacts

continued corrosion upon burial over a lengthy time period [12]. The anodic regions become acidified with the metal ions concentrating and undergoing hydrolysis leading to alterations in pH at this site as well as the separated cathodic site [14, 18]. The diffusion of anions from the soil maintains electrical neutrality balancing the charge of the positive metal ions. At the anodic sites chloride ions tend to accumulate as they are the most common environmental anion and have a high mobility. The process of metal dissolution at the anodic region is continual; the chloride ions accumulate as the metal corrodes further with the addition of an increased concentration of hydrogen ions causing localised attack at this site. Within a pit or crevice, anodic dissolution of the metal is accelerated by hydrogen and chloride ions in the same manner [14].

### 2.4.3 Corrosion cells

Several different types of corrosion cell exist, one of these being an electrolytic cell that requires an external current introduced into the system. A differential temperature cell is another cell that requires two drastically different temperatures to form an anode and cathode. It is safe to assume that neither of these operate in buried metallic artefacts.

A galvanic cell relies on anodes and cathodes of dissimilar metals or the same metals in dissimilar conditions in the same conducting electrolyte. In this corrosion cell one of the metals (the more active) is preferentially corroded over the other metal (the more noble), with respect to the galvanic series as represented in figure 2.2

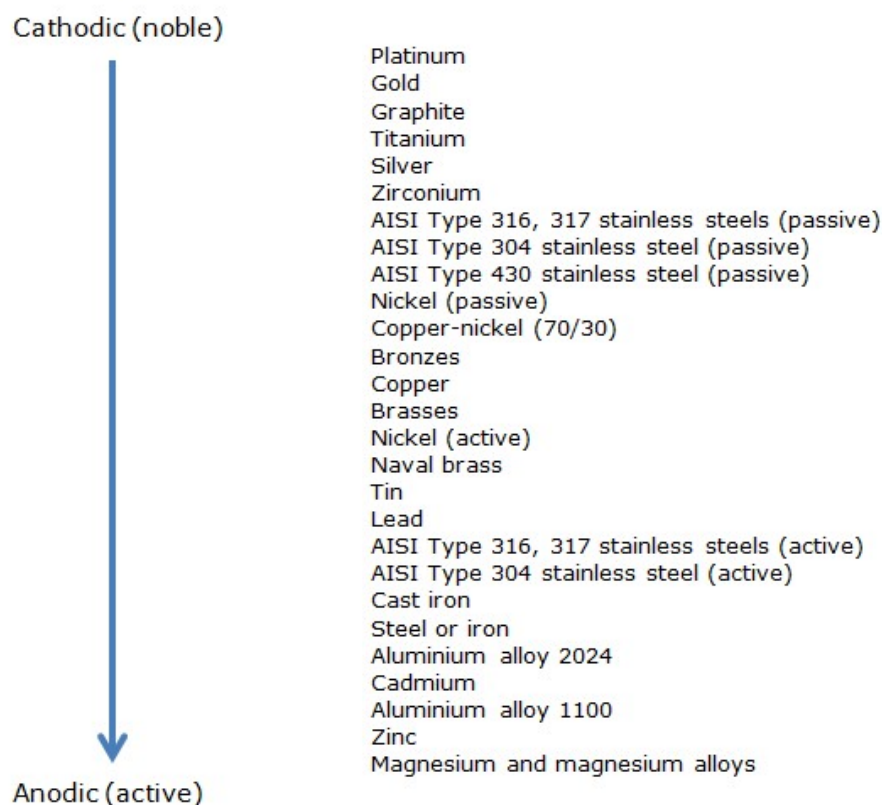


Figure 2.2: Galvanic series in seawater adapted from p.14 [16]

This type of corrosion cell could be present in a metallic artefact made of an alloy where two different metals are present.

A concentration cell is similar to a galvanic cell, except that the anode and cathode are made of the same metal and the electrolyte has different concentrations. The majority of natural corrosion would be from a concentration cell as such, as these are commonly observed in underground corrosion. The factors that influence a concentration cell could be the varying amount of oxygen, the differing moisture content or the compositional differences of the soil. It is the variation in one of these factors that creates a potential difference establishing an anode in an area of high concentration and a cathode in an area of low concentration [15]. The exact mechanism that operates in the corrosion of buried metallic artefacts is difficult to pin point as there are several key influential factors in operation. A concentration cell is the more likely set up as a galvanic cell requires the electrolyte to be homogeneous, and the natural soil environment is extremely diverse.

#### ***2.4.4 Predicting which corrosion products will form***

Ultimately, the corrosion cell in operation and the types of corrosion products formed, rely on the thermodynamically most stable products in the burial environment. Corrosion is only possible in areas where soluble metal ions are stable, in order for these ions to react to form corrosion products. Generally the most stable products depend on the standard reduction potentials of  $M^{n+}$ ,  $O_2$  and water; the pH; the partial pressure of  $O_2$  and the temperature [13].

As well as these factors influencing the rate of corrosion, the burial environment has a large impact. In dry soil, corrosion rates of metal are negligible but as the moisture content rises the corrosion rate is controlled mainly by the diffusion of dissolved oxygen in water found in the soil [16]. The rate of corrosion is also affected by the conductivity, aggressive ion concentration, biological activity and pH of the soil. The nature of the soil, whether this is sand, silt or clay and the different influencing factors mentioned above vary considerably. The mineral content of soil and consequently any ions present greatly influence the conductivity and pH of the environment. The corrosivity of the soil environment is also effected by addition of chemicals such as fertilisers [19].

The stability of water undergoing electrolysis in the soil is key in determining the corrosion processes course. Without the supporting cathodic reactions of water and oxygen the corrosion cell would be obsolete. The acidity of the solution determines the voltage over which water is thermodynamically stable, with alterations in pH directly influencing changes in corrosion products. Pourbaix represented the influence pH has on corrosion products diagrammatically, by relating the pH of the solution to the systems electrode potential (eg.

figures 2.3 & 2.4). Electrode potential measures the oxidising or reducing power of the metal-solution interface; the more negative the conditions the more reducing and vice versa. Pourbaix diagrams indicate three important regions; immunity, passivation and corrosion. The region of corrosion is where the metal is transformed into a soluble species and this usually takes place under acidic conditions. The passivation area tends to occur under alkaline and oxidising conditions (high electrode potential), with the area of immunity being found under reducing conditions (low electrode potential) [20]. The Pourbaix diagrams below are those of the decomposition of water, showing the regions of stability for itself and its decomposition products; and the corrosion of iron showing the three regions of corrosion, passivation and immunity.

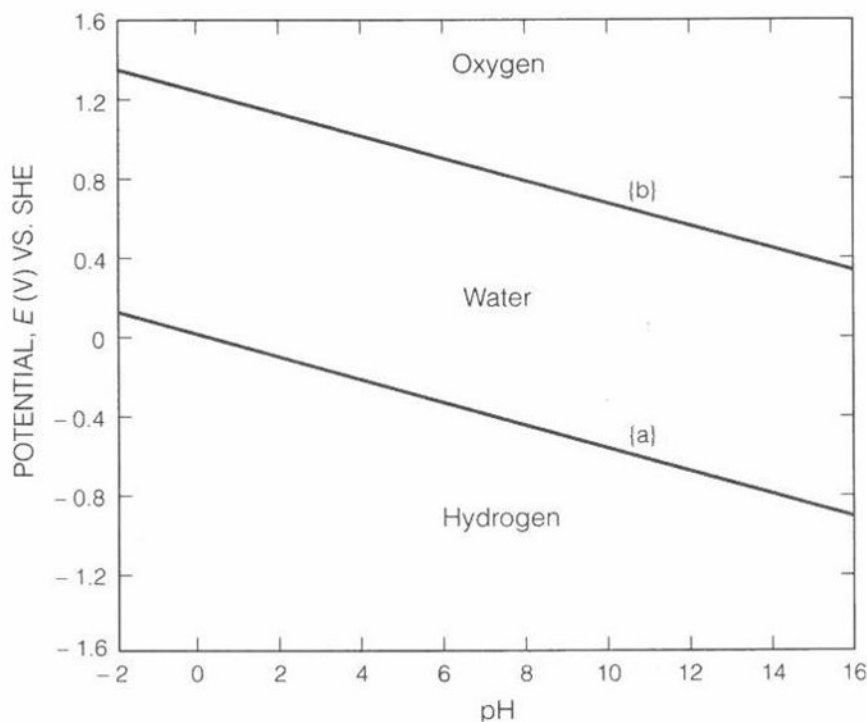
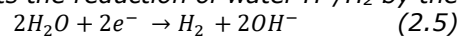
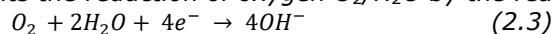


Figure 2.3: Potential v. pH for the decomposition of water p.51 [16]

Where {a} represents the reduction of water  $H^+/H_2$  by the reaction mechanism:



and {b} represents the reduction of oxygen  $O_2/H_2O$  by the reaction mechanism:



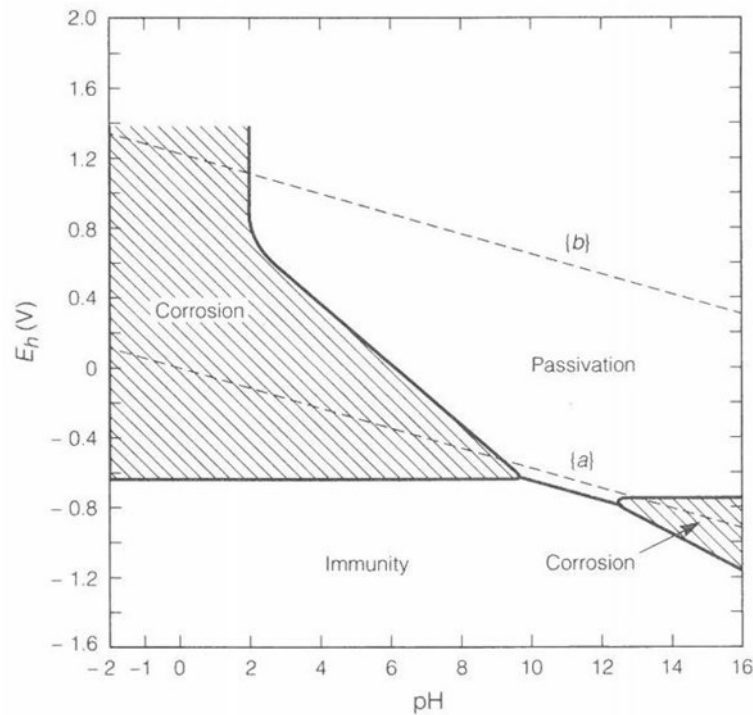


Figure 2.4: Pourbaix diagram for the corrosion of iron in water p.53 [16]

As seen in figure 2.3 below line {a} water is unstable and decomposes to  $H_2$ , above the line water is stable and any hydrogen gas present is oxidized to  $H^+$  or  $H_2O$ . At positive potentials above line {b} water is unstable and oxidises to  $O_2$ , below line {b} water is stable and dissolved oxygen is reduced to water if present. Thus helping to explain what cathodic reactions will take place at a certain pH and potential to yield certain corrosion products [16].

Predicting which corrosion products will be present during burial even with the help of Pourbaix diagrams is difficult as there are several factors influencing what will form. It is a combination of all the factors discussed that ultimately lead to the oxidation of a certain metal in an alloy and therefore the most thermodynamically stable products being made.



### 2.4.5 Corrosion types

There are eight major corrosion types that describe the mechanisms taking place in buried environments on metal. The forms can be identified by visual observation and are pictured schematically below in figure 2.5.

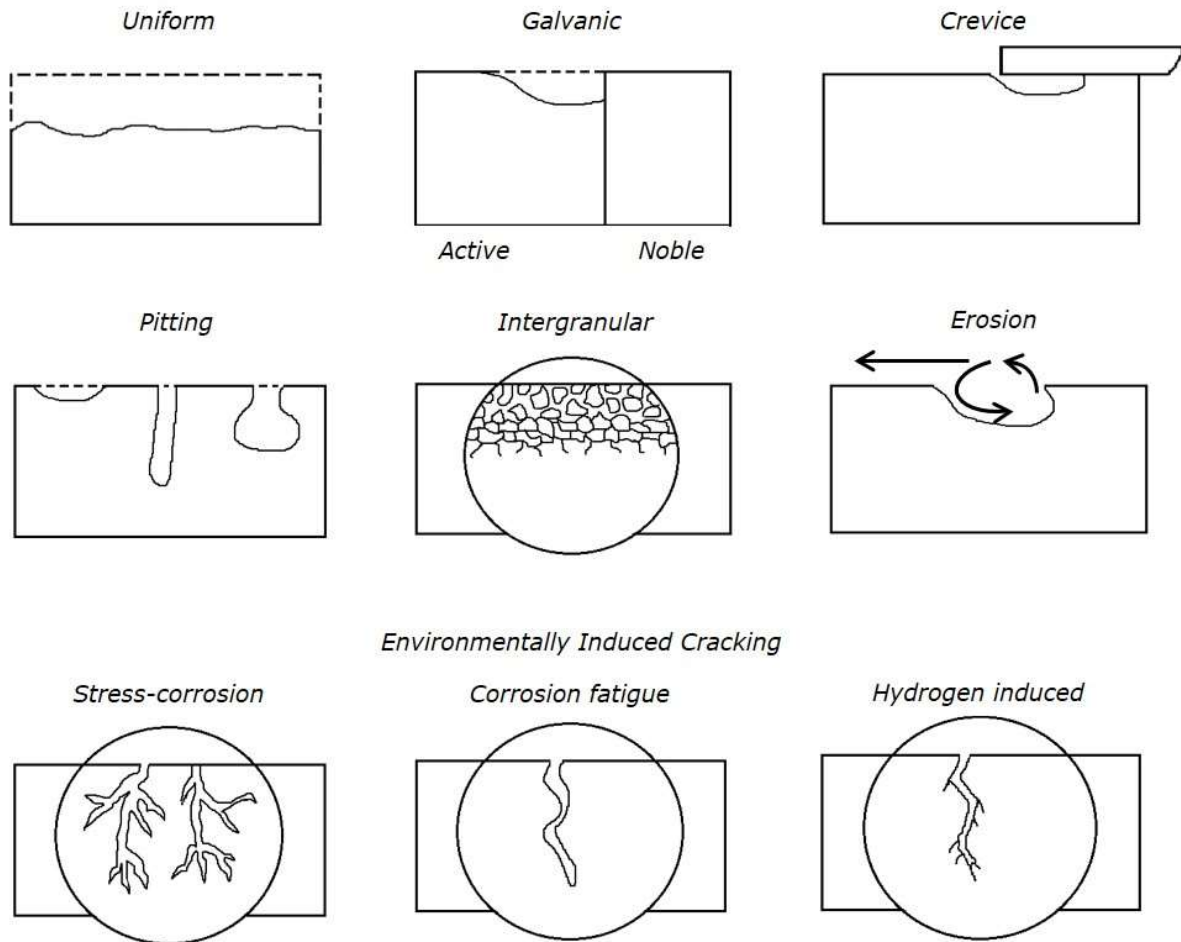
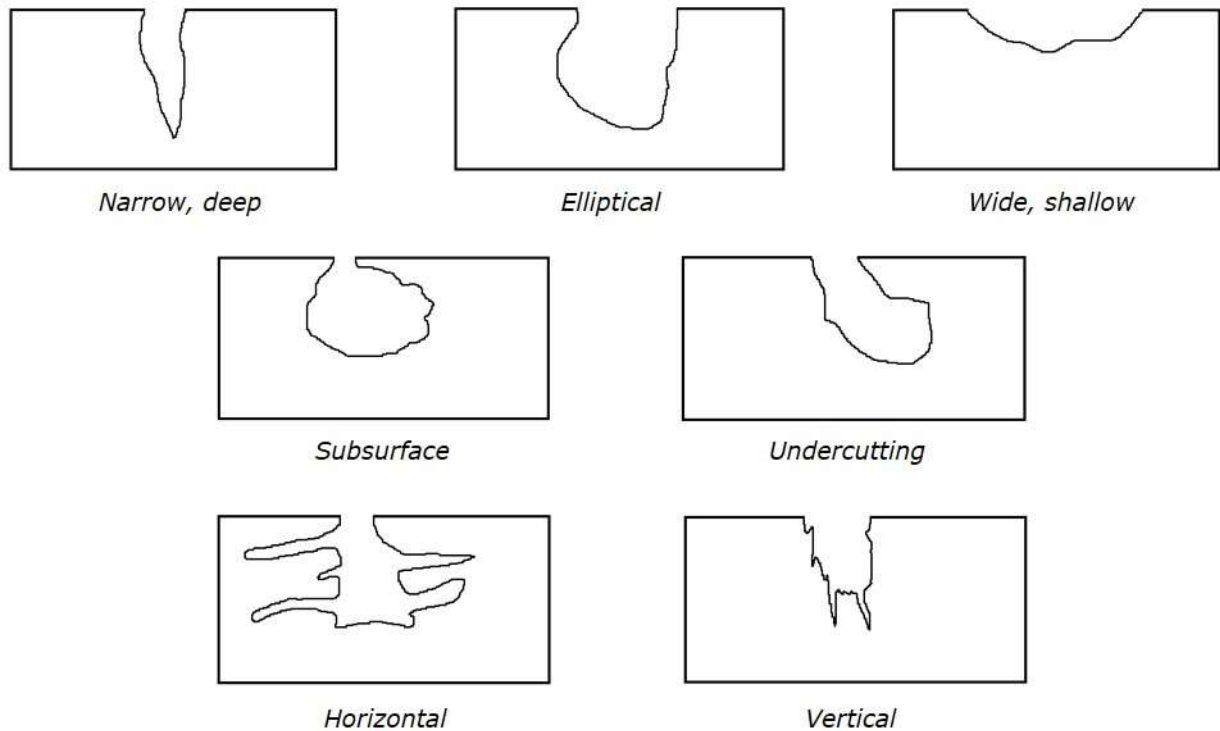


Figure 2.5: Schematic summary of some forms of corrosion expected on buried metal artefacts adapted from p.10 [16]

Uniform corrosion or general attack is a continuous form of corrosion that removes the metal from the entire surface area in a uniform manner and usually does not penetrate into the bulk. It is the most common corrosion type with the visible aspects of it shown above in figure 2.5. Galvanic corrosion takes place when a potential difference develops between two dissimilar metals in a conductive solution.

When a corrosive material or insoluble solid comes into contact with an object's surface a crevice may be created. This crevice creates a small sheltered volume where intense localised corrosion occurs. Another localised attack that occurs in a similar manner is pitting corrosion. Both corrosion types arise due to the isolation of the anode in the crevice/pit with the surrounding surface acting as the cathode. Pitting corrosion results from a 'puncture' in

the passive film; the pits produced vary in morphology with some of the common types shown below in figure 2.6:



*Figure 2.6: Variations in the shape of pits adapted from p.201 [16]*

Intergranular corrosion is the result of localised attack at the grain boundaries and adjacent regions due to the segregation of impurities or passive elements at the grain boundaries decreasing.

If the corrosive fluid flows rapidly it will physically erode the surface removing any passive corrosion layer to expose the metal underneath thus accelerating corrosion. Erosion corrosion is relatively easy to visually characterise by grooves, waves or valleys, where the formation of these follow the direction of the fluid flow.

Environmental cracking is where a brittle fracture occurs in a material that is usually ductile due to the corrosive environment. Environmental cracking includes: stress-corrosion cracking, where a static tensile strength is present in a specific corrosive environment, corrosion fatigue cracking, under cyclic stress, and hydrogen induced cracking, where hydrogen in some form brings about internal cracks.

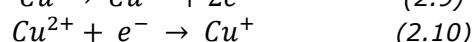
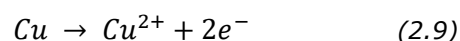
Another form of corrosion commonly observed is selective leaching (de-alloying) where an element in the alloy preferentially corrodes because one of the elements in the alloy is more active; this isn't always the case. Preferential attack also depends on the redox reactions

taking place, which metal ions are available and if those and the corrosion products are stable in the environment. De-alloying may occur in a uniform sense or in layers, it may also occur under deposits and other non-visible locations. [16, 21]

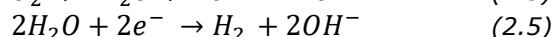
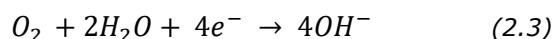
In buried artefacts the most common form of corrosion comes as a general attack on the surface which includes uniform corrosion as well as differing types of localised corrosion. Localised corrosion concentrates in small areas such as grain boundaries and indentations as well as making pits. 'Botryoidal growths' are also present on buried metals where the corrosion has been deposited in a globular form. Cracks may appear in the patina layer due to the changes in volume that result from corrosion, this favours soil elements being transferred to the buried artefact therefore promoting intergranular corrosion [14].

## 2.5 Copper corrosion

Copper and copper ions are produced at the anode entering solution by dissolution, hydration, complex formation or redeposition [22, 23] with the following electron transfer reactions taking place simultaneously:



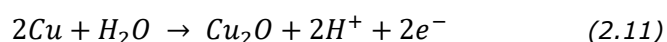
Oxygen reduction and hydrogen evolution are the main cathodic reactions of metal corrosion as shown below:



Hydrogen evolution (2.5) occurs at negative potentials, as shown in figure 2.3, favouring alkali and alkaline earth metals in more reducing acidic conditions. Therefore oxygen reduction (2.3) tends to be the only cathodic reaction involved in copper corrosion. [16, 21]

### 2.5.1 Copper oxide formation

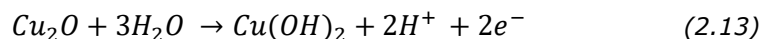
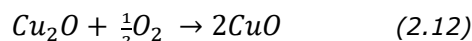
The first stage of corrosion of copper and its alloys is the formation of a passive oxide layer (which may take place before burial). Upon burial, the preferential corrosion of copper will take place usually due to the corrosive soil conditions with the redeposition of copper onto the surface. As this happens a natural corrosion cell will be set up allowing cathodic and anodic reactions to take place. The initial oxide layer formed on the copper-soil interface is usually cuprite ( $Cu_2O$ ) operating via the mechanism:



[24]

This cuprite layer is protective towards the copper alloy it has formed on and is thermodynamically stable at neutral and alkaline pH values in oxidising potentials [25]. The majority of the oxidised copper remains under the surface as an initial cuprite layer,

however in some cases the cuprite can be oxidised to cupric compounds such as CuO and Cu(OH)<sub>2</sub> appearing as an outer film to the inner Cu<sub>2</sub>O layer.



Usually, copper oxides form as a result of slow corrosion with a red, black or brown patina with either a dull or lustrous surface. [23, 24]

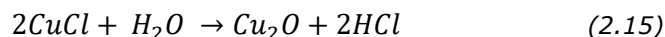
### **2.5.2 Secondary corrosion product formation**

The second stage of the corrosion process on copper and its alloys is the formation of a coarse corrosion layer due to a more severe attack. A local cell is established where oxygen, carbon dioxide and corrosive ions in the soil further corrode the artefact [12]. With this further corrosion chlorine, nitric acid or other oxidising agents present will be reduced to provide the supporting cathodic reduction [21]. During the corrosion process, changes in volume will occur resulting in cracks along the patina which enhances diffusion of soil elements into the internal areas of the metal.

If copper and its alloys are present in a saline soil environment chloride ions may migrate through the oxidised layer to form corrosion products that are attached to the original metal surface alongside any other corrosion products present [12]. Initially Nantokite (CuCl) will form via the reaction of copper cations with chlorine anions:

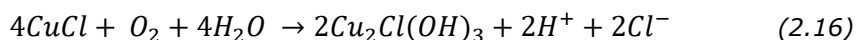


The presence of chloride leads to the instability of the artefacts as the ions break down the oxide layer causing pitting or become lodged in cracks causing further damage. The CuCl formed can continue to damage the metal further by self-catalysis in an anoxic water environment as follows:



The HCl produced in the reaction will accelerate metal dissolution and consequently form more CuCl.

Under soil burial conditions the more likely reactions to transpire are those of CuCl in an aerobic and moist environment. Copper in contact with water in this environment will lead to the production of basic copper chlorides like atacamite and paratacamite by the following mechanism:

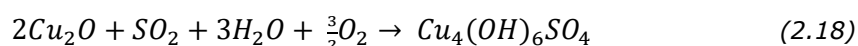


The  $H^+$  and  $Cl^-$  ions produced may combine to form HCl that will accelerate dissolution as before. The process represented in equation 2.16, moisture dependent, will continue until all metallic copper converts to copper trihydroxychlorides [26]. Copper chlorides take the form of a green or greenish blue crust. The corrosion products have an uneven encrustation that typically have a crumbly, powdery or warty surface [27].

Sulfur dioxide may be present in burial conditions as it is adsorbed onto the metal's surfaces from the atmosphere and is highly water soluble. Any sulfur dioxide present will oxidise to form sulfate ions in the presence of surface moisture as shown below:

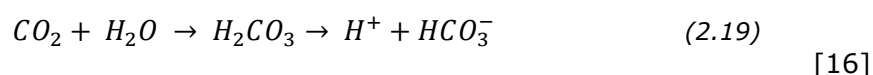


The sulfide ions then react with the cuprite layer on the artefact to form copper sulfate. Brochantite, a basic copper sulfate forms via the general reaction scheme:

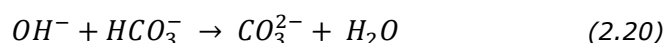


Altering the moisture and oxygen content will lead to the formation of other copper sulfates providing they are stable in the burial environment [28]. Copper sulfates tend to exhibit a relatively even green or blue patina after a slow corrosion process if the Cu is present in its +2 oxidation state. The slow corrosion of copper sulfates may also lead to a red, black or brown patina. Equally, non-protective patinas and uneven crusts may form [27].

Carbonic acid ( $H_2CO_3$ ) found in the soil will react with copper to form copper carbonates. The presence of carbonic acid is due to the reaction of carbon dioxide and the water that it's dissolved in. The acid produced will then dissociate into bicarbonate ions ( $HCO_3^-$ ) in the following process:



As corrosion proceeds, the bicarbonate ions made here will remove the hydroxyl ions produced by the first cathodic reaction involved in the initial oxidation:



The reaction of the carbonate ions produced via the above mechanism with the copper cations will result in the formation of basic copper carbonates [15]. The copper carbonates will form a green or greenish/blue crust or patina. Patina formation would be due to a slow corrosion process consisting of copper in the +1 or +2 oxidation state. The encrustation of copper carbonates would be uneven with a crumbly, powdery surface rather than an even patina [27].

Copper silicates such as chrysocolla and diopside ( $\text{CuSiO}_3 \cdot \text{H}_2\text{O}$ ), that are blue-green, green or emerald green in appearance, are formed from the resultant reaction of copper and silicon dioxide in the presence of water. The silicon dioxide may also weakly bind to the corrosion layer as a concretion rather than reacting to form copper silicates. Calcite ( $\text{CaCO}_3$ ) is another compound that forms a concretion, where a concretion is a mass of mineral matter embedded in an object that differs in composition. The outer oxide layer of corrosion on an artefact is porous enabling elements found in the soil such as Cl, P, Al, S, Si, Fe, Ca and O as well as other ions to migrate and interact with corrosion products. Cracks present along the patina due to volume changes accompanying corrosion also enhance the diffusion of soil elements into the artefact. The outer layer of corrosion will therefore be composed of precipitations of relatively insoluble corrosion products incorporating these elements and sediments (soil markers). [29-31]

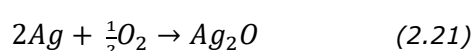
## **2.6 Silver corrosion**

### ***2.6.1 Visual characterisation of silver corrosion***

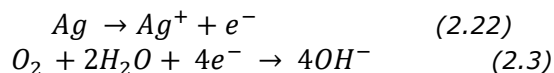
The corrosion products of silver tend to be white, purplish black or grey in colour (although purple is rarely seen). If a thin black or dark purple patina is formed, a protective silver sulfide layer is present. Patination of silver occurs either in the atmosphere or from exposure to soil where there is an absence of chlorine and bromine. A black, grey or brown crust is commonly formed as a result of chlorine, bromine or sulfur present in soil (a saline environment). If there is a high concentration of chlorine ions, the initial protective layer on silver will be permeated and disfiguration will occur in the form of a hard swollen crust. As a result of this, a greyish non-protective layer of AgCl (horn silver) will develop on the silver artefact; with silver chloride corrosion much less harmful than any copper chloride alteration products. In the presence of bromine in the soil a brown crust of AgBr may form, again in severe cases causing disfiguration. Copper corrosion products may cover the surface of a silver-copper alloy with an advanced form fabricating corroded copper, and a less advanced form producing spots of copper corrosion on the surface. [27, 29] The exact colours related to the patina or crusts formed on silver objects can vary dependent on the soil compounds that will be integrated into the outer surface of the metal [23].

### ***2.6.2 Corrosion products and mechanisms***

As a noble metal, silver won't usually react with atmospheric oxygen and tends to be corrosion resistant. Under burial conditions silver will adsorb oxygen molecules that are partially converted into oxygen ions ( $\text{O}^{2-}$ ) to form a protective silver oxide layer. Usually  $\text{Ag}_2\text{O}$  is the major oxide formed although AgO has been found after atmospheric exposure. The combination of metal cations and oxygen ions leads to the formation of  $\text{Ag}_2\text{O}$  with an overall reaction of:

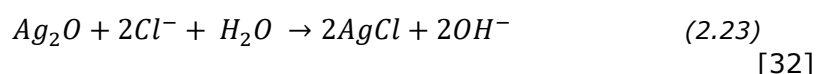


From the half-cell reactions of the anode and cathode respectively:



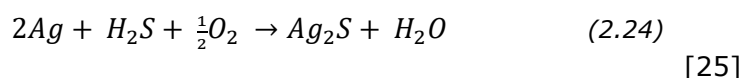
[31, 32]

The protective oxide layer is required to support the formation of AgCl and more often than not the oxide layer will be completely transformed into AgCl, so that the presence of Ag<sub>2</sub>O is undetectable. Usually sulfur containing products such as H<sub>2</sub>S, ammonia or sulfate reducing bacteria dissolve the oxide layer allowing the silver ions present to react with the Cl<sup>-</sup> ions in the soil to produce AgCl (the major corrosion product on archaeological silver) [31]. The transformation of Ag<sub>2</sub>O to AgCl is thermodynamically possible and shown below:



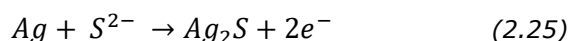
[32]

The sulfur present in the soil environment as mentioned can also lead to the formation of silver sulfide (Ag<sub>2</sub>S). Usually silver sulfide appears on silver as a film of black tarnish from an atmospheric environment where sulfur pollutants such as hydrogen sulfide (H<sub>2</sub>S) and carbonyl sulfide (OCS) are present [31]. The overall reaction mechanism for the formation of silver sulfide is:



[25]

With the ionic equation of:



Over time, silver sulfide in the natural atmosphere will slowly become silver sulfate:



[33]

Again, as with copper artefacts, the oxide layer of corrosion on silver is porous and enables elements found in the soil to migrate and interact with corrosion products. Any cracks present as before will enhance the diffusion of soil elements into the metal. Concretions of compounds may also be found on exterior layers. The outer corrosion products, such as AgCl, will have resulted from the reaction of the metal constituents and soil elements, as with any metal. The inner corrosion layer will incorporate oxygen containing phases. As the oxide layer is not usually detected in silver artefacts due to its transformation into AgCl, any phases containing oxygen will be in connection with other elements such as Ca, Si, Cu and so on. [12, 31]

## 2.7 Corrosion in alloys

In the majority of cases metal used to produce coins is alloyed which alters the way it behaves when corroding. Copper tends to be alloyed with zinc, tin or lead which will protect the copper that is more noble in the alloy. It may also be alloyed with silver, but then becomes the more active element and so corrosion will accelerate. A galvanic corrosion process may take place where the more active metal preferentially corrodes over the more noble, with the activity of metals deduced via the galvanic series (figure 2.2). Ultimately, regardless of the individual metals activity the preferential attack of one metal will depend on the reactions taking place and which metal ions are present and stable in the environment to selectively leach out; this is known as selective corrosion [25]. In some cases such as that of a copper-tin alloy the more active element, tin, is preserved over copper. Copper will leach out and may redeposit to form corrosion products but the surface will become enriched with tin as the tin acts as the cathode [27].

In a silver-copper alloy, the generation of a galvanic cell occurs as the preferential corrosion of the more active copper takes place. The noble silver in the alloy acts as a cathode producing a silver-surface enriched layer; a copper enriched layer is also formed with the redeposition of corroded copper onto the surface. Cuprite ( $\text{Cu}_2\text{O}$ ) is formed on the copper enriched surface which can then later be converted into other corrosion products depending on the environment. Despite silver being cathodic in the galvanic cell with copper, it may suffer corrosion due to local action cells where the silver reacts with oxygen, hydrogen, sulfur or chlorine to produce  $\text{AgCl}$ ,  $\text{Ag}_2\text{S}$  and  $\text{Ag}_2\text{O}$ . This explains the presence of both copper and silver corrosion products in a silver-copper alloy with a relatively high copper content. In other metals, not just silver, the noble metal (cathode) may corrode via a local action cell rather than acting as it should in galvanic coupling [25, 29]. Overall in the corrosion of metal alloys, it is the thermodynamically most stable products that will form dependent on which metal ions and corrosion products are stable at certain pH and potentials as shown in Pourbaix diagrams.



## Chapter 3 - Samples and Sites

### 3.1 Choice of materials for the study

The coins in this study were found using an XP DEUS metal detector in the top 3-10 inches of the topsoil. All samples were found in the UK in the East Midlands (Nottinghamshire, Derbyshire or Lincolnshire) or South Yorkshire (Rotherham). Upon excavation the coins were brushed of any loose soil particles and stored in sealed bags. The top 5-6 inches of soil surrounding four coin samples was acquired for analysis. All samples were kindly donated by Andy Morris.

#### 3.1.1 Coin samples

All 18 coins analysed in this project are shown below with their assigned reference and recorded location:



R06 - Roman  
Thoresby  
SK63903 71712



R02 - Roman  
Langford  
SK820 575



R294 - Roman  
Laughterton  
SK83503 77032



R253B - Roman  
Langford  
SK8229 5931



R03 - Roman  
Langford  
SK820 575



M516 - Medieval  
Thorpe Salvin  
SK516 814



M805 - Medieval  
Holme  
SK805 586



M804 - Medieval  
Rampton  
SK804 787



M821 - Medieval  
Langford  
SK8212 5913



M333 - Medieval  
Holymoorside  
SK333 700



V186 - Modern  
Collingham  
SK83342 60606



V112 - Modern  
Collingham  
SK83342 60606



V114 - Modern  
Collingham  
SK83342 60606



V106 - Modern  
Collingham  
SK83342 60606



Coin A - Roman  
Brough  
SK83746 59240



Coin B - Roman  
Brough  
SK83774 59226



Coin C - Modern  
Brough  
SK83538 59209



Coin D - Modern  
Brough  
SK84162 59015

*Figure 3.1: OM images of all the coin samples in the study*

### 3.1.2 Soil samples

Three soil samples were acquired from Brough, Nottinghamshire, England and labelled Soil A, Soil C and Soil D with their assigned reference matching the coins found in the topsoil. A separate soil sample was not taken for coin B due to the close proximity of coin A and so soil A was used to represent the burial environment of coin B. Soil samples from other sites were unable to be obtained.



Figure 3.2: Map indicating the location of the soil samples [34]

The sedimentary bedrock of soils A, C and D belong to the Penarth group containing silica minerals from the mud, silt, sand and gravel that originally formed the sedimentary rocks. The lithology of the bedrock is of grey to black mudstones with underlying limestone and sandstone. The record of superficial deposits (the youngest geological deposits) were only found for soil C and D belonging to the Balderton sand and gravel type. The rocks present were formed via the deposition of sand and gravel from the River Trent that predominated the environment. Any sandy gravel has an orange-brown colour that is mainly rounded quartz pebbles with some flint and Triassic sandstone. As well as rocks, Alluvium was formed on floodplains from silt and clay with bogs depositing peat. [35]

The fields are mainly agricultural, currently under cultivation; as a result any artefacts close to the top of the soil column are exposed to varied conditions and aspects of human and animal activity [36]. The climate of the area also heavily influences the soil and thus effects any artefacts buried within. The land here, like the rest of the UK, has experienced a range of temperature and rainfall with the monthly climate recorded between 1961 to 2010 by the MET office demonstrating the recent diversity in Nottingham.

Climate period	Maximum temperature /°C	Minimum temperature /°C	Maximum Rainfall /mm	Minimum Rainfall /mm	Maximum Sunshine /hours	Minimum Sunshine /hours
1961-1990	20.2	0.3	77.9	54.4	180.7	43.4
1971-2000	20.9	0.7	82.7	51.8	190.0	42.6
1981-2010	21.1	0.8	82.0	54.0	189.6	45.0

*Table 3.1: Highest and lowest units recorded in each month for the specified climate period from the Met office [37]*

Higher temperatures tend to speed up chemical reactions in the soil and an environment devoid of water will precipitate dissolved chemicals at the soils surface. Low temperatures affect organic life and decay and will not have a major influence upon corrosion. In warmer weather, where the temperature is close to maximum any buried artefacts may have experienced enhanced corrosion. Soil moisture is also an influential factor towards the corrosivity of an environment, as the corrosion of metals in soil is determined by the diffusion of oxygen in water. Therefore as the moisture content rises (the more rainfall and less sunshine there is) the corrosion rate may accelerate [36].

About 99% of the soil in the world has developed from the weathering of bedrock with the remaining 1% found in organic materials from plant growth [38]. Soil comprises a mixture of parent material, chemically altered materials and organic matter (humus). The bedrock composition of these fields will be the major influence for the soils composition, therefore an introduction of silicate minerals into the patina layer would be expected alongside other ions found in the soil. Moisture may influence corrosion from rainfall and even possibly from the river Trent nearby, however as the superficial deposits are sandy and gravelly the soil may drain relatively well with water damage at a minimum. The field has been exposed to varying weather patterns affecting the moisture and temperature of the soil; this and other factors will have affected the severity of corrosion on the buried metal.

## **3.2 Background of the areas in the study**

### **3.2.1 Roman finds**

The Sites and Monuments Record (SMR); now the Historic Environment Records (HER), hold local and national records on the historic environment of England. The Nottinghamshire SMR holds 648 records relating to the Roman period, which include 5 small towns, 12 villas and over 250 settlements. It is evident when considering all sources of information of finds, earthworks, aerial photography and excavations that the whole of Nottinghamshire was well inhabited throughout the Roman Period. The Fosse Way, a Roman Road that linked Exeter to Lincoln had four small towns lying along it which included Vernemetum (Willoughby-on-the-Wolds), Margidunum (Bingham), Ad Pontem (Thorpe) and Crococalana (Brough). Roadside settlements were also apparent nearby with a substantial settlement at Newark [39]. In the Roman period the Roman military moved north to Lincolnshire to secure the Trent Valley and Humber estuary. The positioning of settlements in Lincolnshire varies with



some on main roads, some acting as markets to the surrounding countryside and even riverside settlements [40]. There are documented Roman movements and settlements in Lincolnshire and Nottinghamshire supporting the finds of Roman coins in these counties.

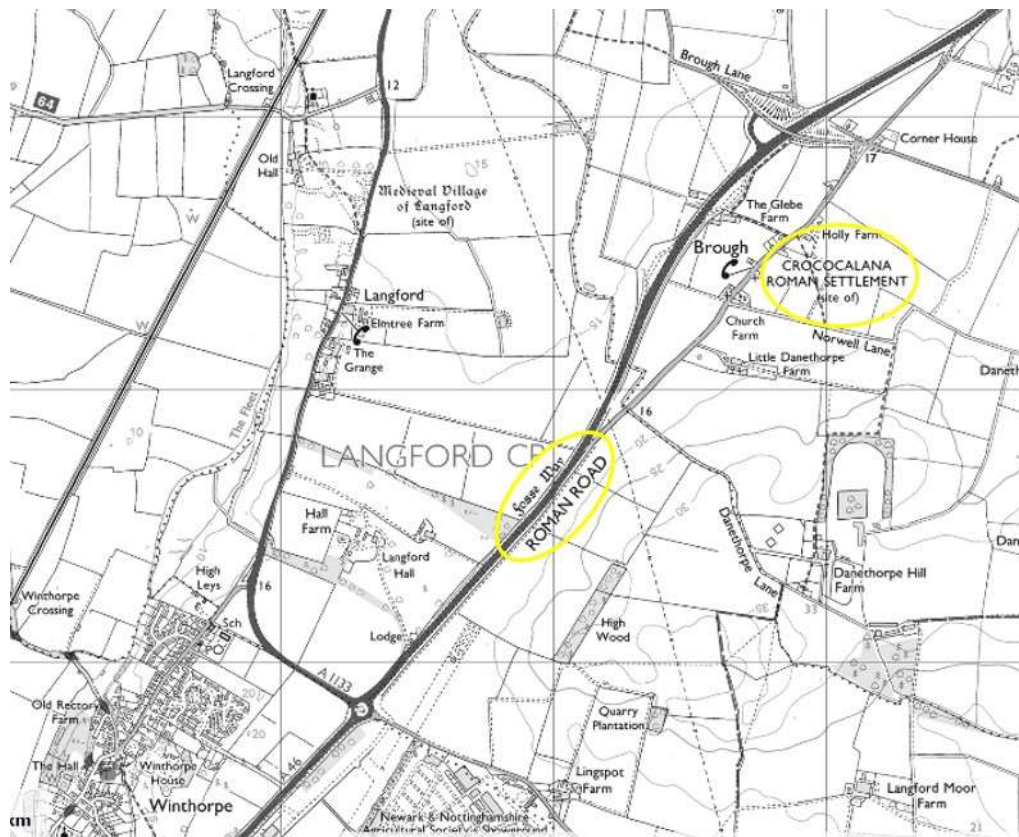


Figure 3.3: Magic Map indicating the location of the Roman Settlement Crocalana and the Fosse Way [41]



Figure 3.4: Google Earth Map showing the location of the Roman Settlement Crocalana and the Fosse Way [42]

### 3.2.2 Medieval finds

The Nottinghamshire SMR holds 893 records belonging to the Middle Ages consisting of castles, monastic sites, Medieval villages and churches amongst others. The 10<sup>th</sup> to 13<sup>th</sup> centuries represented an exponential population growth where communities were established and certainly by the 13<sup>th</sup> century Nottinghamshire's settlement pattern was fixed. Typically settlements consisted of villages and hamlets near open fields of pasture and possible woodlands. The villages were distributed in areas close to water sources with Medieval villages found in the Trent Valley itself and along the banks of the River Trent. The settlement patterns of the 16<sup>th</sup>, 17<sup>th</sup> and 18<sup>th</sup> centuries (post-medieval) were the same as the Medieval ones where settlement was established in areas close to the river and were largely village based. For these periods archaeological evidence of entire landscapes have survived where Medieval villages were converted into pasture for sheep grazing due to socio-economic difficulties of the late Middle Ages [43, 44]. It is not surprising to find Medieval coinage in the region due to inhabitation.

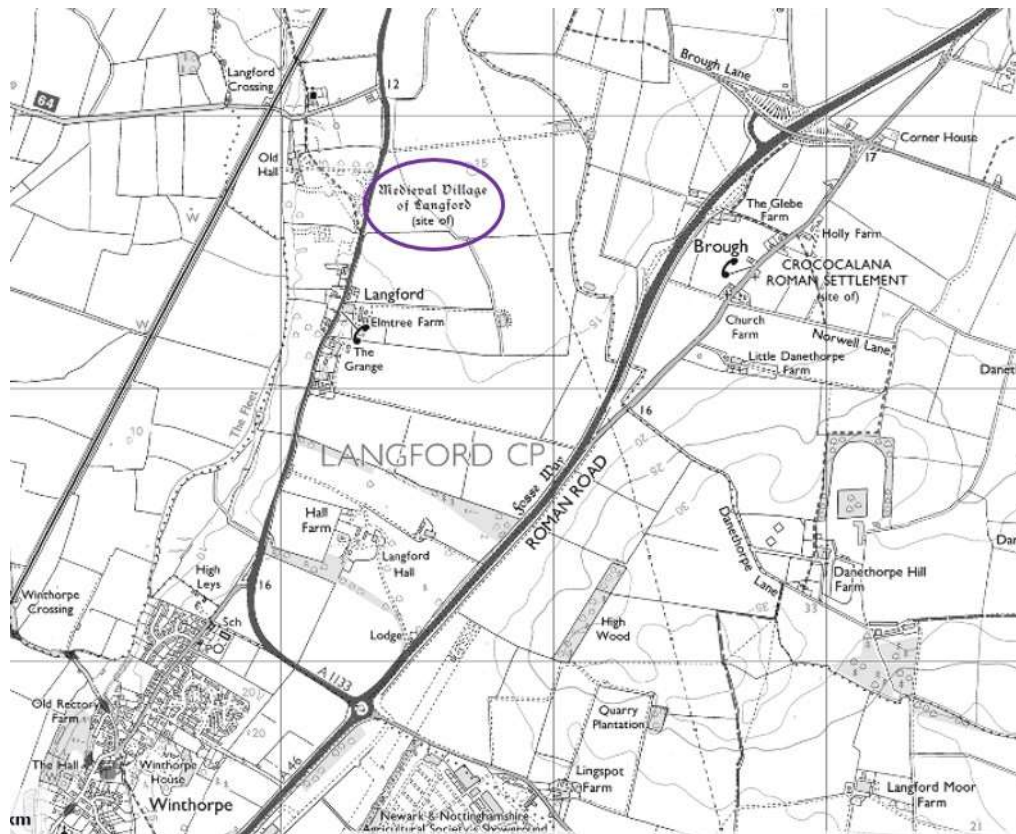


Figure 3.5: Magic Map indicating the location of the Medieval village of Langford [41]



Figure 3.6: Google Earth Map showing the location of the Medieval village of Langford [42]

### 3.2.3 Modern finds

The industrial period in Nottinghamshire, from 1750 onwards, shaped the landscape leading to the current environmental setting of the county. Maps from this era show the layout of the land within the county with a map of Nottingham from 1960 showing features such as roads, schools and parks alongside adverts for shops evidencing the exchange of modern currencies [45]. The staples of the industrial revolution in this county were found in coal, hosiery and lace. The county developed a self-sustaining supply and demand chain, localised to the west, as well as exporting supplies to other countries such as France, Germany and Spain. Revolutions in industry, agriculture, communications and society arose in this industrial period [46]; it is evident that exchange and use of 'modern' currency extended over this area.

The geographical locations of the finds are shown in the maps below:



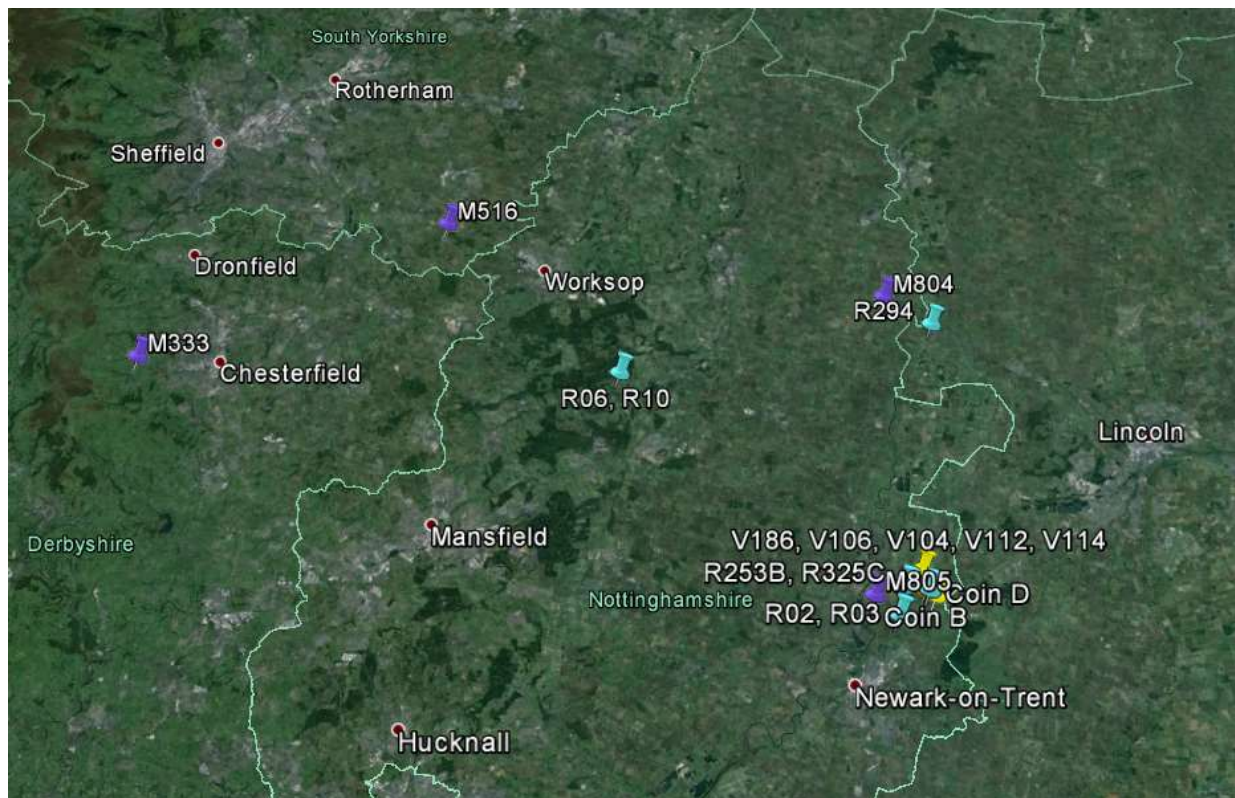





Figure 3.7: Google Earth Map indicating the location of all coin samples [47]

Key:

Modern	
Medieval	
Roman	

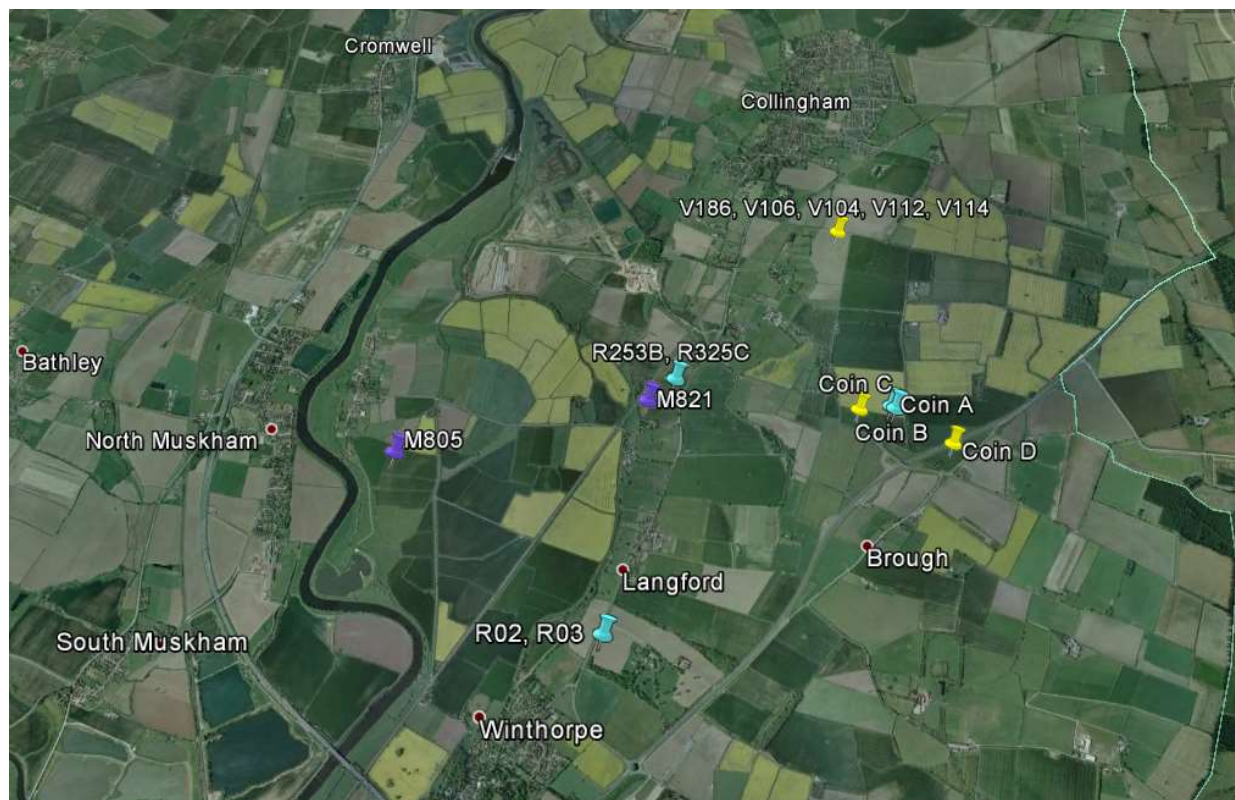


Figure 3.8: Google Earth Map indicating the location of the coin samples densely populated in Nottinghamshire [42]



## Chapter 4 - Methodology

An overview of each of the techniques used in the study is given below. More details can be found in Appendix A.

### 4.1 X-ray Diffraction

X-ray diffraction (XRD) analysis was performed using a Bruker D2 Phaser desktop diffractometer with experiments executed in reflection mode. A Lynxeye detector was used for the collection of diffraction data. Experimental parameters for data acquisition included the use of Cu K $\alpha$  radiation ( $\lambda = 1.54184 \text{ \AA}$ ), an applied voltage of 30kV and a current of 10mA for the X-ray source. The powder diffractometer scanned  $2\theta$  from  $5^\circ$  to  $100^\circ$ . Coin samples required no sample preparation; soil samples were ground to a fine powder using a pestle and mortar. All XRD pattern analysis performed throughout chapters 5, 6 and appendix F were indexed and referenced to the data from the Handbook of Mineralogy [48].

Mineral	d-spacing/ $\text{\AA}$	Relative Intensity/a.u.
Copper (Cu)	2.088	100
	1.808	46
	1.278	20
	1.0900	17
	0.8293	9
	0.8083	8
	1.0436	5
Cuprite ( $\text{Cu}_2\text{O}$ )	2.465	100
	2.135	37
	1.510	27
	1.287	17
	3.020	9
	1.233	4
	0.9795	4
Malachite ( $\text{Cu}_2(\text{CO}_3)(\text{OH})_2$ )	2.857	100
	3.693	85
	5.055	75
	5.993	55
	2.520	55
	2.778	45
	2.464	35
Silver (Ag)	2.359	100
	2.044	40
	1.231	26
	1.445	25
	0.9375	15
	1.8341	13
	0.9137	12
Chlorargyrite ( $\text{AgCl}$ )	2.77	100
	1.961	60
	1.240	40
	3.22	30
	1.134	30

	0.926	30
	1.672	20
Quartz (SiO <sub>2</sub> )	3.342	100
	4.257	22
	1.8179	14
	1.5418	9
	2.457	8
	2.282	8
	1.3718	8
Kaolinite (Al <sub>2</sub> Si <sub>2</sub> O <sub>5</sub> (OH) <sub>4</sub> )	7.16	Not stated
	3.573	
	4.336	
	2.491	
	2.289	
	2.558	
	2.379	
Cassiterite (SnO <sub>2</sub> )	3.347	100
	2.6427	75
	1.7641	57
	2.3690	21
	1.6750	14
	1.4155	14
	1.4392	12
Goethite (α-FeOOH)	4.183	100
	2.450	50
	2.693	35
	1.7192	20
	2.190	18
	2.253	14
	4.98	12

Table 4.1: Diagnostic reflections and intensities for the crystalline corrosion product constituents of the patinas in this study [48]

## 4.2 X-ray Fluorescence

A Bruker Handheld XRF spectrometer (Tracer IV-SD series) with a Rh target X-ray tube was used for fluorescence data collection. The elemental composition was recorded using a windows based PDA system attached to the spectrometer with elements matched against internal alloy standards. Computational analysis was undertaken using the S1 PXRF software which enabled full control of acquisition parameters. All samples had an analysis time of 30 seconds and required no sample preparation.

Element	Ka peak/keV	La peak/keV	Possible interferences
Al	1.49		
Si	1.74		
P	2.01		
S	2.31		
Cl	2.62		ClKa (2.62) with AgLa (2.98)
K	3.31		
Ca	3.69		CaKa (3.69) with SnLa (3.44)
Ti	4.51		TiKa (4.51) with VKa (4.95)
Mn	5.90		
Fe	6.40		
Ni	7.48		

Cu	8.05		
Zn	8.64		
As	10.54		AsKa (10.54) with PbLa (10.55)
Se	11.22		
Br	11.92		
Rh	20.22	2.70	
Pd	21.18	2.84	PdLa (2.84) with AgLa (2.98)
Ag	22.16	2.98	AgLa (2.98) with ClKa (2.62) and PdLa (2.84)
Cd		3.13	
Sn	25.27	3.44	SnLa (3.44) with CaKa (3.69)
Sb	26.36		
Au		9.71	
Pb		10.55	PbLa (10.55) with AsKa (10.54)
Bi		10.84	

*Table 4.2: Characteristic X-rays of elements graphically represented throughout this study [49]*

XRF cannot identify elements lighter than Na as the fluorescence photons from these elements have an energy that is too low to transmit through air and so are not detected efficiently by a conventional detector. The table below shows characteristic X-rays of elements lighter than Na that will not be included in the XRF data.

Element	Ka peak/keV
Li	0.054
Be	0.11
B	0.18
C	0.28
N	0.39
O	0.52
F	0.68
Ne	0.85

*Table 4.3: Characteristic X-rays of elements lighter than Na [49]*

In the majority of analyses undertaken in this study, Rh and Pd are present due to the cap and X-ray target tube on the handheld XRF containing these elements. The X-rays from the X-ray tube strike the atoms in the samples without fluorescence being promoted and so appear as a Rayleigh peak at the same energy a source element would be identified.

Sum peaks are peaks created by two photons arriving simultaneously at the detector experienced as a single X-ray at twice the photon energy. Copper's sum peaks appear at 16.08keV and do not cause any interference with other X-ray lines; with the analysis of lead however, the sum peaks pose a problem as they overlap the Ka lines for cadmium and tin which can be misleading when interpreting which elements are present in the spectra [50].

### 4.3 SEM-EDS

Scanning electron microscopy (SEM) images were taken using a JEOL 6060LV SEM. The secondary electron detector (SEI) allowed visualisation of the samples under high vacuum operation. An Oxford Instruments INCA X-sight 7582 EDS system was employed as the

energy dispersive X-ray detector (EDS). SEM micrographs and EDS spectra of the samples were collected using an accelerating voltage of 20kV, a magnification of x200 with a working distance that ranged between 8mm to 10mm. The obverse and reverse of each coin was analysed with no sample preparation placed in their entirety onto the sample holder.

SEM samples are required to be conductive to stop electrons collecting on the sample and interfering which if transpires results in blurring. If a non-conductive sample is used it is sputter coated with metal, usually gold or aluminium. Carbon conducting tape is used throughout this study to prevent charging, meaning that the presence of carbon is inevitable on every spectra collected. Oxygen will also be present on every spectra collected due to outside influence such as contamination from carbon dioxide (CO<sub>2</sub>) or oxygen (O<sub>2</sub>) in the air. Unless specifically commented on with reference to a corrosion product the existence of C and O in the elemental analysis can be disregarded.

#### **4.4 Optical Microscopy**

A Keyence VHX-2000 digital microscope was used to investigate the surface morphology of the corrosion products present on the coins. A VH-Z20R lens was used which allowed magnification from a minimum of 20x to 200x. Optical photographs were obtained at various magnifications with no sample preparation required.

#### **4.5 MEIS**

The copper samples used in the MEIS measurements were chemically etched in two stages as described below. All solvents and reagents were purchased from commercial sources and used without further purification unless stated otherwise.

##### ***4.5.1 Chemical etching procedure***

25mL of glacial acetic acid was pipetted into a 250mL volumetric flask, deionised water was added so that the bottom of the meniscus was level with the 250mL mark, the flask then sealed and inverted ~40-50 times. 100mL of the 10% acetic acid solution was added to a 150mL beaker and the sample coin lowered into solution by two thirds of the diameter and left for 6 hours. After which it was raised by one third, the bottom third remaining in the solution for a further 18 hours. The coin was taken out of solution and allowed to dry over silica that had been heated to 100°C for 1 hour and left to cool.

##### ***4.5.2 Experimental analysis and parameters***

MEIS measurements were performed at the IIAA at the University of Huddersfield using 100keV He<sup>+</sup> ions. The sample was introduced from air at the loading chamber and transferred to the storage chamber and then to the analysis chamber with the sample remaining under UHV throughout. The sample was aligned with respect to the incoming beam using the sample goniometer; a scattering angle of 125° was employed to give the highest possible dispersion between the masses detected. The analysing energy was varied

between a minimum of 35.7keV and a maximum of 90keV. A toroidal electrostatic analyser fitted with a multiplier and detector detected the back scattered ions. The two-dimensional ion detector provided multiple tiles of ion counts as a function of energy and scattering angle. These were stitched together using MEIS control software to a single 2-D spectrum from which ion energy spectra were cut.

The He beam used probes the surface structure of the sample, with the mass of the nucleus that the initial beam particles collide with directly correlating to the energy of the scattered ion. An elastic collision occurs where a transfer of energy takes place from the moving particle to the target atom with the consequent energy loss of the ion dependent on the mass ratio of the incident ion/target atom and the scattering angle. By application of the principles of conservation of energy and momentum, the kinematic factor can be calculated and consequently the energy of the target atom. The derived equation for calculating the kinematic factor is as follows:

$$k = \frac{E_1}{E_0} = \frac{1}{(1+A)^2} (\cos \theta \pm \sqrt{A^2 - \sin^2 \theta})^2 \quad (4.1)$$

$k$  = kinematic factor

$E_1$  = energy of the projectile atom after collision

$E_0$  = energy of the incident projectile atom

$A = \frac{m_2}{m_1}$  where  $m_1$  is the mass of the incident projectile atom and  $m_2$  is the mass of the target atom

$\theta$  = scattering angle

The full derivation process for the kinematic factor is found and referenced in appendix B.

The energy of the projectile atom after collision ( $E_1$ ) reflects the mass of the target atom. Equation (4.1) is rearranged for  $E_1$  in order to identify the elemental mass signals found in the energy spectrum. Substituting numbers into the equation and rearranging gives the energies for scattering through  $125^\circ$  of the different atomic masses as shown in the table below:

Element	Energy/keV
Ni	80.03
Cu	81.35
Zn	81.81
Ge	83.41
As	83.85
Se	84.58
Pb	93.37
Bi	93.42
Pd	88.14
Ag	88.28
Cd	88.70

Table 4.4: Energies of the elements studied for identification from signals in the MEIS spectra

## 4.6 Soil analysis

### 4.6.1 Visual analysis procedure

#### 4.6.1.1 Soil colour

The colour of the soil samples were identified using the Munsell soil color charts [51]. The undried soil sample was held directly behind the aperture that separated the closest matching colour chips.

#### 4.6.1.2 Soil texture

A visual soil assessment technique was implemented for the investigation of soil texture. The soil was moistened by adding 4-5 drops of deionised water from a pipette and rubbed between fingers. The textural category was identified using the following procedure from soil texture leaflet 895.

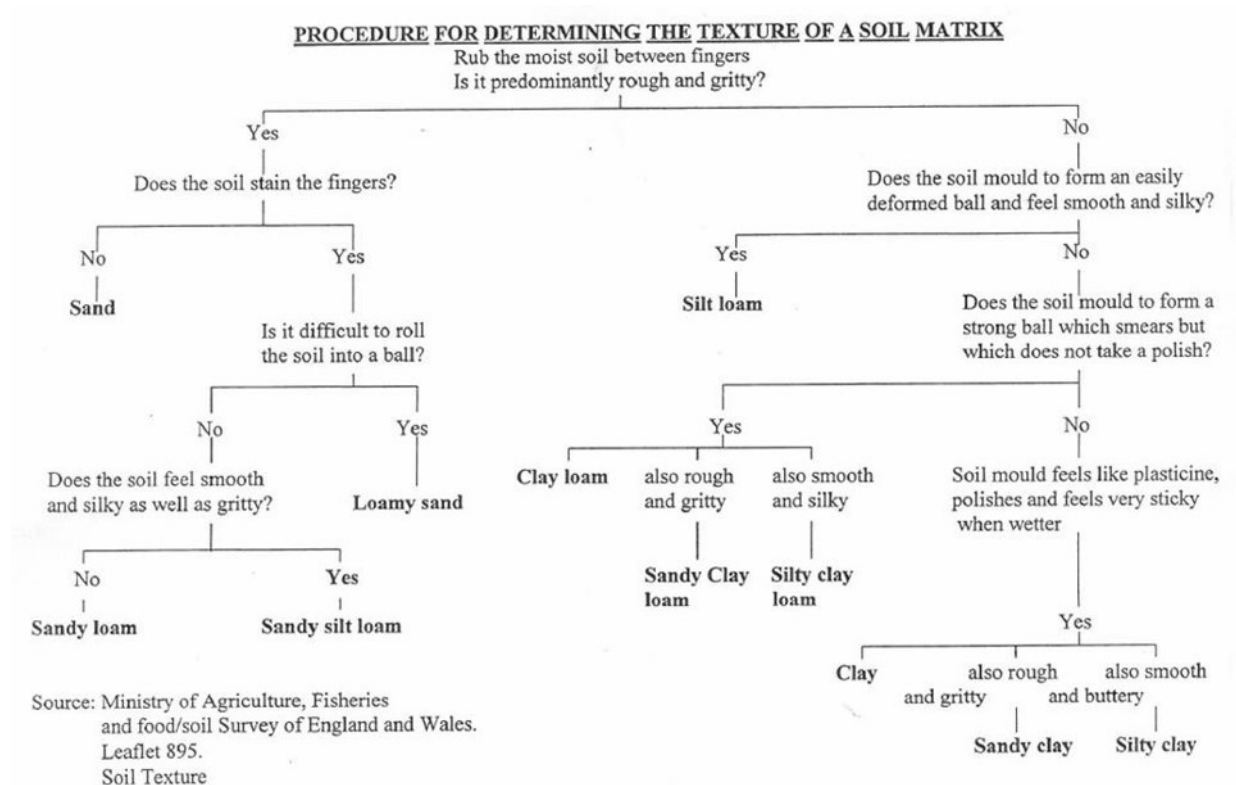


Fig. 1

Figure 4.1: Procedure for determining the texture of a soil matrix [52]

#### ***4.6.2 pH analysis procedure***

The pH of soil is measured by mixing it with de-ionised water to a known ratio and taking a measurement of the pH. However, this only measures the active acidity of the soil; the hydrogen ions dissolved in the soil solution. To determine a more accurate estimate of the soil pH the reserve acidity must be measured; the acidity made up of the cations present on the surface of the soil and in the organic matter. To measure the reserve acidity a cation exchange must take place and by using a calcium chloride ( $\text{CaCl}_2$ ) solution  $\text{Ca}^{2+}$  cations displace ions such as  $\text{H}^+$  from the surface of the soil releasing them into the solution. The solution will then have a  $\text{H}^+$  concentration that is more representative of the soil solution in the field as it is less affected by soil electrolyte concentration [53]. Both pH methods will be used in this report.

##### ***4.6.2.1 pH analysis using deionised water***

###### ***Experimental procedure***

A 20mL universal container was filled to the 5mL mark using an undried soil sample. De-ionised water was added in equal amounts the tube was stoppered and vigorously shaken for 10 to 20 seconds. The tube was allowed to stand for 10 minutes before being shaken to re-suspend the soil. The pH probe was then lowered into the suspension so that the glass electrode and junction were just below the surface of the liquid and the pH reading recorded.

##### ***4.6.2.2 pH analysis using calcium chloride solution***

All solvents and reagents were purchased from commercial sources and used without further purification unless stated otherwise.

###### ***Preparation of 0.04M calcium chloride solution***

Calcium chloride (4.4404g) was transferred to a 1L volumetric flask, deionised water was added to the flask so the bottom of the meniscus was level with the 1L mark. The volumetric flask was sealed and inverted ~40 -50 times.

###### ***Experimental procedure***

5mL of 0.04M calcium chloride solution was added to the tube containing the soil and deionised water as prepared for part one of the pH analysis. The tube was stoppered and vigorously shaken for 10 to 20 seconds. The tube was allowed to stand for 10 minutes. The pH probe was lowered into the liquid layer created without disturbing the settled sediment and the pH reading recorded. This whole process repeated for all soils in the study.

## Chapter 5 - Copper Coinage Results

The results presented in chapter 5 are those of the following samples: burial environment D, Coin D, R06 and R02. Coin D was from the 'Modern' era, coins R06 and R02 belong to the Roman period therefore a discussion of coins from varying historical periods is achieved.

Burial environment D and coin D are initially discussed in order to understand the influence the environment had upon copper coins in burial with key information gained from this analysis applied to the other coins in the study. Another copper coin and adhering soil sample coin C and burial environment C are found in appendix F. Burial environment D had a stronger influence on Coin D and so was chosen for discussion.

The second coin chosen for discussion was R06 as the sample demonstrated a smooth layer of primary corrosion products as well as influence from the burial soil. The other copper alloy samples studied in this project presented in appendix F all showed layers of primary corrosion and/or deposits of soil compounds; they are V186, V112, V114, R294, R253B and R03.

Coin R02 was chosen as the final sample for discussion of copper corrosion as it had the growth of secondary copper corrosion products as well as primary corrosion products and compounds from the soil. The corrosion layers in this sample had a different morphology to the smooth primary corrosion layers identified in all other copper samples studied.

For each sample the results are presented starting with the basic identification of the coin and continuing with analysis that increasingly reveals more about the corrosion products on the surface. Firstly the heritage of the coin is established followed by the XRF examination of the sample in order to identify the metallic alloy. Once this information is known an estimate of the corrosion products based on the visual interpretation of colours and previous knowledge of the corrosion of the alloy can be formed. The SEM-EDS analysis then reveals elementally what is present in the different layers of the coins furthering any estimations of the corrosion products present. Finally, XRD analysis reveals exactly which corrosion products are present on the surface of the coin drawing all conclusions together.



## 5.1 Copper Coinage corrosion with adhering soil samples

### 5.1.1 Burial environment D

#### 5.1.1.1 Results for burial environment D

Soil	Colour	Texture
D	7.5YR 2.5/1	Loamy sand

Table 5.1: Visual analysis of soil D

pH test	Average	Error
Water	7.32	0.02
CaCl <sub>2</sub>	6.51	0.02

Table 5.2: pH measurements for soil D

Element	Composition/%	Error/± %
Si	69.70	1.50
Fe	16.40	0.40
Al	10.30	1.40
Ti	1.56	0.06
Pd	1.27	0.10
Zr	0.38	0.03
Cu	0.16	0.04
Cr	0.10	0.03
Zn	0.08	0.03
Mn	0.06	0.11
V	0.02	0.03

Table 5.3: XRF Elemental Composition of soil D

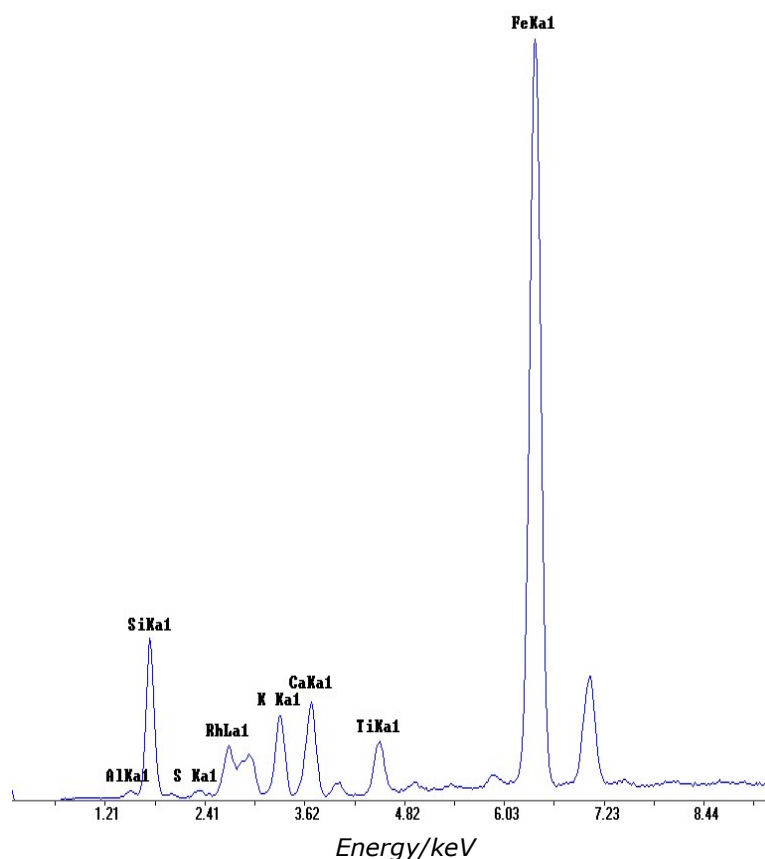


Figure 5.1: XRF pattern of soil D

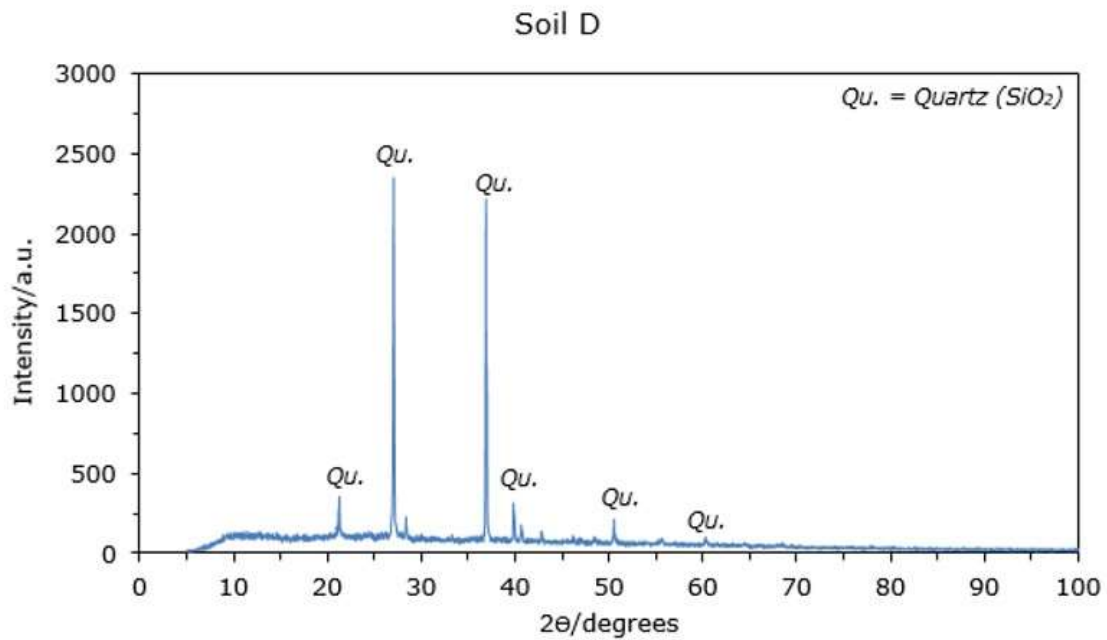


Figure 5.2: XRD pattern of soil D

#### 5.1.1.2 Discussion for burial environment D

The British Geological Survey (BGS) reported that the sedimentary bedrock of soil D formed with a heavy influence of silica minerals and therefore it is expected that soil D will be composed mainly of silicate minerals. Soil D was identified as a loamy sand using the soil texture assessment technique described in chapter 4; and seeing as the most common constituent of sand is silica ( $\text{SiO}_2$ ; predominantly found naturally in the form of quartz) the prediction that the soil will contain silicate minerals from the bedrock is supported.

The XRF analysis performed on the soil identified silicon as the main element in the composition as expected due to the weathering of the bedrock contributing to 99% of the soils composition. The total elemental composition from the XRF analysis was 100.04% and included the three major elements silicon ( $69.70 \pm 1.50\%$ ), iron ( $16.40 \pm 0.40\%$ ) and aluminium ( $10.30 \pm 1.40\%$ ). Titanium and palladium followed in decreasing percentages as minor elements and other elements such as Zr, Cu, Cr as shown at the bottom of table 5.3 were present in trace amounts. The three major elements identified are commonly found in soil and so are expected, they are also all identified in the XRF graph (Fig. 5.1) by their Ka peaks. Palladium does not show any peaks in the XRF graph and its presence in the data is probably due to Rayleigh scatter, the La lines of Rhodium in the graph are equally for this reason. The trace elements in the data could be constituents of the soil but are not found in the XRF graphs. There is an addition of potassium Ka line, calcium Ka line, sulfur Ka line and rhodium La line in the XRF pattern. These elements are commonly found in the soil and there were energy lines in the spectra unaccounted for where these elements should be

found and so were consequently labelled. The information provided by the XRF analysis is that silicon is the major constituent of the soil with iron, aluminium, titanium, potassium, calcium and sulfur also present.

The XRD analysis of the soil fully confirms the presence of silicate minerals as quartz was the major compound identified. The XRD pattern produced by soil D shows the first six d-spacings present in the literature for quartz as found in table 4.1 in chapter 4.

The Munsell soil color charts identified soil D as being black with yellow sandy flecks (7.5YR 2.5/1). This colour identification can be matched to the lithology of the bedrock with the black colour represented by the black mudstone and the yellow sandy flecks being the limestone and sandstone. The superficial deposit doesn't seem to have much influence on the colour of the soil but seeing as the bedrock makes up 99% of the soil this is expected.

The burial environment in question has experienced diverse weather with moisture content and temperature fluctuating affecting the severity of corrosion on the buried metal; however it is the pH of the burial environment that heavily influences the aggressiveness of the environment and ultimately what corrosion products form. The active acidity of the soil had an average pH of  $7.32 \pm 0.02$  as shown in table 5.2 (raw data found in appendix D), with the reserve acidity slightly lower at a pH of  $6.51 \pm 0.02$ . The reserve acidity is expected to be lower due to the higher  $H^+$  concentration in the  $CaCl_2$  solution as a cation exchange took place. The reserve acidity is more representative of the conditions in the field so it is assumed that the pH of  $6.51 \pm 0.02$  influenced any corrosion that took place in burial.

The Pourbaix diagram below is that of the reactivity of copper in water, a line has been drawn showing the pH of soil D and so it is expected that copper will produce cuprite.  $Cu^{2+}$ ,  $Cu^+$  and Cu are also all stable at this pH. It is difficult to predict what will happen to the metal in burial even with the use of Pourbaix diagrams as a combination of factors influence what will form; ultimately it is a question of what the most thermodynamically stable product will be under burial conditions.

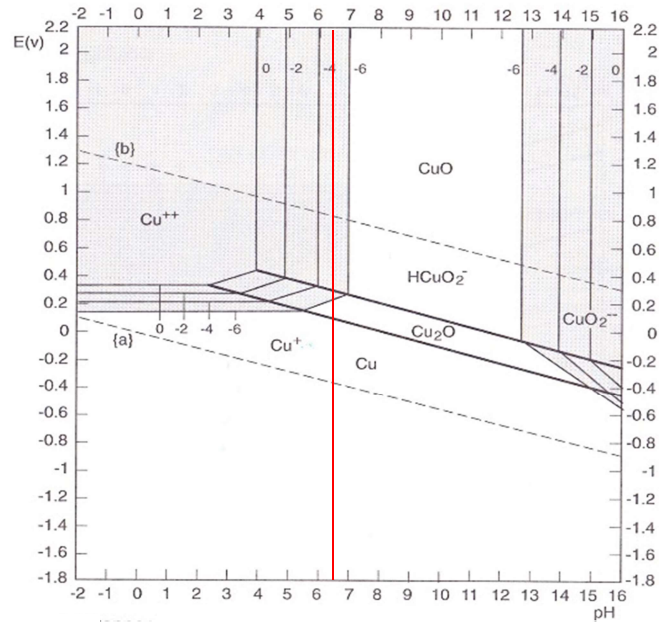


Figure 5.3: Stability diagram for copper p.63 [16]

### 5.1.2 Modern coin - Coin D

Soil D, the adhering soil surrounding Coin D, will have directly influenced the environment and therefore any corrosion products to transpire on this coin.

#### 5.1.2.1 Identification

Coin D was identified as a Victoria Bun Head Farthing minted in 1861; from the Victorian 'Modern' era. This conclusion was reached confidently as key details of the coin survived burial. The diameter and weight of a Bun Head Farthing reported in literature are 20.00mm and 2.9g respectively [54]; coin D's measurements were 2.5804g and 20.3mm which are very close to the literature values. This information can add evidence to the identification but cannot be used for direct comparison as alteration products and corrosion alter the shape and nature of coins.



*Figure 5.4: OM image of the obverse of coin D, x50 magnification*



*Figure 5.5: OM image of the reverse of coin D, x50 magnification*

The obverse of a Bun Head Farthing should show a left facing bust of Victoria, which as seen in figure 5.4 is visible in its entirety. The inscription on the obverse should read VICTORIA D:G: BRITT:REG:F:D: which is seen apart from half of the semi colon after the last D that is covered by an orangey/brown corrosion. The border on this coin is that of the toothed variety, with no other possible border present for this minting date. The reverse inscription for a Bun Head Farthing should read FARTHING which is present in its entirety above seated Britannia. Seated Britannia should be right facing holding a shield and trident, which as shown above in figure 5.5 can be seen. The outline of the ship on the right hand side is visible; the outline of the lighthouse on the left hand side can only just be made out with no detail present. The date is clearly visible in exergue below Britannia as 1861. [54]

#### **5.1.2.2 Results from XRF analysis**

As XRF is a surface sensitive technique analysing at a depth of  $\sim 2\text{mm}$  it provides no elemental data of the bulk, meaning that numismatists have difficulties drawing conclusions about any coins original composition. The coins original elemental data found in literature cannot be used as comparison or for the identification of coins in their present state [55]. However, XRF provides an excellent starting point to identify the composition of the surface products and therefore estimate the metallic alloy and additional elements introduced from the soil. XRF analysis was performed over the obverse and reverse of all coins in the study with several measurements taken in different areas to identify whether or not the corrosion on the surface was homogeneous. For coin D two different areas could be observed; green and orange, and so these were studied by XRF with the results from both sides of the coin combined and averaged as shown below:

Element	Composition/ %	Error/ ± %
Cu	80.81	0.59
Sn	11.71	0.50
Al	2.90	1.59
Zn	1.71	0.08
As	1.59	0.11
Fe	0.53	0.06
Bi	0.45	0.09
Sb	0.22	0.10
Ag	0.06	0.03
Zr	0.02	0.02
Mn	0.01	0.02

*Table 5.4: Average XRF Elemental Composition of green areas on coin D*

Element	Composition/ %	Error/ ± %
Cu	70.35	0.60
Al	16.34	3.06
Sn	9.15	0.48
Zn	1.49	0.08
As	1.35	0.11
Fe	0.71	0.07
Bi	0.37	0.09
Sb	0.16	0.09
Ag	0.05	0.03
Mn	0.03	0.02
Zr	0.01	0.02

*Table 5.5: Average XRF Elemental Composition of orange areas on coin D*

The results show that the major component of the surface was copper, and that this coin is composed of bronze, a Cu-Sn alloy. The green areas show a Cu-Sn alloy with an 81%-12% composition of bronze. There was  $2.90 \pm 1.59\%$  of aluminium present which could be part of the alloy or equally inclusion of soil elements as Al is a major constituent of soil D. The orange areas appear to be the introduction of sand from the soil and show a significantly higher amount of Al at  $16.34 \pm 3.06\%$ . The aluminium here could be included in elemental form or as part of a concretion of sandstone for example. The bronze components of copper and tin are still present as a majority on the orange areas at  $70.35 \pm 0.60\%$  and  $9.15 \pm 0.48\%$  respectively providing extra confirmation of the bronze origin of the metal. Copper and tin are lower in comparison to the green areas due to the inclusion of aluminium on the surface as XRF is sensitive to surface elements and not the bulk. All the other elements present in the analysis shown in tables 5.4 and 5.5 are exactly the same for both areas and are in similar amounts. There is no inclusion of the major soil element Si in the XRF analysis of coin D which is not surprising as examination took place in metals mode matching samples against internal alloy standards, however the following elements from soil D: Fe, Al, Zr, Zn, Mn and V, are all present demonstrating the influence of the burial environment on the surface of the coin.

It is expected that the corrosion products present on the coin are cuprite ( $\text{Cu}_2\text{O}$ ) or another copper oxide as these are the most common corrosion products to be found on archaeological bronzes. It is this porous oxide layer that allows the transportation of elements from the burial environment to the metal's surface, and so without a copper oxide layer the inclusion of Al, Fe, Zr and so on would not be possible. The presence of any secondary corrosion products cannot be commented upon as the elements present in these products will not be identified by the XRF analysis as they are too light to be detected. The outer stratum present on coin D will be composed of elements from the burial environment

with the corrosion products influenced by these elements and the conditions of the environment.

### **5.1.2.3 Visual characterisation**



*Figure 5.6: Photograph of the obverse of coin D*



*Figure 5.4: OM image of the obverse of coin D, x50 magnification*

The majority of the surface of the obverse is covered in a smooth lustrous dark green layer which resembles a metal surface with a very fine layer of corrosion. There are patches of lime green and cream varying in size across the bust and space between the bust and the inscription. An orange-brown coarse grainy sand is localised mainly around the circumference of the coin which is possibly the inclusion of the superficial deposits from soil D reported to include sandy-gravel of an orange-brown colour composed of quartz, flint and sandstone. The reverse of the coin has exactly the same appearance with a lustrous dark green layer and the inclusion of an orange-brown grainy sand from the soil. Once more the sand is localised around the circumference of the coin but in a larger quantity, appearing also round the outline of seated Britannia and across the surface in small patches as seen in figure 5.5.

The orange grainy sand appears to be the inclusion of quartz or sandstone and as the presence of an oxide layer is necessary for the diffusion of soil compounds the general green layer across the surface could be this oxide layer in the form of cuprite. Cuprite may take a different colour to the normal maroon patina as ultimately the colour depends on the elements from the soil. Copper oxides may have a lustrous surface, much like the green one seen in coin D, where secondary copper corrosion products tend to have a powdery appearance. Copper sulfates and carbonates can form a relatively even green patina and so it is possible that these secondary corrosion products are present; the SEM-EDS analysis will reveal if this is the case.



#### 5.1.2.4 SEM-EDS results

Analysis was performed across several sites on both sides of all the coins in this study with measurements taken across the entire surface to understand the formation of corrosion and whether this corrosion was localised or general. Coin D demonstrated two different morphologies that were seen across the entire surface on both the obverse and reverse.

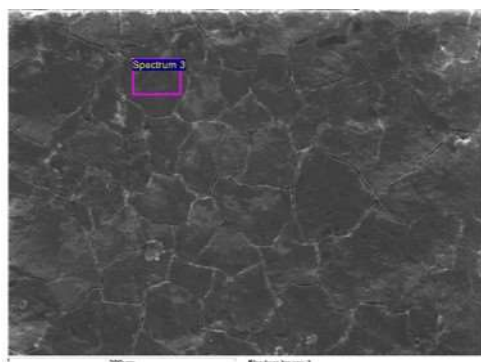


Figure 5.7: SEM image of area 1 on the obverse of coin D demonstrating site 3 of analysis

Element	Atomic percentage /%
O	82.02
Cu	8.79
Si	3.49
P	2.59
Sn	2.06
Ca	1.05

Table 5.6: SEM-EDS Elemental Composition of site 3 on area 1 of the obverse of coin D

The first type of morphology found on the surface of coin D is shown in figure 5.7 which is that of a very smooth and flat general surface layer broken up into slab like structures with a mottled surface effect. Between the slabs are cracks with some shallow surface cracks and others slightly deeper. Site 3 of analysis is taken on the centre of a smooth flat slab which is oxygen rich (82.02%) followed by copper (8.79%) and silicon (3.49%) in high amounts. Some of the oxygen present will be part of the initial copper oxide layer with the rest contamination from the air. The copper and tin present are as expected from the bronze alloy with the addition of silicon, phosphorus and calcium from the burial environment. The presence of phosphorus and calcium here supports their identification in the XRF graph for soil D as these elements have diffused from the environment into the metal via the cracks present along the patina.

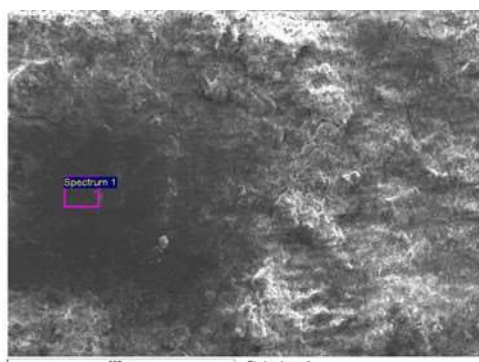
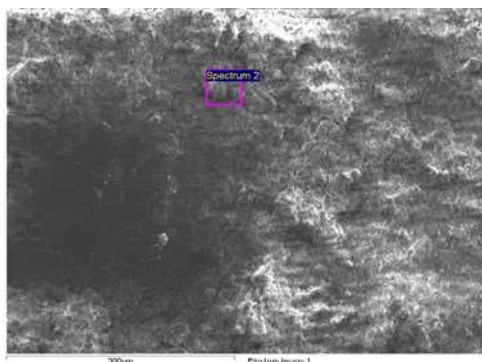


Figure 5.8: SEM image of area 1 on the reverse of coin D demonstrating site 1 of analysis

Element	Atomic percentage /%
O	64.58
C	22.97
Cu	5.33
Sn	2.40
P	1.80
Si	1.13
Al	0.82
Ca	0.41
Fe	0.35
Pb	0.21

Table 5.7: SEM-EDS Elemental Composition of site 1 on area 1 of the reverse of coin D





*Figure 5.9: SEM image of area 1 on the reverse of coin D demonstrating site 2 of analysis*

Element	Atomic percentage /%
O	53.81
C	28.92
Si	9.01
Al	3.96
Fe	1.38
Cu	1.36
Ca	0.53
Mg	0.52
K	0.51

*Table 5.8: SEM-EDS Elemental Composition of site 2 on area 1 of the reverse of coin D*

Figures 5.8 and 5.9 are of the reverse of the coin and show a slightly different morphology. These images were taken where the orange grainy sand was present next to the H on the reverse. The area of analysis in figure 5.8 is of the smooth flat uniform slabs like those found on area 1 of the obverse formed as an initial layer here. A grainy powder has developed on top of this layer in deposits of varying height with some loose individual crystalline grains. This area was analysed by EDS with the results in table 5.8. The analyses of sites 1 and 2 on area 1 of the reverse show oxygen and carbon as the elements present in the highest atomic amount from the oxide layer that developed on the metal, atmospheric contamination, sample preparation or secondary copper corrosion products. The powdery area shown in figure 5.9 shows a very high amount of silicon (9.01%) alongside other common soil elements such as Al, Fe, Ca, Mg and K in higher amounts than found in the analysis of site 1. The powder is therefore confirmed as the inclusion of the orange-brown coarse grainy sand that has diffused into the metals surface and formed an alteration layer. The analysis of site 1 of the smooth flat surface includes common soil elements P, Si, Al, Ca, Fe and Pb but at a much lower atomic percent than those in site 2. The elements from the soil do generally affect the surface with the inclusion of elements from soil D across all the analyses performed; however it is clear visually and with support from the EDS analysis that the heavy concretion of soil elements is localised. The addition of elements and compounds from the soil alters the morphology of the surface forming this grainy powdery layer on top of a general smooth layer high in oxygen and copper.

### 5.1.2.5 XRD results

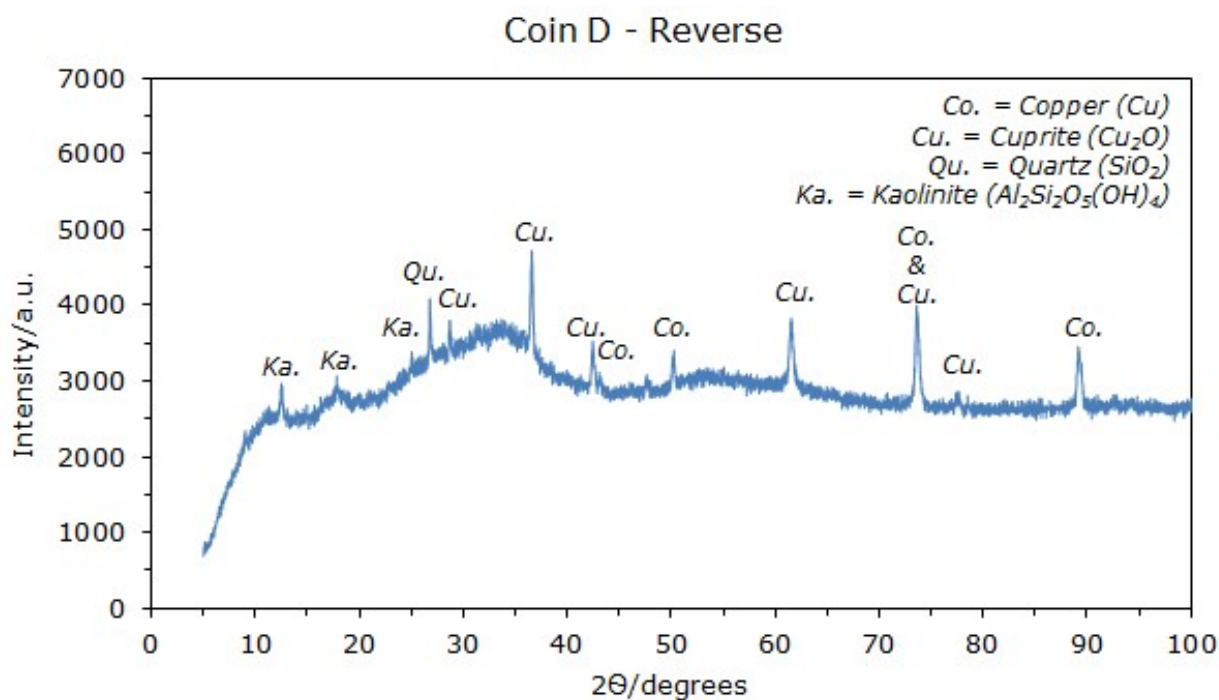


Figure 5.10: XRD pattern of the reverse of coin D

The XRD pattern revealed that the corrosion products on the surface of coin D were copper (Cu), cuprite ( $\text{Cu}_2\text{O}$ ), quartz ( $\text{SiO}_2$ ) and kaolinite ( $\text{Al}_2\text{Si}_2\text{O}_5(\text{OH})_4$ ) as the experimental d-spacing values of these minerals were found in the standard reference pattern of reflections in table 4.1. The four peaks at  $2.098\text{\AA}$  ( $43.13^\circ$ ),  $1.818\text{\AA}$  ( $50.18^\circ$ ),  $1.285\text{\AA}$  ( $73.71^\circ$ ) and  $1.097\text{\AA}$  ( $89.25^\circ$ ) represent the (111), (200), (220) and (311) planes of cubic face-centered copper. The six peaks at  $3.112\text{\AA}$  ( $28.68^\circ$ ),  $2.462\text{\AA}$  ( $36.50^\circ$ ),  $2.131\text{\AA}$  ( $42.41^\circ$ ),  $1.507\text{\AA}$  ( $61.52^\circ$ ),  $1.285\text{\AA}$  ( $73.71^\circ$ ) and  $1.231\text{\AA}$  ( $77.54^\circ$ ) represent the (110), (111), (200), (220), (311), and (222) planes of cubic simple cuprite. Quartz only shows one peak at  $3.328\text{\AA}$  ( $26.79^\circ$ ) with the other peaks not visible due to the background noise. The remaining three peaks are those of kaolinite at  $7.145\text{\AA}$  ( $12.39^\circ$ ),  $3.570\text{\AA}$  ( $24.94^\circ$ ) and  $4.998\text{\AA}$  ( $17.75^\circ$ ). The graph above is that of the reverse of coin D, the pattern for the obverse shows exactly the same products.

### 5.1.3 Conclusion of the burial environment's influence on the corrosion products

The Victorian Bun Head Farthing is bronze, a copper-tin alloy, with a protective cuprite layer formed initially as a very smooth and flat general layer. This cuprite layer visually appears as a lustrous dark green surface across the coin and its presence is confirmed by the identification of cuprite in the XRD analysis. The initial oxide layer was porous and allowed the diffusion of elements from soil D such as Al, Fe, Zr, Zn, Mn and V to the coin's surface. The inclusion of Si (the major component of soil D at 70%) was not found in the XRF analysis of the farthing but its existence is absolutely confirmed by the presence of quartz in

the XRD results from Coin D. The inclusion of quartz is as expected due to soil D being a loamy sand consisting of silica ( $\text{SiO}_2$ ) and the fact that the main crystalline product of the soil is quartz. The exterior grainy powdery layer of coin D (as shown in figure 5.9) that had a high amount of silicon and other common soil elements is that of the concretion of quartz and kaolinite rather than secondary corrosion products. The orange brown grainy sand found on the 1861 farthing is the loamy sand of soil D which diffused into the surface forming a localised heavy concretion of soil elements; the influence of the soils composition is seen over the entire surface as well as this localisation. The environment of soil D influenced the formation of any corrosion products on coin D and whether they were stable in the burial environment, the only product that was able to form under the burial conditions was cuprite; copper was also present as it was stable in the environment. The presence of these products was predicted by the Pourbaix diagram of copper where the reserve acidity of soil D at  $\text{pH } 6.51 \pm 0.02$ , representative of the burial conditions of the coin as found upon excavation, demonstrated that copper and cuprite along with  $\text{Cu}^{2+}$  and  $\text{Cu}^+$  were stable. Another sample coin C, had an adhering soil sample with very similar properties demonstrating the presence of quartz and other common soil elements. The corrosion products found on coin C were copper and cuprite only with no crystalline corrosion products from the soil. However, the XRF of coin C found silicon as the second highest component of the surface and so once again the influence of the burial environment is seen across this sample. The results for coin C are found in appendix F.

## 5.2 Primary copper corrosion products

### 5.2.1 Identification

The Roman coin - R06 was found in Thoresby, Newark where a substantial Roman settlement once was [39] and was successfully identified as a barbarous radiate with a possible minting date of AD 275 – 285. The coin weighed 1.7291g and measured 11.5mm or 12.8mm dependent on where the measurement was taken. Barbarous radiates were imitations of radiates and there was a huge rise in the number of these copies produced in Britain around AD 275 – 285 with the demise of the Gallic Empire. Initially radiates were composed of 50% silver falling to as little as 1% in the early AD 270s with their debasement to bronze throughout the 3<sup>rd</sup> century AD [56].



*Figure 5.11: OM image of the obverse of coin R06, x50 magnification*



*Figure 5.12: OM image of the reverse of coin R06, x50 magnification*

The prominent radiate crown that is worn by the emperor on the obverse in figure 5.11 leads to the conclusion that this is a barbarous radiate. The bust is right facing with the outline of the crown, face and neck visible including some inside details such as the ear, eye and nose. The reverse of the coin is quite worn and corroded, however it is possible to pick out several lines and dots as a pattern. Unfortunately, as seen in figure 5.12 there is not enough detail to unravel what the reverse design actually comprises. It is more than likely that the detail is that of an architectural type as buildings such as temples, structures and monuments were frequently depicted [56].

### 5.2.2 Results from XRF analysis

Element	Composition/ %	Error/ ± %
Cu	50.10	0.19
Sn	42.55	0.35
Pb	3.51	0.07
Fe	1.75	0.05
Pd	0.77	0.03
Rh	0.45	0.02
Zn	0.45	0.02
Sb	0.19	0.06
Ag	0.11	0.02
Ru	0.05	0.01
Ti	0.03	0.10
Mn	0.03	0.03
Co	0	0

*Table 5.9: Average XRF Elemental Composition of metal areas on R06*

Element	Composition/ %	Error/ ± %
Cu	49.80	0.19
Sn	42.85	0.36
Pb	3.65	0.07
Fe	1.73	0.05
Pd	0.77	0.03
Rh	0.45	0.03
Zn	0.40	0.02
Ag	0.20	0.03
Sb	0.18	0.06
Co	0.03	0.02
Mn	0.02	0.03
Ti	0	0
Ru	0	0

*Table 5.10: Average XRF Elemental Composition of green areas on R06*

The averages of the two different areas show that the coin was made from bronze as the major elements across the entire surface were copper and tin with only a 0.30% difference in each element across the areas. Pb and Fe also feature heavily on the surface of coin R06, again with extremely similar amounts across the surface. This trend continues as the minor and trace elements are present in almost the same amounts across the entire surface, with some exceptions, demonstrating a general homogenous layer. As this radiate has been identified as bronze it is evidence that it may be a barbarous radiate from the 3<sup>rd</sup> century as radiates were debased to bronze throughout this century. The silver content was found to be low across both areas with  $0.11 \pm 0.02\%$  on the metal areas and  $0.20 \pm 0.03\%$  on the green areas. As XRF does not measure the bulk metal this information cannot be used as concrete proof of the minting date of the coin. The surface of the coin has been altered through its lifetime due to corrosion and so in its current state is not a true representation of the composition of the original coin. What can be taken from this data is the composition of the surface products, allowing an estimation of the metallic alloy of the coin which in this case is bronze. It is possible that the bronze has been alloyed with lead or iron, although these elements could equally have been introduced into the metals surface by the burial environment. There are some common elements found in the soil such as Fe, Pb, Zn, Ti, Mn amongst others that were detected and so their inclusion is possibly via diffusion from the environment during corrosion. The corrosion products expected from the knowledge of the metallic alloy are copper oxides as an initial layer, then possibly secondary copper corrosion products such as copper carbonates and the incorporation of soil elements and compounds in the outer most layer.

### 5.2.3 Visual characterisation



Figure 5.13: Photograph of the obverse of R06



Figure 5.11: OM image of the obverse of coin R06, x50 magnification

The embossed design of the obverse has features such as the barbarous crown still visible with a lustrous dark green surface. The other areas present on the obverse are at a lower level and show a multi-coloured thicker corrosion layer with several surface pits of lime green and cream with a powdery appearance. There is also a creamy light brown grainy sand localised round the edges of the embossed design but also found across the surface. A darker green corrosion product is found near the lime green pits and generally towards the edges of the coin.



Figure 5.14: Photograph of the reverse of R06



Figure 5.12: OM image of the reverse of coin R06, x50 magnification

The reverse of coin R06 includes the grainy sand in abundance across the entire surface in a brighter orange colour with some localisation as an outline to the embossed detail. The embossed design once more shows a lustrous dark green surface. The lime green corrosion found on the obverse is present on a larger scale with surface pits of varying sizes and



some localisation towards the edges of the coin. This coin has a more severe and coarse corrosion layer in comparison to coin D with the presence of localised pitting.

Coin R06 exhibits a similar lustrous green surface to the one in coin D, and so it is predicted that this general layer is that of cuprite showing a different colour due to the influence of the burial environment. The inclusion of quartz or other soil compounds are expected as generally most archaeological finds incorporate soil elements into their exterior layer. There is a possibility that copper chlorides are present on the surface with the localised pits of lime green commonly associated with these corrosion products. Equally other secondary copper corrosion products such as copper carbonates could contribute to this green colour (although this does not tend to form in pits). The XRF results cannot shed any light onto what this lime green alteration product could be, however the SEM-EDS and XRD results will provide some conclusions.

#### 5.2.4 SEM-EDS results

Area 3 of the reverse (Figs 5.15 & 5.16) almost mirrors the morphology of coin D seen in figures 5.8 and 5.9 showing relatively flat and smooth slabs with an exterior powdery, lumpy area. As well as this morphology there were also areas that showed just a relatively general flat and smooth slab like surface similar to figure 5.7 of coin D.

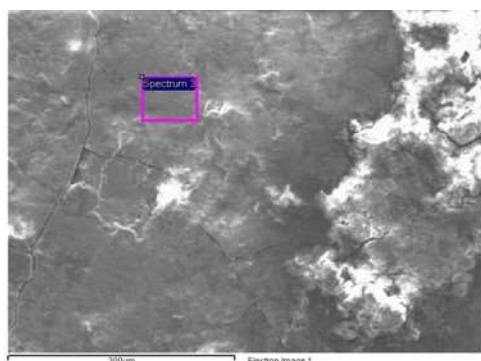


Figure 5.15: SEM image of area 3 on the reverse of R06 demonstrating site 3 of analysis

Element	Atomic percentage /%
O	67.53
C	16.12
Cu	4.79
Sn	4.38
P	2.76
Al	2.19
Si	1.29
Ca	0.55
Fe	0.39

Table 5.11: SEM-EDS Elemental Composition of site 3 on area 3 of the reverse of R06

The analysis of site 3 incorporates the smooth and flat slabs with a slight mottling of the surface, shallow surface pits and small individual powder grains as seen in figure 5.15. As shown in table 5.11 the surface was made up of oxygen and carbon as a majority followed by copper and tin with the inclusion of elements from the soil such as P, Al, Si, Ca and Fe. The 67.53% of oxygen was present as part of the initial oxide layer on the surface as well as from atmospheric contamination. Copper and tin come as one of the major elements found on the surface as expected for bronze. Visually, the smooth surface does not appear to have been heavily influenced by elements in the burial environment with no powder

present on the surface, however there is a large amount of typical soil elements such as P, Al and Si followed by minor amounts of Ca and Fe. Analysis was also performed on the raised powdery layer formed on the initial smooth flat surface.

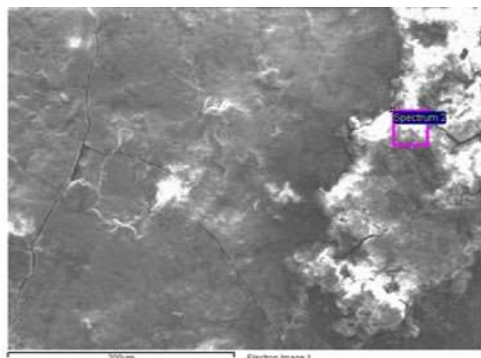


*Figure 5.16: SEM image of area 3 on the reverse of R06 demonstrating site 2 of analysis*

Element	Atomic percentage /%
O	57.43
C	29.17
Si	5.30
Al	5.03
P	1.07
Cu	0.73
Ca	0.33
Sn	0.33
K	0.29
Fe	0.23
Pb	0.07

*Table 5.12: SEM-EDS Elemental Composition of site 2 on area 3 of the reverse of R06*

This raised area consisted of oxygen and carbon mostly, but then instead of copper and tin taking up the majority of the surface as found in the previous analyses, silicon is in abundance. There is substantially more aluminium and phosphorus present on this site demonstrating the influence of the burial environment upon this area. Copper and tin are still present but in smaller amounts as the majority of the surface is covered by the powder alteration product. Ca, K, Fe and Pb are also present from the soil but in trace amounts in similar percentages to the other slabbed areas. The EDS analysis of this area proves that area 3 does not just have the same morphology as coin D, that it also has a very similar composition. Therefore, it is highly likely that as with coin D this grainy powdery layer is that of the heavy concretion of soil elements.

The SEM image of the reverse, figure 5.17, was taken of the creamy/green surface pit shown in figure 5.12 and shows a coarse morphology with severe corrosion. The area is very powdery looking with several lumps and lots of raised areas. There are small deep pits visible with individual powder granules in some and other pits completely dark with the bottom not visible. There are some smoother looking slabs present similar to those found throughout this sample and in coin D.



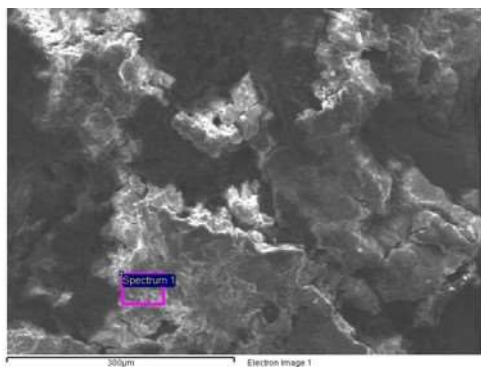


*Figure 5.17: SEM image of area 2 on the reverse of R06 demonstrating site 1 of analysis*

Element	Atomic percentage /%
O	34.48
C	34.08
Cu	24.15
Al	2.52
Cl	1.81
Sn	1.80
Si	1.16

*Table 5.13: SEM-EDS Elemental Composition of site 1 on area 2 of the reverse of R06*

Site 1 of area 2 is of a slightly powdery raised slab with circular lumps, the layer underneath the slab is smooth and flat as seen previously. This area again has a high amount of carbon and oxygen present on the surface as well as a high copper content and the presence of tin as part of the bronze base metal. The EDS analysis detected typical soil elements such as aluminium in 2.52% followed closely by chlorine in 1.81% and silicon in 1.16%. The fact that chlorine is present in a relatively high amount in this area explains why the morphology of this surface in general appears much more coarse and rough. When copper is in an environment that is chlorine rich, the copper artefact becomes unstable as the chlorine ions break down the oxide layer causing pitting and further damage to the surface as visualised here.

### 5.2.5 XRD results

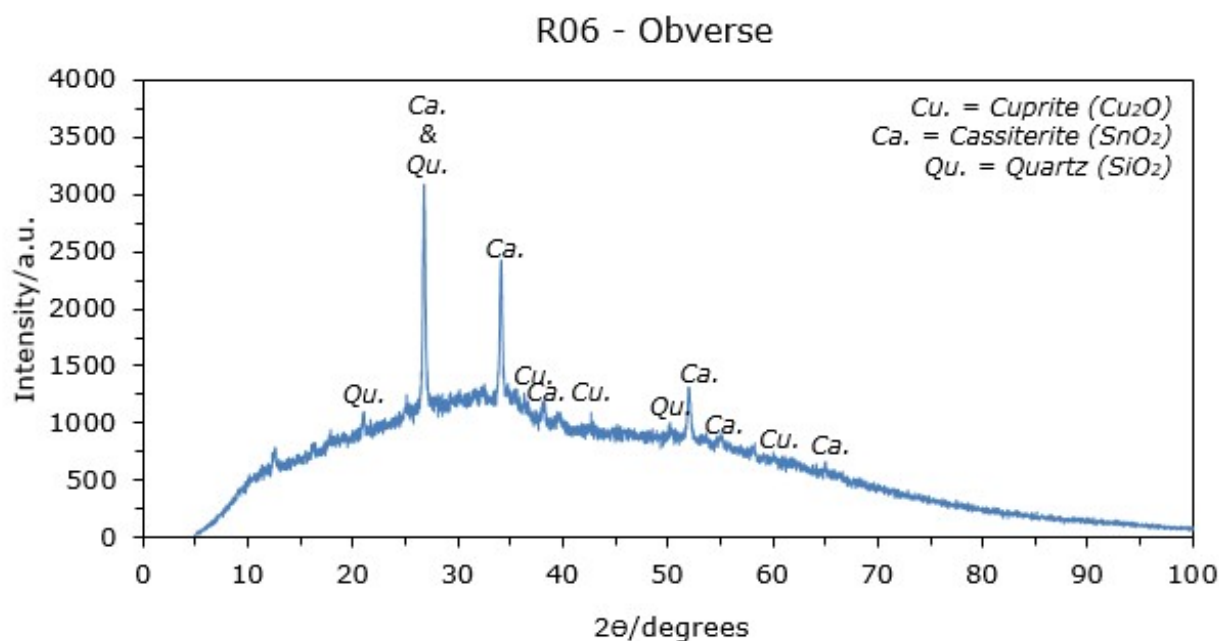


Figure 5.18: XRD pattern of the obverse of coin R06

The surface of R06 contains cuprite ( $\text{Cu}_2\text{O}$ ), Cassiterite ( $\text{SnO}_2$ ) and quartz ( $\text{SiO}_2$ ) as the d-spacing values for these minerals found in table 4.1 are present in the XRD experimental data above. The pattern collected of the reverse of the coin shows exactly the same minerals. Cuprite has three peaks in the XRD graph above at  $2.468\text{\AA}$  ( $36.40^\circ$ ),  $2.118\text{\AA}$  ( $42.69^\circ$ ) and  $1.530\text{\AA}$  ( $60.52^\circ$ ) for the (111), (200), (220) planes of cubic cuprite. The peaks at  $3.313\text{\AA}$  ( $26.89^\circ$ ),  $2.629\text{\AA}$  ( $34.10^\circ$ ),  $1.759\text{\AA}$  ( $51.98^\circ$ ),  $2.352\text{\AA}$  ( $38.17^\circ$ ),  $1.668\text{\AA}$  ( $55.03^\circ$ ) and  $1.435\text{\AA}$  ( $64.87^\circ$ ) represent cassiterite. The two peaks at  $3.313\text{\AA}$  ( $42.69^\circ$ ) and  $1.811\text{\AA}$  ( $50.31^\circ$ ) are those of quartz, the remainder of the full pattern will not be visible due to background noise.

Archaeological bronzes tend to include a copper oxide layer such as cuprite (as found here); the presence of tin oxide is also identified as a corrosion product on coin R06. There are several explanations as to why tin oxide has formed on this particular sample, there is a higher tin content on this sample so more availability to react; a tin enriched layer could have formed with copper selective corrosion once again providing a large amount of tin for reaction. Ultimately, the burial environment influences what will form by providing the mechanism for corrosion and supporting the products that are thermodynamically stable, cassiterite was able to form in the environment and remain stable.

### **5.2.6 Conclusion**

Coin R06, a Barbarous radiate, was made from bronze a Cu-Sn alloy confirmed by all analysis undertaken on the sample. This sample demonstrated a similar morphology and composition to that of coin D, starting with a smooth flat slab like surface with a high oxygen and copper content accompanied by a high atomic percentage of tin. This initial smooth layer is that of cuprite, with an addition of tin oxide in the form of cassiterite as this corrosion product was able to form in the burial environment and remain stable. The oxide layer has once again formed as a lustrous dark green surface and it is this porous oxide layer that allowed the diffusion of soil elements such as Si, Al, P, Ca, K, Fe and Pb to form a second stratum. This exterior layer formed on top of the oxide layer with the appearance of a grainy powder under the SEM and visually as an external grainy sand localised round the edges of the coin. In this powdery area there is a higher content of Si as well as other common soil elements in comparison to the initial layer, showing a heavy inclusion of these elements in certain areas; however the burial environments affect is surface wide. Quartz is identified as a crystalline corrosion product of the coins surface further demonstrating this influence. The crystalline compounds present on R06 show primary corrosion products (metal oxides) and the deposits of soil compounds (quartz). Initial observations led to the prediction that copper chlorides were present on the surface in the lime green localised pits; XRD investigations revealed that there were no secondary chlorine compounds on the surface. XRD analysed the surface of these coins only and so there is a possibility that chlorine compounds could have formed internally in the metal and so not identifiable by the surface sensitive techniques. Chlorine was found across the surface in the SEM-EDS analysis and so is present on the surface elementally localised in the lime green pits rather than as a chloride layer of corrosion. Identifying this chlorine on the surface is vital for further conservation as not controlling the humidity of the environment of where this artefact would be stored, could lead to bronze disease and the complete destruction of the object.

## 5.3 Secondary copper corrosion products

### 5.3.1 Identification

Coin R02 is from the Roman era, and is either a radiate or a barbarous radiate minted more than likely in AD 275 – 285 if the latter is true, however this coin could have been produced at any time between AD 238 – 296. Further evidence of its Roman heritage comes from the fact that the place of its find was in the vicinity of the Fosse Way and the Roman town of Crococalana [41].



*Figure 5.19: OM image of the obverse of coin R02, x50 magnification*



*Figure 5.20: OM image of the reverse of coin R02, x30 magnification*

The spikes of a radiate crown are just visible to the naked eye on the obverse and so evidence that this is a radiate coin of some sort. Also visible is the outline shape of the head of a right facing bust as well as the outline of an eye. On the reverse of the coin there are some raised areas that look like a reclined figure possibly seated on a chair. Apart from this detail, there is not much more available to support the identification of whether this coin is a barbarous radiate or radiate [56]. The diameter of this coin is 16.8mm or 21.6mm dependent on where the measurement was taken and the weight of the coin was 2.3024g.

### 5.3.2 Results from XRF analysis

Element	Composition/ %	Error/ ± %
Cu	82.60	0.64
Pb	7.15	0.42
Sn	5.26	0.56
Al	2.15	1.15
Fe	1.88	0.08
Pd	0.42	0.14
Ti	0.16	0.03
Ni	0.16	0.05
Zn	0.10	0.06
Zr	0.09	0.04
Co	0.04	0.02
V	0	0.02
As	0	0
Sb	0	0
Mn	0	0
Bi	0	0
Si	0	0
Ag	0	0
Cr	0	0

*Table 5.14: Average XRF Elemental Composition of green areas on R02*

Element	Composition/ %	Error/ ± %
Cu	73.89	0.57
Al	6.53	2.54
Pb	5.35	0.45
Si	5.20	0.47
Sn	4.64	0.36
Ag	1.94	0.16
Fe	1.71	0.09
Zn	0.17	0.05
As	0.14	0.07
Sb	0.12	0.07
Ti	0.10	0.02
Ni	0.10	0.03
Co	0.05	0.02
Mn	0.04	0.03
Cr	0.03	0.01
Bi	0.02	0.05
Zr	0.01	0.01
V	0.00	0.01
Pd	0	0

*Table 5.15: Average XRF Elemental Composition of orange crust on R02*

Averages were taken of the two visually different areas which were the green regions across the surface of the sample and the orange crust. All XRF analyses revealed that the coin was made from copper with an 82.60% coverage of the orange crust and 73.89% of copper on the green regions. It is unclear if this copper was alloyed with lead, tin or aluminium or all three as the amounts of these elements vary in different areas. It is probable that lead has been alloyed with the copper as it is in a relatively high amount across both areas at 7.15% and 5.35%. Tin may also have been alloyed as there was 5.26% and 4.64% in the orange and green areas respectively; it would be expected that the amounts of metal in the metallic alloy would be similar across all areas. Al and Si are found across the surface but in varied amounts, probably an inclusion from the soil rather than part of the base metal. As seen in the two tables above there are a few different elements present in varied amounts across the surface that will have been introduced into the metal at some point during its lifetime either before or during burial. It is clear that this coin is copper with lead and tin possibly alloyed to increase the metals properties. Elements that are found naturally in the soil have been introduced into the coins surface with the presence of aluminium, silicon, iron, silver, zinc and many more common soil elements found on the coins surface.

At this stage, the only thing that can be said for the corrosion on the surface is that it will consist of a copper oxide such as cuprite, with the inclusion of soil elements and compounds such as quartz. There is a possibility that secondary copper corrosion products will be

present such as carbonates, sulfates or chlorides; this however will only be revealed with the information provided by the SEM-EDS and XRD results.

### **5.3.3 Visual characterisation**



*Figure 5.21: Photograph of the obverse of R02*



*Figure 5.19: OM image of the obverse of coin R02, x50 magnification*

A general dark green layer that appears to have formed initially was present on the obverse with some areas having a vaguely lighter tone; a large slightly raised area in the centre was darker green in colour. Small clear shiny crystals were present over the entire surface. A raised orange brown coarse crust consisting of brown and clear rounded crystals/grains was located over the left hand side of the original circumference (as shown in the image above). The crust does expand out across the surface but concludes before the raised green area in the centre. The brown and clear rounded crystals/grains are found individually across the surface and in clumps. A small area of black smooth fine corrosion can be seen at the bottom left.



*Figure 5.22: Photograph of the reverse of R02*



*Figure 5.20: OM image of the reverse of coin R02, x30 magnification*

The reverse of the coin has a similar appearance with an initial fine green layer that has a darker tone towards the bottom and a paler tone towards the top. There is a raised crust on the right hand side consisting of brown and clear rounded crystals/grains as on the obverse. Again, the crystals are also found individually across the surface and in clumps with a darker brown colour in comparison to the obverse, there are clear shiny crystals also present over the entire surface as before. There is a large orange crystal embedded in the crust which is probably the concretion of a compound from the soil such as quartz. There are lots of grainy pebbles present that are sand like; as the main constituent of sand is quartz the inclusion of  $\text{SiO}_2$  is highly probable. Again, the initial green layer is probably cuprite as found in coin D and R06 with similar colours.

### 5.3.4 SEM-EDS results

The two images shown below of the site analysis on area 4 of the reverse of R02 demonstrate a common trend for the surface of this coin. This trend is that the area with a smoother powdery appearance formed as a general surface layer (figure 5.23) has a high amount of oxygen, copper and carbon with the inclusion of common soil elements such as silicon in lower amounts. The surface is made up of oxygen and carbon as expected from atmospheric contamination, sample preparation and the presence of an oxide layer on the metal. Copper is in 5.06% abundance further evidence that this coin was made from copper. Silicon, iron, phosphorus and aluminium are present showing the influence of the burial environment over the entire surface. The inclusion of smooth crystals on the surface (figure 5.24) demonstrate a very high oxygen and silicon content. The analysis of the smooth crystal below (figure 5.24) shows only silicon and oxygen on the surface in a 1:2.47 atomic ratio having the correct amount required for a crystal of quartz ( $\text{SiO}_2$ ), with an abundance of oxygen from atmospheric contamination.

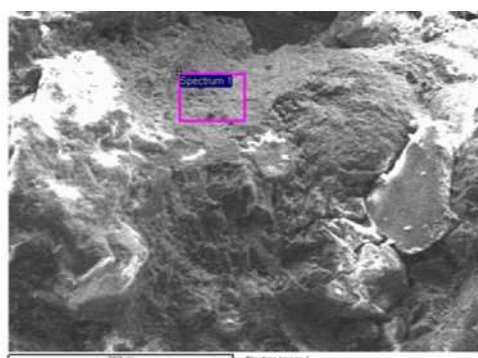


Figure 5.23: SEM image of area 4 on the reverse of R02 demonstrating site 1 of analysis

Element	Atomic percentage /%
O	56.76
C	31.50
Cu	5.06
Si	4.18
Fe	1.13
P	0.84
Al	0.52

Table 5.16: SEM-EDS Elemental Composition of site 1 on area 4 of the reverse of R02



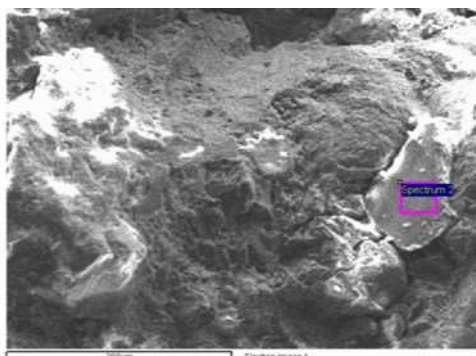


Figure 5.24: SEM image of area 4 on the reverse of R02 demonstrating site 2 of analysis

Element	Atomic percentage /%
O	71.16
Si	28.84

Table 5.17: SEM-EDS Elemental Composition of site 2 on area 4 of the reverse of R02

Area 2 of the obverse is where the crystals are present on the crust and the SEM images show that the majority of the surface consists of circular lumps and squarer crystal lumps. The lower areas are very powdery and grainy with some crystalline lumps and shallow surface pitting. The lower powdery and grainy area shown below in figure 5.25 had a surface mainly composed of carbon and oxygen (outside influence, the oxide layer) with a high copper content (the metal surface) and a relatively large amount of silicon (burial environment influence). As this is of a lower stratum it is highly possible that this is an initial copper oxide layer. The analysis of the large circular lump embedded in the surface of the coin shown in figure 5.26 is that of quartz. The EDS results show that the site analysed consists mainly of oxygen and silicon – the constituents of quartz, along with other common soil elements such as Al, Fe, P and K. It is clear that the burial environment has had a major impact on the surface of this particular coin with the concretion of compounds and diffusion of minerals into the surface layer.

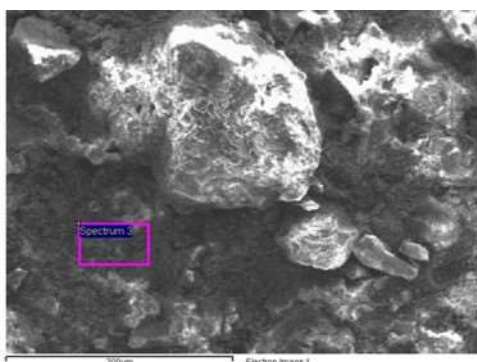


Figure 5.25: SEM image of area 2 on the obverse of R02 demonstrating site 3 of analysis

Element	Atomic percentage /%
O	35.86
C	34.14
Cu	23.23
Si	6.77

Table 5.18: SEM-EDS Elemental Composition of site 3 on area 2 of the obverse of R02



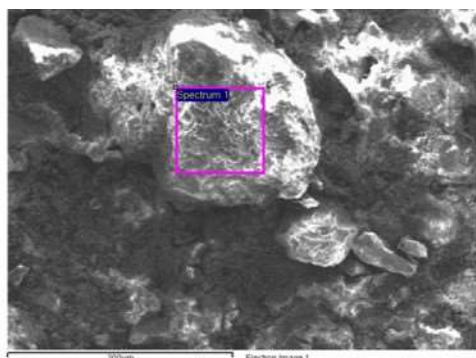


Figure 5.26: SEM image of area 2 on the obverse of R02 demonstrating site 1 of analysis

Element	Atomic percentage /%
O	65.53
Si	19.38
C	11.50
Cu	1.14
Al	0.94
Fe	0.79
P	0.44
K	0.28

Table 5.19: SEM-EDS Elemental Composition of site 1 on area 2 of the obverse of R02

It is clear that the copper coin here has suffered a more coarse and severe corrosion which could mean that secondary copper corrosion products are present on the surface. The secondary copper corrosion could only be that of a copper carbonate due to the fact that Cl and S have not been identified as constituents of the surface, therefore chloride and sulfate alteration products would not be found as external layers. The presence of an initial cuprite layer is supported by the abundance of oxygen and the inclusion of copper in the data. It is apparent that the soil has influenced this coins surface greatly with typical soil elements across the entire surface and quartz concretions across the crust and surface.

### 5.3.5 XRD results

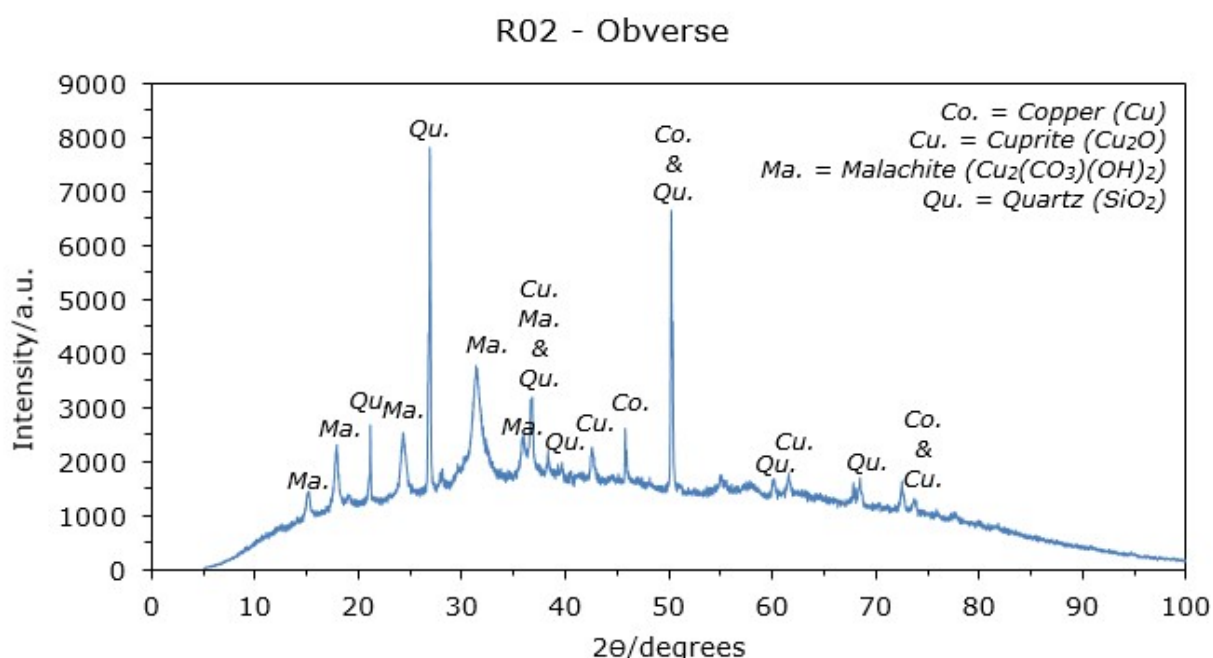


Figure 5.27: XRD pattern of the obverse of coin R02

The XRD pattern confirms that the surface of coin R02 has primary and secondary copper corrosion products as well as compounds from the soil with copper, cuprite, malachite and

quartz identified. Copper had three peaks present at  $1.982\text{\AA}$  ( $45.79^\circ$ ),  $1.818\text{\AA}$  ( $50.18^\circ$ ) and  $1.286\text{\AA}$  ( $73.64^\circ$ ) for the (111), (200) and (220) planes of cubic face-centered copper. The first four peaks of cuprite's reference pattern were found at the following intensities:  $36.61^\circ$  ( $2.454\text{\AA}$ ),  $45.79^\circ$  ( $2.126\text{\AA}$ ),  $61.45^\circ$  ( $1.509\text{\AA}$ ) and  $73.64^\circ$  ( $1.286\text{\AA}$ ) representing the planes (111), (200), (220) and (311) of the cubic face-centered structure. The diffraction pattern for quartz found in table 4.1 is found in its entirety with all seven peaks labelled. Finally, malachite, a secondary copper corrosion product was identified by its characteristic d-spacing values.

### **5.3.6 Conclusion**

The barbarous radiate, coin R02, was copper, and it was unclear if this copper was alloyed with elements such as lead, tin or aluminium as the XRF measurements revealed a lot of elemental variation on the surface. The morphology of the corrosion on coin R02 was different to the other copper coins discussed previously, as a smooth powder is seen as the general layer. This smooth general layer of powder had a high oxygen and copper content, similar to the smooth flat general layers on the other coins, and was identified as cuprite visually possessing a general dark green layer (the colour influenced by the burial environment). The smooth powder layer also had common soil elements across the entire surface. The XRD of coin R02 confirmed the metal of the coin as copper and the presence of an initial cuprite layer. Quartz was also identified by XRD which is visually seen as the crystal concretions embedded in the orange crust of the coin. The quartz concretions have a smooth crystal slab appearance under the SEM with a high silicon and oxygen content along with other elements from the soil such as Si, Al and Fe. A secondary copper corrosion product was present in the form of malachite, a copper carbonate, supported by the high content of carbon over the entire surface and the absence of other elements present in chloride and sulfate alteration products. The presence of malachite accounts for the severe powdery corrosion seen visually under the OM and the SEM-EDS.

## 5.4 Summary of Copper Coinage Results

The table below summarises the corrosion products of all the copper alloy samples studied in this project as well as the coins composition.

	Coin sample	Coin Composition	Crystalline corrosion products identified		
			Primary corrosion products	Secondary corrosion products	Soil compounds
Roman	R06	Cu-Sn	Cuprite ( $\text{Cu}_2\text{O}$ ) Cassiterite ( $\text{SnO}_2$ )		Quartz ( $\text{SiO}_2$ )
	R02	Cu	Cuprite ( $\text{Cu}_2\text{O}$ )	Malachite ( $\text{Cu}_2(\text{CO}_3)(\text{OH})_2$ )	Quartz ( $\text{SiO}_2$ )
	R294	Fe-Cu	Goethite ( $\alpha\text{-FeOOH}$ )		Quartz ( $\text{SiO}_2$ )
	R253B	Sn-Cu	Cassiterite ( $\text{SnO}_2$ )		
	R03	Cu-Sn	Cassiterite ( $\text{SnO}_2$ )		
Modern	V186	Cu-Sn	Cuprite ( $\text{Cu}_2\text{O}$ )		Quartz ( $\text{SiO}_2$ )
	V112	Cu	Cuprite ( $\text{Cu}_2\text{O}$ )		
	V114	Cu	Cuprite ( $\text{Cu}_2\text{O}$ )		
	Coin C	Cu	Cuprite ( $\text{Cu}_2\text{O}$ )		
	Coin D	Cu-Sn	Cuprite ( $\text{Cu}_2\text{O}$ )		Quartz ( $\text{SiO}_2$ ) Kaolinite ( $\text{Al}_2\text{Si}_2\text{O}_5(\text{OH})_4$ )

Table 5.20: Summary of composition and corrosion products of all copper coins in the study

The majority of the copper coins in the study had cuprite present as an initial layer; as expected. In the absence of this cuprite layer, another metal oxide would take its place such as cassiterite which was the case in a couple of the Roman coins as they were Cu-Sn alloys with a high percentage of Sn. Sample R06 had cassiterite as an initial oxide layer formed alongside cuprite, as tin was a major component of the surface and cassiterite was able to form and remain stable in the burial environment. The inclusion of quartz from the burial environment was another product that was commonly found in most of the coin samples; one sample, coin D, also showed the compound kaolinite that had been introduced by the soil. Alongside cuprite and quartz sample R02 exhibited secondary corrosion products in the form of the copper carbonate malachite. Coin R294 was a copper alloy that had a majority of iron on the surface and so in this sample goethite was the alteration layer to form alongside quartz. The modern coins all exhibit the major corrosion product cuprite, whereas the roman coins all have differing initial metal oxides on the surface; this is not to do with the age of the coins or the type of burial environment they were in. Even though the burial environment is a major influential factor over which corrosion products will form and remain stable it is in fact the metal alloy that is key in establishing what will form. The coins R02, V112, V114 and Coin C of a purer copper nature along with bronze coins D and V186, that had a majority of copper on the surface >70%, all formed cuprite. Coin R06 had near equal amounts of Cu and Sn in its alloy and so it is unsurprising that both cassiterite and cuprite formed, it is important however to remember that even though the alloy provided the tin for

reaction it was ultimately the conditions of burial that allowed formation of both oxides. R253B had a higher amount of tin and R03 had ~10% less tin than its copper counterpart and so formed cassiterite, R294 had an iron majority and therefore goethite formed.

The major morphological features of all the copper alloy coins followed a similar pattern, a general attack of the entire surface with no localised corrosion was observed in all cases. All coins exhibited a general initial layer of corrosion high in oxygen which was more powdery than smooth in some cases. The initial oxide layer formed on top of the metal core with the inclusion of some elements from the soil such as Si and P. In most cases there were concretions of compounds from the soil formed as an external layer, R294, R253B and R03 did not demonstrate such inclusions. The soil alteration layer formed as an external powder or slab like structures and was significantly higher in common elements from the soil. In the case of R02, this external layer also included secondary corrosion directly influenced by the burial environment.

It is clear that the corrosion products and morphology of the copper alloy samples all followed a similar pattern and the age of the samples did not affect this. The metal alloy was key in influencing which type of metal oxide would be produced but it was the burial environment that ultimately influenced what would form and remain stable; its effect seen surface wide. An initial metal oxide will always form as a general layer on a copper alloy followed by any secondary corrosion and the inclusion of any soil compounds.

## Chapter 6 - Silver Coinage Results

The results presented in chapter 6 are those of the following samples: burial environment A, Coin B, M516 and V106. The three silver coins are all from varying historical periods with Coin B identified as Roman, M516 Medieval and V106 'Modern'.

Coin B was chosen for discussion with burial environment A firstly to identify the influence the soil had on the corrosion of this coin and therefore apply this knowledge to the remainder of the silver samples in this study. Another silver coin, Coin A, found in the same burial environment has its results in appendix F.

Coin M516 was presented as the second set of results displaying a layer of silver and only one corrosion product Chlorargyrite; the general exterior layer present on most silver coins in this study and so representative of the majority. The results of the remaining silver coins are presented in appendix F.

The final sample chosen for discussion was coin V106 as this was a silver-copper alloy, the only silver alloy in the study, and demonstrated different corrosion types such as galvanic corrosion as found in the literature.

The presentation of results follows the order taken for the copper coins; the heritage of the coin is firstly established, the base metal alloy identified by XRF and then an estimate of the corrosion products based on the visual interpretation and previous knowledge of corrosion products for the specific alloy is formed. SEM-EDS analysis reveals the elements present on the surface with further conclusions drawn about the possible corrosion products with the absence or presence of certain elements. XRD analysis then confirms absolutely the presence of the corrosion products on the surface rendering any earlier predictions true or false.

## 6.1 Silver Coinage corrosion with adhering soil samples

### 6.1.1 Burial environment A

#### 6.1.1.1 Results for burial environment A

Soil	Colour	Texture
A	10YR 3/2	Loamy sand

Table 6.1: Visual analysis of soil A

pH test	Average	Error
Water	6.23	0.03
CaCl <sub>2</sub>	5.68	0.01

Table 6.2: pH measurements for soil A

Element	Composition/%	Error/± %
Si	75.30	1.50
Fe	11.10	0.30
Al	10.50	1.20
Ti	1.73	0.05
Pd	0.86	0.07
Zr	0.24	0.02
Mn	0.17	0.11
Cu	0.10	0.03
V	0.06	0.03
Zn	0.05	0.02
Ni	0.00	0.03

Table 6.3: XRF Elemental Composition of soil A

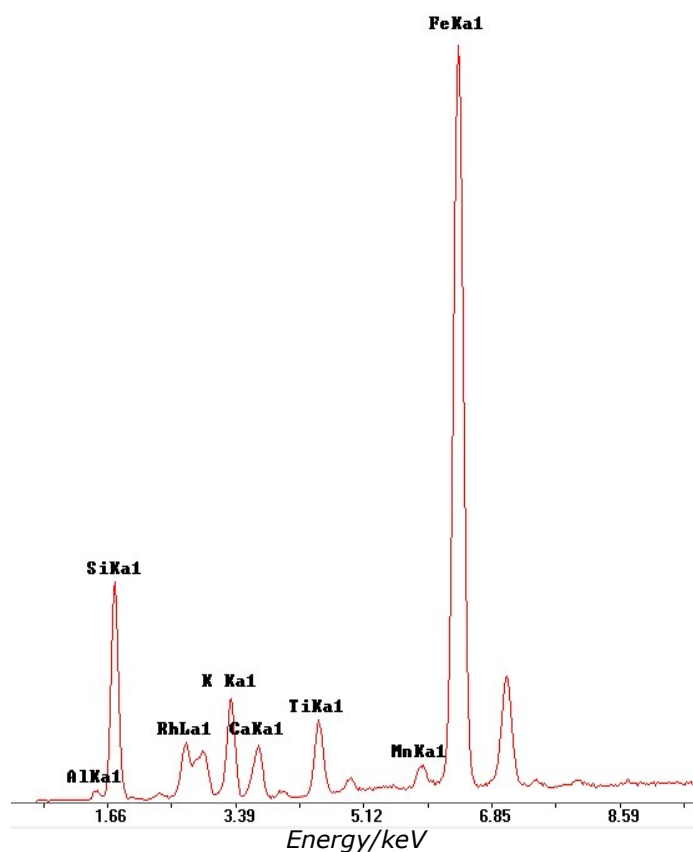


Figure 6.1: XRF pattern of soil A

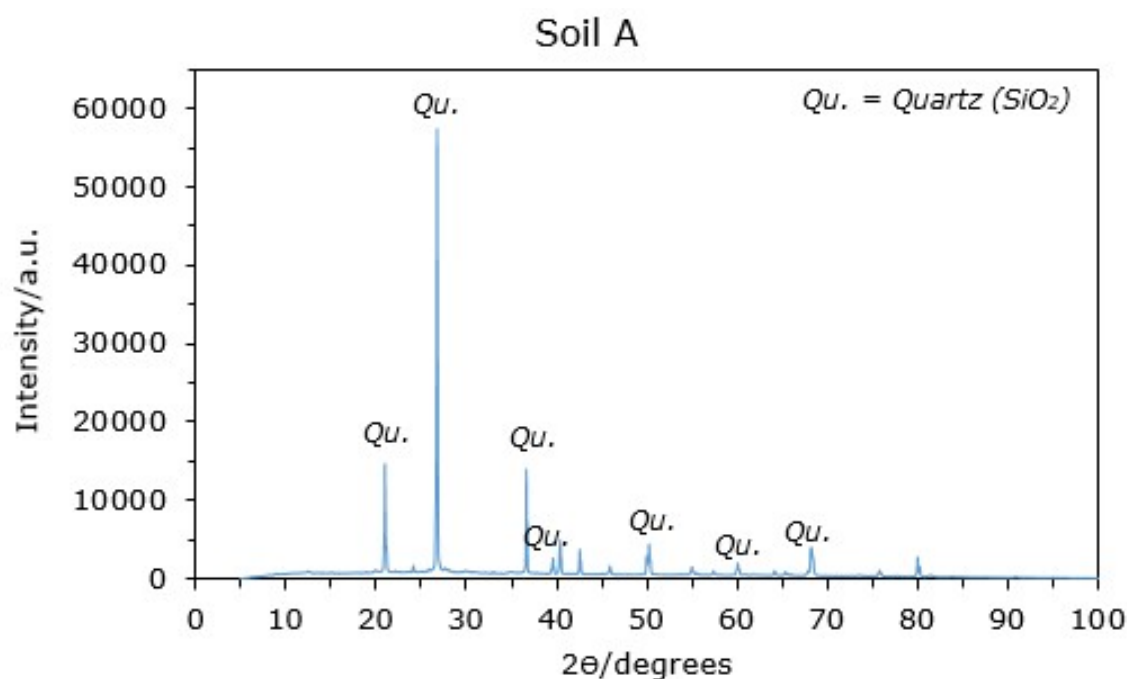


Figure 6.2: XRD pattern of soil A

#### 6.1.1.2 Discussion for burial environment A

Soil A was identified as a loamy sand with a very dark greyish brown colour including yellow sandy flecks (10YR 3/2). The BGS recorded the lithology of the bedrock in the area that soil A was found to contain grey to black mudstone with underlying limestone and sandstone correlating with the colours identified. With the textural category identified as a sand preliminary compositional information can be estimated as silica usually in the form of quartz is the most common constituent of sand.

The results of the XRF support this prediction as the major component found in soil A was silicon with a composition of  $75.30 \pm 1.50\%$ . Soil A also consisted of  $11.10 \pm 0.30\%$  of iron,  $10.50 \pm 1.20\%$  of aluminium,  $1.73 \pm 0.05\%$  of titanium, with minor elements Pd, Zr and Mn and trace elements Cu, V, Zn and Ni. The total elemental composition of soil A was 100.10% and included typical soil elements reported in literature. The XRF spectrum above in figure 6.1 shows Ka peaks for the major elements Si, Fe, Al and Ti and minor element Mn. The other minor and trace elements do not show any Ka or La lines. The spectrum had unassigned peaks where the Ka lines for K and Ca fell, these elements weren't identified in the data but being typical soil elements found in literature were labelled. The presence of Rh La lines on the spectrum is due to Rayleigh scatter.

Figure 6.2 shows the XRD pattern of soil A and correlates perfectly to the full diffraction pattern of quartz (SiO<sub>2</sub>) with respect to the peak positions as shown in table 4.1 in chapter 4. Again, this is as expected as soil A is a loamy sand and the most common constituent of

sand is quartz; it is also supported by the geographical position of the finds as the sedimentary bedrock incorporated silica minerals into the soil.

The pH of the active acidity of the soil (table 6.2) had an average pH of  $6.23 \pm 0.03$  (raw data found in appendix D). The loamy sand is slightly acidic as expected due to the fact that a pH of between 5 to 7 is needed to support crops and pasture; plant nutrients are also in their most available state in this region. Usually the pH of soil varies between 5 and 9, however most soils are naturally acidic [36, 57]. The reserve acidity is expected to be lower than the active acidity due to a cation exchange taking place, this trend seen in soil A's results as the reserve acidity had an average pH of  $5.68 \pm 0.01$  (raw data found in appendix D) which is lower than the active acidity. The reserve acidity will be more representative of the soil in the field upon excavation and so it is more feasible to assume that the more acidic pH of  $5.68 \pm 0.01$  influenced the corrosion of any coins found in the burial environment.

Pourbaix diagrams can assist in predicting what will happen to the metal in its burial conditions based on the pH of the environment. The diagram for silver in seawater below demonstrates that at a pH of  $\sim 5.68$  (where the red line has been drawn) AgCl and Ag<sub>2</sub>S will be able to form, potential dependent, as well as Ag being stable. However, there are many components to consider that will influence the corrosive environment and which corrosion products will form and therefore, it is difficult to predict what will happen under burial conditions.

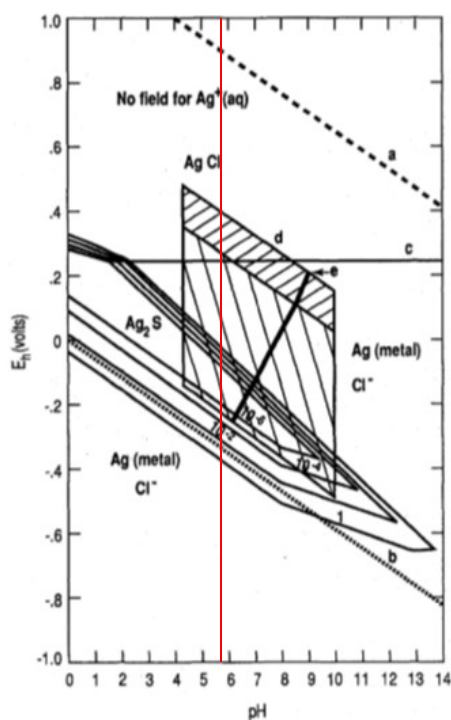


Figure 6.3: Stability diagram for silver in seawater at varying reduced sulfur concentrations p.355 [58]



### **6.1.2 Roman coin - Coin B**

Coin B was found in soil A and therefore, the burial environment as discussed above will heavily influence whether corrosion transpires and the type of corrosion products to form.

#### **6.1.2.1 Identification**

Coin B was identified as a Roman denarius minted between AD 138 to AD 161; Reece period 7. This coin was found near the Roman road, the Fosse Way, and the Roman town of Crococalana [41] adding further evidence of its Roman heritage. The obverse has a right facing bust of Antonius Pius present as well as an inscription of ONINVS which is the lettering remaining from the word ANTONINVS which is present on an Antonius Pius denarius. The reverse design confirms an Antonius Pius bust as the reverse design is that of Tranquillitas standing right holding a rudder and corn ears which is only present on Antonius Pius denarii. The inscription that can be made out on the reverse reads TR POT XV COS IIII. The coin weighs 2.5477g and has a diameter of 17.6mm or 18.0mm dependent on where the measurement was taken.



*Figure 6.4: OM image of the obverse of coin B, x50 magnification*



*Figure 6.5: OM image of the reverse of coin B, x50 magnification*

### 6.1.2.2 Results from XRF analysis

There were two main areas of visual difference that were studied by XRF with the averaged results below:

Element	Composition/ %	Error/ ± %
Ag	97.57	0.45
Pd	0.74	0.04
Pb	0.57	0.03
Cu	0.54	0.03
Fe	0.31	0.04
Bi	0.24	0.02
Au	0.03	0.02

*Table 6.4: Average XRF Elemental Composition of metal areas on coin B*

Element	Composition/ %	Error/ ± %
Ag	98.33	0.45
Pd	0.74	0.04
Pb	0.18	0.03
Cu	0.20	0.02
Fe	0.40	0.05
Bi	0.13	0.02
Au	0.01	0.01

*Table 6.5: Average XRF Elemental Composition of dark grey areas on coin B*

The major element present on the entirety of the surface is silver which is unsurprising seeing as the coin in question is a Roman denarius. The denarius was initially made of almost pure silver with a 95% to 98% silver content in 15 BC; over the next 270 years the silver content gradually declined to about 2% with later 3<sup>rd</sup> century AD coins consisting of copper with a silver external layer [59]. Both areas of the coin have an extremely high silver content of ~98% which could lead to the conclusion that this denarius is from the beginning of the first century, however the coin was identified as being from the 2<sup>nd</sup> century AD with the recorded values differing as the coins surface was subject to alteration. The area of dark grey; that possibly represents a common crystalline product in silver alteration such as AgCl, AgBr or Ag<sub>2</sub>S; has a slightly higher silver content of 98.33±0.45% compared to the metallic value of 97.57±0.45%. Although visually the two areas are slightly different, they contain exactly the same elements in very similar amounts. The difference between the silver content of the two areas is less than 1%, and this small difference is reflected throughout the other elements. From this data, at this point it is concluded that the surface and any corrosion on the surface is homogeneous even though visually a different conclusion is reached.

There is no inclusion of the major element silicon from soil A reported in the data for coin B as the coin matched an internal alloy standard in metals mode; there is an inclusion of Fe, Pd and Cu from the soil. The silver oxide layer that would have developed on coin B was porous and enabled the transportation of such elements to the surface of the metal. Consequently, the external corrosion products on coin B will have resulted from the reaction of the silver metal with the burial environment. It is possible that the Pd present in both tables with values of 0.74±0.04% in the metallic area and 0.74±0.04% in the dark grey area is due to Rayleigh scatter rather than soil inclusion. Lead could have been included in the original metallic composition or equally it could have been introduced during corrosion as Pb is a naturally occurring element reportedly found in soil. Bi and Au could be naturally

occurring in the burial environment and introduced into the surface, however they are not present in the XRF for the adhering soil sample. It is clear that the metal the coin was originally made from was certainly silver with some impurities existing from the smelting process and other elements being introduced during the lifetime of the coin whether this be before or during burial.

### **6.1.2.3 Visual Characterisation**

The preservation state for all coins in this study is relatively similar, they are covered in an alteration layer containing an external mineral stratum of soil and corrosion products influenced by the burial environment as well as initial oxide layers.



*Figure 6.6: Photograph of the obverse of coin B*



*Figure 6.4: OM image of the obverse of coin B, x50 magnification*

The obverse of coin B is partially covered in a dark grey/black crust of medium thickness with the remaining surface appearing as dull and metal like with some areas of lustre. The crust on the circumference and centre of the coin consists of small deposits of differing shapes with some areas built up as the deposits rest on one another. The metallic surfaces are relatively smooth however a fine corrosion layer is present creating a raised textural difference. The reverse of coin B (figure 6.5) demonstrates a similar appearance with key features such as the dark grey crust and areas of dull and lustrous metal identifiable. The reverse is not as corroded as the obverse and has a larger quantity of lustrous metal on its surface with some areas of the metal having a fine covering of dark grey/black specks.

The crust present could be the concretion of soil compounds, however with few or small amounts of common soil elements present in the XRF measurements the crust is probably that of silver corrosion products  $\text{AgCl}$  or  $\text{Ag}_2\text{S}$  which commonly form a black or grey crust. A hard greyish swollen crust (much like the crust on this coin) is formed when chloride ions in the burial environment permeate the initial protective surface layer of silver.

It is more than likely that the corrosion product AgBr has not formed as this usually has a brown crust; although the actual colours of exterior corrosion layers vary dependent on the soil compounds. The XRF reveals no inclination as to what the possible corrosion products could be as the presence of S, Cl and Br are not visible due to examination in metals mode, the results from the SEM-EDS and the XRD will confirm the identification of the corrosion.

#### 6.1.2.4 SEM-EDS results

All SEM images taken of this coin have a similar morphology which is that of a lumpy and raised powdery surface in general with the formation of two stratum. An initial lumpy powdery layer appears to have formed with an exterior raised surface equally with a globular powdery nature but appearing flattened.

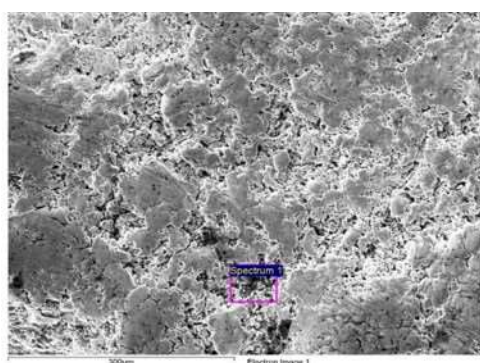


Figure 6.7: SEM image of area 3 on the reverse of coin B demonstrating site 1 of analysis

Element	Atomic percentage/ %
O	61.30
C	14.11
Cl	7.67
Ag	6.96
Si	6.86
Al	2.47
Fe	0.65

Table 6.6: SEM-EDS Elemental Composition of site 1 on area 3 of the reverse of coin B

Figure 6.7 demonstrates site 1 of analysis where the elemental analysis is taken from the powdery lumpy layer that appears to have formed initially. The analysis revealed that this was an oxygen rich layer, carbon was the next highest element, chlorine was 7.67% in abundance followed by silver, silicon, aluminium and iron. Silver is of a relatively low atomic percent (6.96%) similar to the chlorine and silicon in the sample. These results are in good agreement with the XRF data supporting that the coin is made from silver, but also highlights the introduction of soil elements Si, Al, Fe as well as Cl. As stated earlier, the carbon and oxygen may have some involvement with the corrosion products present but the high amount is possibly to do with interference from the atmosphere and sample preparation.

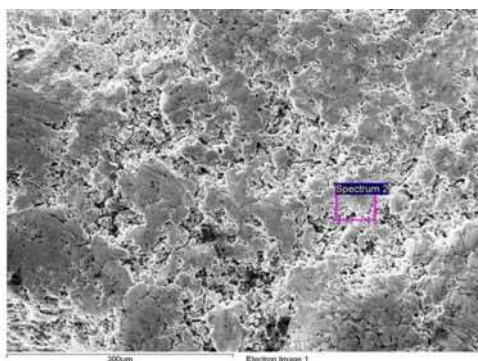


Figure 6.8: SEM image of area 3 on the reverse of coin B demonstrating site 2 of analysis

Element	Atomic percentage/ %
Cl	36.71
Ag	34.00
O	28.01
Si	1.28

Table 6.7: SEM-EDS Elemental Composition of site 2 on area 3 of the reverse of coin B

Site 2 of analysis on the same area is on the flatter smooth slab of powder that appears as an exterior layer. This raised area is the external layer that would have been in direct contact with the burial environment and has a high content of Cl - 36.71% (the element with the highest atomic percentage), leading to the assumption that AgCl has formed as a corrosion product. The amount of Si is also higher than the previous levels found in site 1, showing the influence of the Si present in the burial environment of this coin. Across all analyses performed on coin B the external layer has a high chlorine content (as well as other soil elements) and the initial layer has a lower silver and chlorine content but is oxygen rich. Thus demonstrating that an initial passive oxide layer upon contact with chlorine has transformed into a layer of AgCl with the inclusion of soil elements.

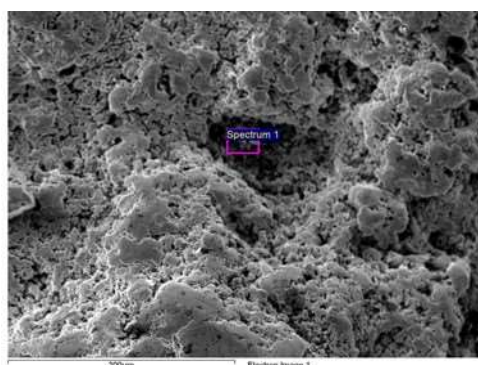


Figure 6.9: SEM image of area 2 on the reverse of coin B demonstrating site 1 of analysis

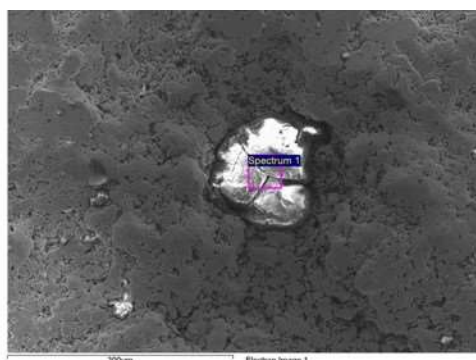
Element	Atomic percentage/ %
O	81.59
Cl	7.21
Ag	5.72
Si	5.48

Table 6.8: SEM-EDS Elemental Composition of site 1 on area 2 of the reverse of coin B

The area in figure 6.9 above demonstrates the two stratum with an increase of smaller powdery grains and several surface pits varying in depth. There is a relatively large and deep pit present with small powdery grains inside, the EDS analysis of this pit performed. As with site 1 on area 3 of the reverse of coin B the highest element of this pit was oxygen, followed by chlorine, silver and then silicon in similar percentages - meaning that the pit is similar to the initial corrosive layer, with the influence of elements from the soil evident



across the entire surface and not in localised corrosion pits. The soil has more of an influence on the exterior stratum confirmed by the inclusion of a large crystalline concretion shown in figure 6.10 where the rest of the surface shows the same powdery morphology as seen previously. The EDS analysis of a site locating the surface of this concretion only is as follows:



*Figure 6.10: SEM image of area 2 on the obverse of coin B demonstrating analysis of site 3*

Element	Atomic percentage/ %
O	69.07
Si	19.28
Al	6.60
K	5.06

*Table 6.9: SEM-EDS Elemental Composition of site 3 on area 2 of the obverse of coin B*

The amount of silicon in this site exceeds any other measured amount taken from the entirety of analyses on coin B. There is a high possibility that this lump is the concretion of quartz from the soil as the oxygen is in a high enough abundance for this to be possible supported by the major crystalline compound of the burial soil being quartz. There are other typical soil elements found alongside Si and O such as Al and K, the inclusion of these into the mineral stratum would be expected.

Overall, the layers seem physically discontinuous; however the major elements are similar across the entire surface leading to the conclusion that a general corrosive attack has taken place rather than any localised corrosion. There is a two stratum morphology with an initial oxygen rich layer and an exterior raised lumpy layer that tends to have a higher Cl content and a more corroded appearance. The dark grey crust seen visually is almost certainly AgCl rather than AgBr or Ag<sub>2</sub>S as Br and S are absent across the SEM-EDS analyses.

### 6.1.2.5 XRD results

The XRD data collected for the obverse of coin B demonstrated exactly the same reflections and compounds.

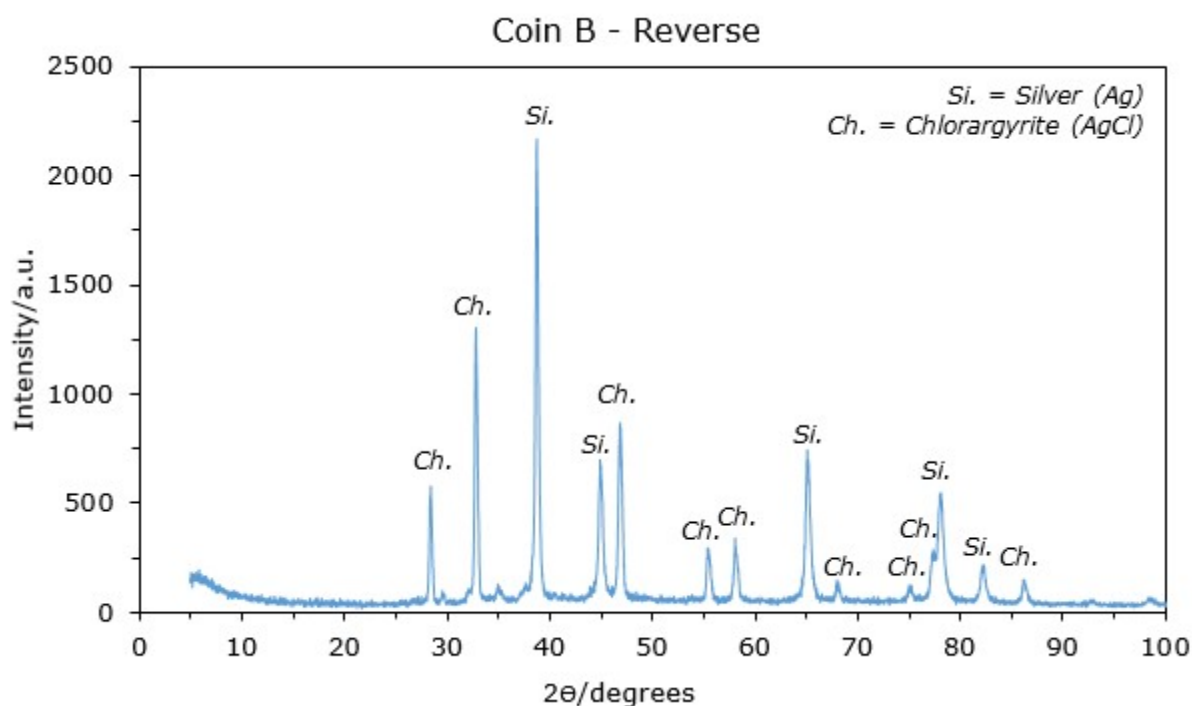


Figure 6.11: XRD pattern of the reverse of coin B

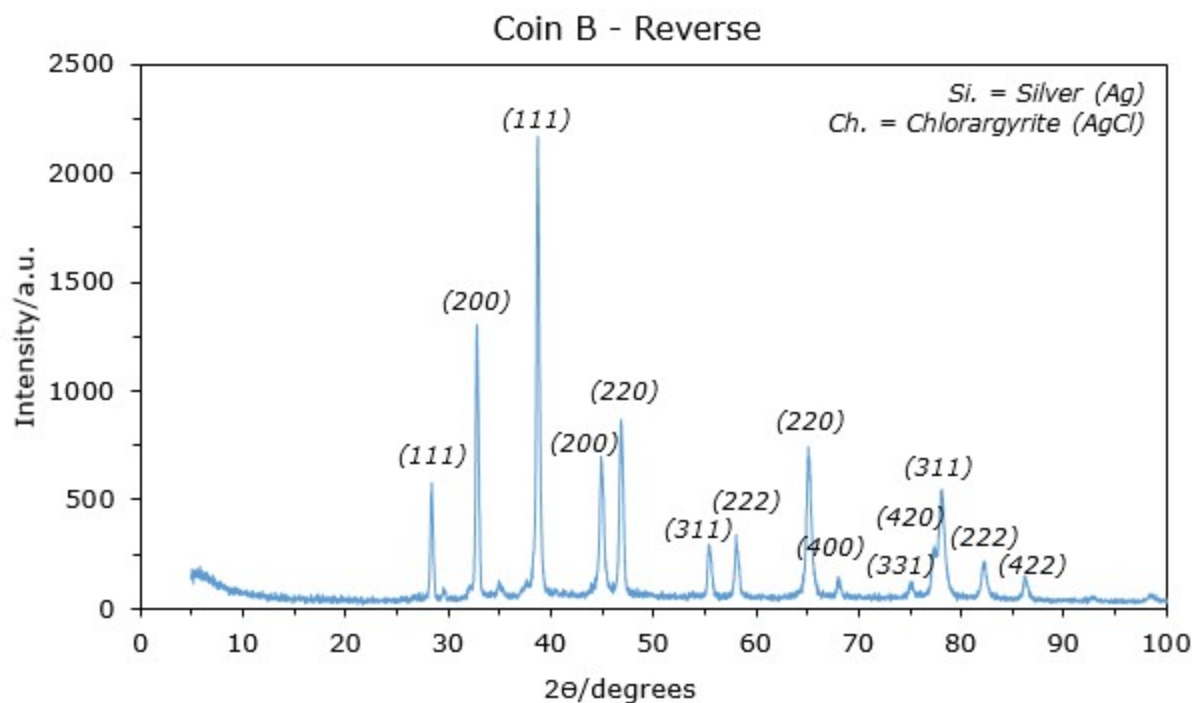


Figure 6.12: XRD pattern of the reverse of coin B showing lattice spacings

The XRD analysis revealed that the coins surface constituted of silver (Ag) and chlorargyrite (AgCl) with the d-spacing values matching the standard reference pattern of values as referenced in table 4.1. The figures above demonstrate on the same XRD pattern the

identification of the crystalline compounds (figure 6.11) as well as their lattice spacings (figure 6.12). The pattern for silver shown above matched the first four peaks of the literature values of silver with an additional peak at  $1.172\text{\AA}$  ( $82.24^\circ$ ) for the (222) face of silver thus rendering silver with a face-centered cubic crystal structure. Chlorargyrite shows peaks matching the entirety of the literature data pattern apart from a peak that should have a d-spacing of  $0.926\text{\AA}$  ( $112.72^\circ$ ) which will not be included in the range set for data analysis as the diffractometer scanned  $2\theta$  from  $5^\circ$  to  $100^\circ$  and  $112.72^\circ$  exceeds this value. Chlorargyrite also shows three additional peaks for the (222), (400) and (331) faces at  $58.15^\circ$  ( $1.586\text{\AA}$ ),  $68.06^\circ$  ( $1.378\text{\AA}$ ) and  $75.09^\circ$  ( $1.265\text{\AA}$ ) contributing to the cubic face-centered structure of AgCl. The XRD pattern shown below demonstrates synthesised Ag and AgCl nanoparticles scanned from  $20^\circ$  to  $80^\circ$  that includes the additional Ag(222), AgCl(222) and AgCl(400) peaks found in the data presented in this report.

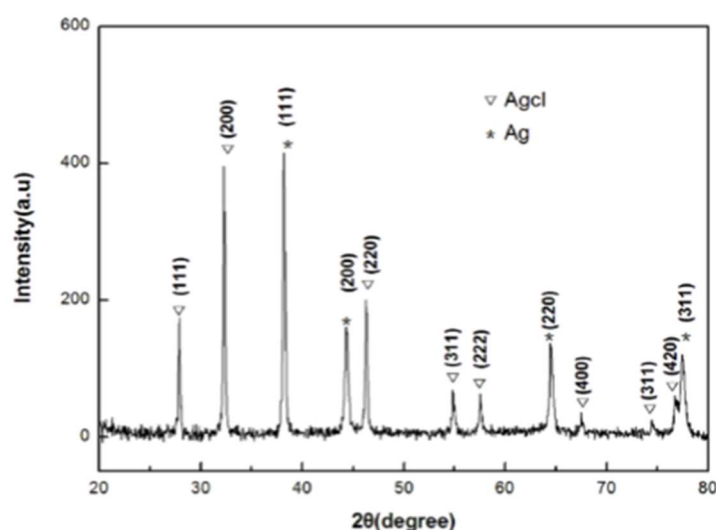


Figure 6.13: XRD pattern of Ag and AgCl nanoparticles [60]

### 6.1.3 Conclusion of the burial environment's influence on the corrosion products

The Roman denarius was made of silver with a dull lustrous metal layer representing the surface of the coin prior to corrosion. The morphology of the surface was that of a lumpy and raised powdery surface in general with the formation of two stratum. The initial layer appeared as a lumpy powder that had a high oxygen content as well as the presence of silver and chlorine. The exterior layer was raised in comparison and consisted of a globular powder that appeared flattened; this layer had an extremely high chlorine content followed by silver – an AgCl alteration product. The presence of chloroargyrite as a corrosion product was confirmed absolutely by the XRD analysis. The dark grey black crust of medium thickness visually present on the coin is this AgCl layer. The initial oxygen rich layer on the silver coin is the remainder of the initial oxide layer that formed to allow the diffusion of



elements such as Cl from the soil. Once these elements had diffused the oxide layer was then fully converted into AgCl. The pH of the environment influenced what was able to form under burial, and from the reserve acidity of soil A it was predicted that AgCl or Ag<sub>2</sub>S would form, potential dependent, as well as silver being stable. Only AgCl and Ag were found on the surface of the coin making it evident that the pH of the soil enabled these products to form and remain stable. The influence of the burial environment is apparent across the entire surface of the coin with certain elements diffusing into the surface from soil A such as Si, Fe, Al, Pd and Cu. There is no inclusion of Si in the XRF of coin B but quartz concretions are visible in the SEM images and confirmed by EDS analysis demonstrating once again the influence of the soils composition on the artefacts surface. The soil provided the chlorine for reaction with silver to produce AgCl as well as the correct environment not only to allow corrosion to proceed but for the products once formed to remain stable.

## 6.2 Silver Coinage corrosion

### 6.2.1 Identification

The Medieval coin - M516 was successfully identified as an Edward I penny with a class between 2 to 9c dating from 1279 – 1327 [61]. M516 was found in Thorpe Salvin, South Yorkshire close to the site of the ruins of the Medieval Thorpe Salvin Hall [62].



*Figure 6.14: OM image of the obverse of coin M516, x50 magnification*



*Figure 6.15: OM image of the reverse of coin M516, x50 magnification*

The obverse legend of an Edward I penny should read EDW RANGL DNS hYB; here the legend is seen as EDW RANG S hYB. The detail of the bust is clearly visible with a trifoliate crown rather than a bifoliate crown confirming an Edward I bust. The initial mark is present above the bust as well as the circles of pellets expected on a coin of this nature. The reverse of the coin has also kept the majority of its detail with the mint signature reading CI AS CAN TOR which should read CIVI TAS CAN TOR for a Canterbury mint surrounded by a circle of pellets. The reverse design of a solid long cross dividing the legend into quarters with trefoils in each quarter surrounded by an inner circle of pellets has also survived. The measurement of diameter for this particular coin was 17.95mm or 18.57mm position dependent and weighed 1.3389g. The diameter of this coin should be between 17 – 19mm; both of the measured diameters fit within this boundary so can be used as assistance for clarification but cannot be used for direct comparison as mentioned earlier [61].

### 6.2.2 XRF analysis results

Element	Composition/ %	Error/ ± %
Ag	96.75	0.35
Cu	1.12	0.03
Pd	0.75	0.03
Pb	0.61	0.03
Fe	0.56	0.05
Au	0.18	0.02
Ru	0.01	0.01
Zn	0	0

*Table 6.10: Average XRF Elemental Composition of cream areas on M516*

Element	Composition/ %	Error/ ± %
Ag	96.75	0.36
Fe	0.88	0.05
Cu	0.86	0.03
Pd	0.75	0.03
Pb	0.58	0.03
Au	0.17	0.02
Zn	0.01	0.01
Ru	0	0

*Table 6.11: Average XRF Elemental Composition of light grey/brown areas on M516*

The surface of the Edward I penny was mainly silver with both areas having the same composition of 96.75% with an accompanying error of  $\pm 0.35\%$  on the cream areas and  $\pm 0.36\%$  for the brown area; demonstrating a very generalised layer of silver across the sample. The copper content is slightly higher in the cream areas at  $1.12 \pm 0.03\%$  where in the light grey/brown areas the content was  $0.86 \pm 0.03\%$ , it is probable that this copper is part of the metallic alloy but equally could have been introduced from the burial environment. Palladium, lead and iron are found in similar amounts to each other and replicated in similar percentages across the entire coin; the areas of light grey/brown showing slightly higher amounts.

The main information to take from the XRF data is that the metal used to manufacture this coin was silver. There is an inclusion of minor elements Cu, Fe, Pd and Pb that were possibly introduced into the coin via diffusion from the burial environment. The Au, Zn and Ru are in trace amounts (with Zn and Ru not accounted for at some points) meaning that these elements are not considered to have any influence or effect on the corrosion of M516. The corrosion products present on the surface will be silver based but there is no further information to predict what the products will consist of. Copper containing compounds may have been formed although the copper is in such a small amount that it is more than likely contamination from the soil rather than part of the metal alloy.

### 6.2.3 Visual characterisation



Figure 6.16: Photograph of the obverse of M516



Figure 6.14: OM image of the obverse of coin M516, x50 magnification

The obverse of coin M516 is completely covered in a very fine smooth light grey/brown corrosion layer giving the coin an overall dull tone. There are some areas of lustrous metal localised on the embossed design. Areas of smooth sandy cream corrosion are present with a large amount in the centre of the bust. The cream corrosion looks to have formed as an initial layer to the light grey corrosion that appears grainy in these areas as seen under the OM.



Figure 6.15: OM image of the reverse of coin M516, x50 magnification

The reverse of coin M516 appears exactly as the obverse with a smooth light grey/brown dull corrosion layer overall but a lustrous surface on some of the embossed detail. There is a larger amount of the sandy cream corrosion product present formed as an initial layer with the dark grey grains appearing to have formed over the top.

As this coin is silver and shows similar colours to the alteration products on coin B it is possible that AgCl is present as a corrosion layer taking on a light grey/brown fine appearance. Chlorargyrite is the most common corrosion product to form on silver after the oxide layer has been successfully transformed into this product in a chlorine rich environment. If the burial environment includes sulfur or bromine AgBr or Ag<sub>2</sub>S may have formed; at this stage there is not enough information to disregard these products.

#### 6.2.4 SEM-EDS results

The SEM images of the sample revealed that the morphology was similar throughout having a raised surface with a globular bubble like appearance showing the formation of different layers as seen in coin B.

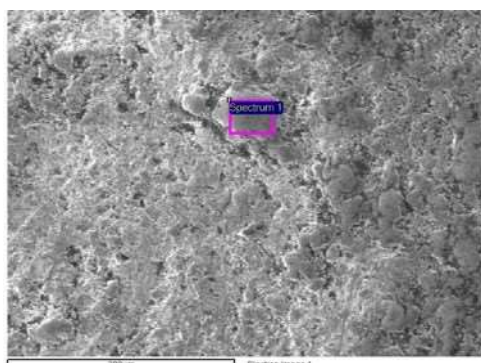


Figure 6.17: SEM image of area 1 on the obverse of M516 demonstrating site 1 of analysis

Element	Atomic percentage /%
C	34.26
O	27.24
Ag	17.75
Cl	17.42
Si	1.44
Br	1.18
Ca	0.49
Al	0.22

Table 6.12: SEM-EDS Elemental Composition of site 1 on area 1 of the obverse of M516

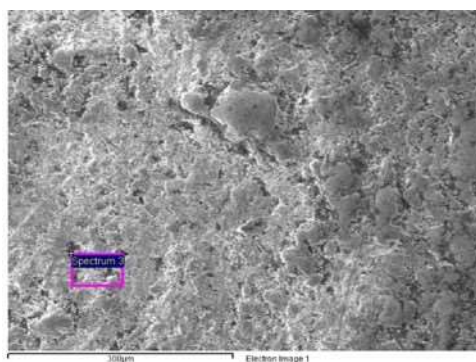


Figure 6.18: SEM image of area 1 on the obverse of M516 demonstrating site 3 of analysis

Element	Atomic percentage /%
O	56.00
Ag	16.95
C	13.65
Cl	7.05
Si	3.09
Al	2.58
Fe	0.68

Table 6.13: SEM-EDS Elemental Composition of site 3 on area 1 of the obverse of M516

The images above show area 1 of analysis and immediately it is apparent that the five most abundant elements on the surface are the same on both sites, the elements being O, C, Ag, Cl and Si; thus confirming that silver is the metal that coin M516 is composed of. The oxygen and carbon may well be part of the crystalline corrosion products present on the surface or could be from atmospheric contamination or sample preparation. Chlorine and silicon are present from the burial environment with these elements diffusing into the metal to influence the corrosion products. It is clear that the influence of elements from the soil is seen across the surface with similar elements replicated for a generalised layer.

Site 1 (figure 6.17) of a raised lump on the exterior surface that appears flattened and scratched has the highest atomic percentage of silver (17.75%) and chlorine (17.42%), which is the formation of AgCl. Bromine is present in this analysis, but in an amount similar to other elements from the soil as the ions diffused from the burial environment. If AgBr has formed as an alteration product it will be localised as Br is not present in other sites. This site is the exterior stratum consisting of a layer of corrosion as well as the heavy influence of the soil with the presence of calcium and aluminium amongst other common soil elements.

Site 3 (figure 6.18) demonstrates the two layered morphology with light grey grainy lumps broken by dark grey cracks and pits as an initial layer. This area is oxygen rich with the atomic percentage at 56.00% as part of the initial silver oxide layer to form before transformation into the external AgCl layer. The silver content here is similar to the external area of site 1 showing a general surface layer. The influence of elements from the soil is seen across the entire surface with a high atomic percentage of silicon and aluminium due to enhanced diffusion via surface cracks.

Area 3 of the reverse of the coin is similar to the obverse with a lumpy surface that has some raised areas as well as a small amount of pitting.

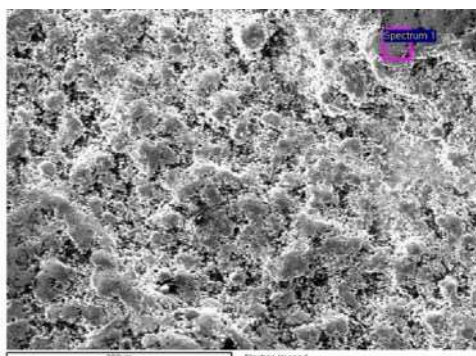


Figure 6.19: SEM image of area 3 on the reverse of M516 demonstrating site 1 of analysis

Element	Atomic percentage /%
C	36.03
O	30.94
Ag	15.38
Cl	14.52
Al	1.95
Si	1.17

Table 6.14: SEM-EDS Elemental Composition of site 1 on area 3 of the reverse of M516

Site 1, area 3 encompasses a flattened lump as an exterior layer with a smooth surface; similar to site 1 of area 1. The EDS analysis reported the elements in the following atomic percentages; carbon (36.03%), oxygen (30.94%), silver (15.38%), chlorine (14.52%), aluminium (1.95%) and silicon (1.17%). These results are similar to area 1 site 1 where silver and chlorine were in abundance in similar amounts representing the corrosion product AgCl on the exterior surface.



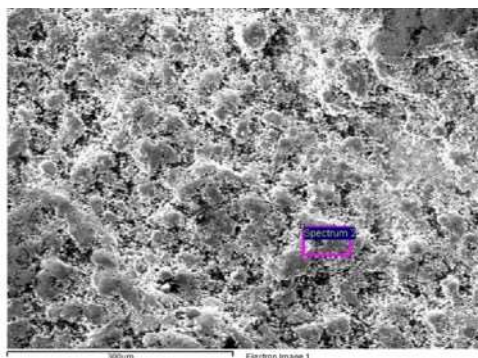


Figure 6.20: SEM image of area 3 on the reverse of M516 demonstrating site 2 of analysis

Element	Atomic percentage /%
O	48.04
C	19.19
Ag	14.14
Cl	12.23
Si	3.83
Al	2.15
Fe	0.43

Table 6.15: SEM-EDS Elemental Composition of site 2 on area 3 of the reverse of M516

Site 2 on area 3 encases a very lumpy area consisting of small and large spherical lumps as well as shallow surface pits. Again, the same elements are present here that appear throughout all analyses showing a generalised layer of corrosion. The silver and chlorine content are quite high possibly representing an external AgCl layer. Similar elements have diffused into the silver surface of the coin from the soil such as Si, Al and Fe.

Overall, the SEM-EDS analysis confirms that the metal the coin was manufactured from was silver. There is a high amount of oxygen and carbon across all the analyses, possibly from atmospheric contamination with the majority of oxygen from its inclusion in the initial oxide layer. Chlorine is present across all the analyses but is slightly higher in the exterior layer where the initial silver oxide has transformed into AgCl. Bromine is only present in one analysis and is quite low and so is a soil marker rather than part of a corrosion product such as AgBr. The burial environment has introduced the elements Si, Al, Fe and Ca into the metallic coin.

### 6.2.5 XRD results

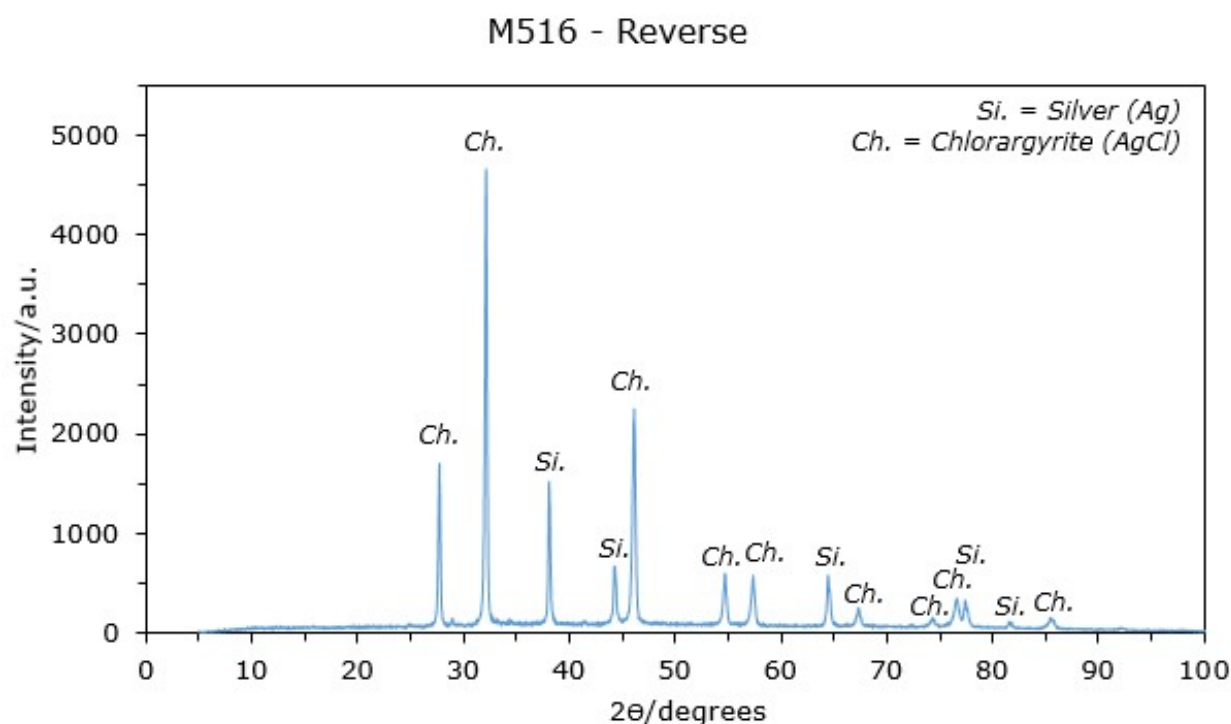


Figure 6.21: XRD pattern of the reverse of coin M516

The XRD patterns for the obverse and the reverse of sample M516 showed the exact same crystalline compounds which were silver (Ag) and Chlorargyrite (AgCl); the same corrosion products present on coin B. The pattern collected revealed the first four d-spacings of silver as found in the standard reference pattern of values as well as a peak at  $81.60^\circ$  ( $1.177 \text{ \AA}$ ) for the (222) face of silver. The entire pattern of silver above shows the (111), (200), (220), (311) and (222) planes of cubic face-centered silver; exactly the same as the XRD pattern of silver of coin B. The remaining 9 peaks are those of Chlorargyrite matching the entire literature data pattern for the d-spacings in the range of  $2\theta$  from  $5^\circ$  to  $100^\circ$  plus the three additional peaks for the (222), (400) and (331) planes showing a cubic face-centered structure of Chlorargyrite.

### 6.2.6 Conclusion

This Edward I penny was made of silver with the inclusion of common soil elements such as Cl, Al, Si, Cu, Fe, Pd and Pb. The morphology of this coin was very much the same as coin B demonstrating a raised powdery surface with the formation of different layers. The exterior surface was of a globular powder that almost appeared flattened with a high silver content followed by a high chlorine content and other soil elements such as Si, Br, Ca and Al. This exterior layer is the presence of the AgCl alteration product, as revealed by the XRD pattern of coin M516, as well as the incorporation of soil markers. A fine, smooth, light grey, brown corrosion layer with a dull tone is the visual appearance of this AgCl corrosion over the



entire coins surface. The initial lumpy, grainy powdery layer once again had a high oxygen content as well as the presence of Ag and Cl. The high oxygen content was once again due to an initial oxide layer that allowed the diffusion of elements from the soil and was then fully converted into AgCl; the remaining oxygen in abundance from this and from atmospheric contamination. All other silver coins studied were the same with respect to the corrosion products present, consisting of silver and chlorargyrite as well as hexagonal Ag<sub>2</sub>O in some cases (d-spacing value of  $\sim 2.797$ ). One of the silver coins studied M333, showed only silver and hexagonal Ag<sub>2</sub>O on its surface. Although compounds from the soil such as quartz are not found as crystalline corrosion products, their presence is apparent across the surfaces of these coins in elemental form and in the Cl provided to enable the formation of AgCl.

### 6.3 Silver alloy Coinage corrosion

The 'Modern' coin - V106 was identified as a silver-copper alloy and so was chosen for discussion of silver alloy corrosion.

#### 6.3.1 Identification

Coin V106 was successfully identified as a George V Sixpence from 1934. A George V Sixpence is reported to have a 19.00mm diameter and weigh 3.00g, this is close to the recorded measurements of coin V106 where the diameter was 19.36mm and the weight was 2.6179g. The weight and diameter will differ due to the fact that they have been exposed to a corrosive environment and therefore cannot be used for direct comparison to draw conclusions about identification.



Figure 6.22: OM image of the obverse of coin V106, x50 magnification



Figure 6.23: Image of the obverse of a George V Sixpence minted in 1934 [63]

Principally a large majority of the detail of this coin has survived, with the observable features highly visible to the eye. The inscription present on the obverse of a George V Sixpence is GEORGIVS V D.G. BRITT: OMN: REX F.D. IND: IMP: and the entirety of this inscription can be seen in figure 6.22 of coin V106 as well as the outline of the bust. The inscription present on the reverse of a George V Sixpence shown in figure 6.25 reads 'A· ·SIX PENCE· ·D·' ; on coin V106 the majority of this inscription can be seen apart from a few features that have been subject to corrosion. Some of the finer detail of the pattern has disappeared however an outline of the acorns and leaves remains with enough detail to successfully identify this coin as a George V Sixpence. [63]



Figure 6.24: OM image of the reverse of coin V106, x50 magnification



Figure 6.25: Image of the reverse of a George V Sixpence minted in 1934 [63]

### 6.3.2 XRF analysis results

Element	Composition/ %	Error/ ± %
Ag	72.45	0.29
Cu	23.20	0.13
Fe	1.75	0.06
Zn	1.39	0.03
Pd	0.66	0.03
Ni	0.43	0.03
Pb	0.07	0.02
Mn	0.04	0.03
As	0.00	0.01
Se	0	0
Ti	0	0
Sn	0	0
Ru	0	0

Table 6.16: Average XRF Elemental Composition of metal areas on V106

Element	Composition/ %	Error/ ± %
Ag	65.05	0.27
Cu	28.80	0.13
Fe	2.80	0.07
Zn	1.55	0.03
Ni	0.97	0.03
Pd	0.60	0.03
Ti	0.14	0.14
Pb	0.08	0.02
Sn	0.03	0.11
Ru	0.02	0.01
As	0.01	0.01
Mn	0	0
Se	0	0

Table 6.17: Average XRF Elemental Composition of green areas on V106

The elemental analysis of the George V Sixpence showed that the coin consisted of silver, copper, iron and zinc with all other elements present in minor or trace amounts. Elements lighter than sodium are left out of the data set and so any elements that would reveal what corrosion products were present, such as oxygen, are not recorded. The literature values reported for a George V Sixpence from 1934 state that the composition was 50% silver, 40% copper and 5% nickel [64]. Although the coin in its current preservation state will vary from these initial values, it confirms that V106 is supposed to be a silver-copper alloy.

Table 6.16 shows the elemental composition of the areas on V106 that appear to have a more natural metallic nature; in this area the silver content is at its highest at  $72.45 \pm 0.29\%$  with the copper content at  $23.20 \pm 0.13\%$ . The silver could be higher in this area due to the formation of a silver enriched surface layer as a result of galvanic corrosion in the alloy. In a silver-copper alloy the preferential corrosion of the more active copper takes place with the noble silver acting as a cathode and consequently forming an enriched layer. The presence of Fe and Zn in relatively high amounts as part of the four major elements on the surface could be from the metallic alloy. The remainder of the surface for the metallic area was made up of Pd, Ni, Pb, Mn, As and Se; the inclusion of these via diffusion from the soil.

Across all other analyses after the first four major elements the two minor elements Pd and Ni are present. The trace elements found are then Pb, Mn, As, Se, Ti, Sn and Ru varying in elemental composition with some elements absent from different areas. The green areas of the coin had an average of  $65.05 \pm 0.27\%$  for silver and  $28.80 \pm 0.13\%$  for copper, where the amount of silver is lower and the amount of copper is higher compared to the metallic area. This area may show more of a copper enriched surface due to the redeposition of copper onto the surface after preferential corrosion in the galvanic cell. It may be that this green looking corrosion is that of copper in the alloy and consequently its corrosion products.

### **6.3.3 Visual characterisation**

A fine patchy corrosion layer covers the unraised regions of the whole coin, and the embossed detail remains clearly visible. The corrosion has formed a very light layer and appears smooth to the naked eye, through the OM the corrosion products appear grainy and have formed in lumps.



*Figure 6.26: Photograph of the obverse of V106*



*Figure 6.22: OM image of the obverse of coin V106, x50 magnification*



The metal on the obverse appears untouched as a gold colour is present on the head and surrounding area; the metallic colour does however have a dull tone. There are relatively smooth patches of fine powdered dark brown and lumpier black corrosion with the brown corrosion framing the bust and the black corrosion on the outside of the nose (seen in figure 6.27). The detail of the edge is golden metallic in colour with some fine cream powder near the lettering (Figure 6.28). There are metallic scratches present on the head with the inclusion of a brown corrosion product in some.



*Figure 6.27: OM image of the black lumpy corrosion localised on the nose on the obverse of V106, x50 magnification*



*Figure 6.28: OM image of the cream corrosion near the lettering on the obverse of V106, x50 magnification*



*Figure 6.29: Photograph of the reverse of V106*



*Figure 6.24: OM image of the reverse of coin V106, x50 magnification*

In general the corrosion on the reverse is thicker and is dark green or black in colour; the metal and detailed pattern of the coin remain visible. There is a large amount of the greeny black raised corrosion product localised towards the bottom of the coin with the date on the coin almost worn away due to this alteration layer; there is a lot of the black grainy corrosion present in the centre and at the top near the letters PEN. The smooth brown powder as found on the obverse is present on the reverse with figure 6.30 demonstrating

this. The writing and the top of the central pattern is tarnished with an orangey/yellow colour, a creamy brown sand is present as an initial layer as seen in figure 6.31.



*Figure 6.30: OM image of the brown lumps present on the acorn on the reverse of V106, x100 magnification*



*Figure 6.31: OM image of the cream sandy corrosion product on the reverse of V106, x100 magnification*

At this stage, not much can be said for the visual identification of the corrosion products present on the surface. Due to the fact that this coin is a silver-copper alloy, both copper and silver corrosion products could be present dependent on whether a local action cell formed in the galvanic corrosion. Cuprite ( $\text{Cu}_2\text{O}$ ) has more than likely formed as the black or brown fine patina (rather than its common maroon colour) as cuprite is the most common corrosion product on a copper enriched layer during the galvanic corrosion of a silver-copper alloy. Dependent on the environment this oxide may have been converted into other secondary copper corrosion products. There are dark green tones present as fine layers on coin V106 so it is possible that copper carbonates or copper sulfates have formed as an even green or blue patina (rather than the uneven crusts commonly found for these and copper chlorides).

#### **6.3.4 SEM-EDS results**

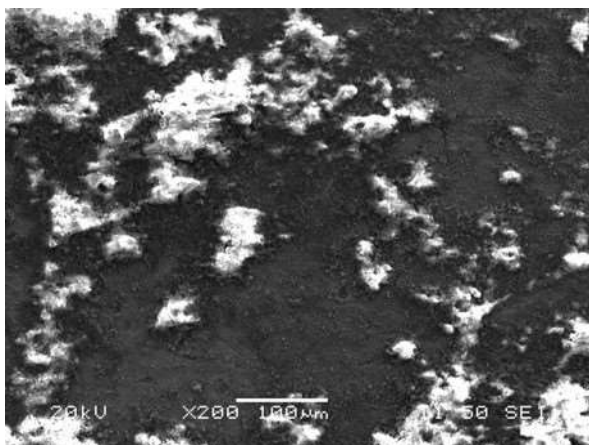


*Figure 6.32: SEM image of area 2 of the reverse of V106*

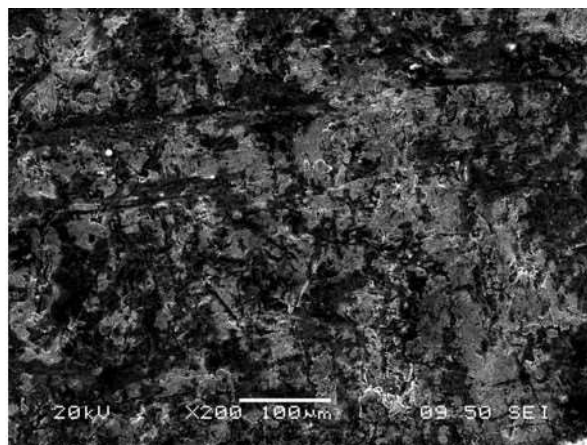


*Figure 6.33: SEM image of area 3 of the obverse of V106*

It is clear that the previous images of the silver-copper alloy are completely different to the other SEM images of the silver coins discussed where the surface showed a lumpy globular raised powder with the formation of different discontinuous layers. The surfaces for sample V106 do not demonstrate this type of morphology appearing rough with deposits of corrosion rather than a globular powder.

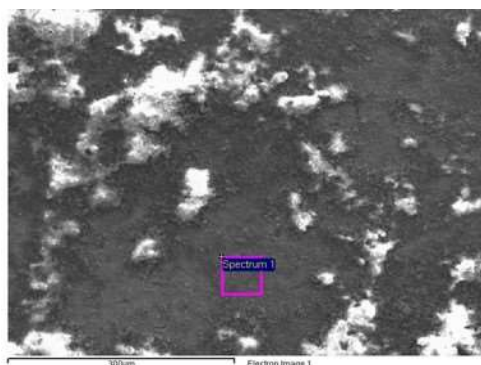


Figure 6.34: SEM image of area 2 on the reverse of V106 demonstrating site 1 of analysis

Element	Atomic percentage/ %
O	69.60
C	10.99
Ag	8.07
Cu	3.89
Fe	2.26
P	1.92
Si	1.65
Al	0.99
Ca	0.44
U	0.20

Table 6.18: SEM-EDS Elemental Composition of site 1 on area 2 of the reverse of V106

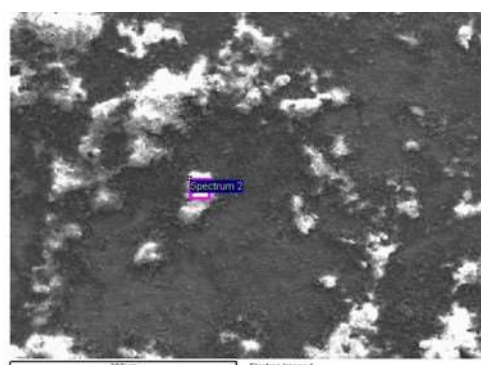


Figure 6.35: SEM image of area 2 on the reverse of V106 demonstrating site 2 of analysis

Element	Atomic percentage/ %
O	62.35
C	13.15
Si	12.43
Al	4.45
Cu	3.12
Fe	1.63
P	1.26
K	0.57
Mg	0.46
Ca	0.44
Ti	0.13

Table 6.19: SEM-EDS Elemental Composition of site 2 on area 2 of the reverse of V106

The surface here is a relatively even and smooth grainy powder with a random distribution of white crystalline lumps that have a smooth and mottled surface much like the surface of the quartz concretion on coin B. Site 1 of analysis on area 2 of the reverse is of the even grainy surface and demonstrates a high percentage of oxygen and copper; with the oxygen from the atmosphere if not from alteration products. The silver content of this site is 8.07% and is more metallic by nature due to its visibly smoother surface and the fact that Ag and Cu are the highest elements by atomic percent (disregarding C and O). There is an inclusion of soil elements on the surface such as Fe, P, Si, Al and Ca demonstrating the influence of the burial environment. These elements are also present in site 2 with the addition of K, Mg, Ca and Ti; elements commonly found in the soil. The presence of common soil elements in a much higher amount than site 1 and the absence of silver leads to the conclusion that these



white powdered collections are concretions of soil. There is a possibility that these concretions involve quartz as silicon and oxygen are present and the texture is much the same as the quartz concretions found on other samples.

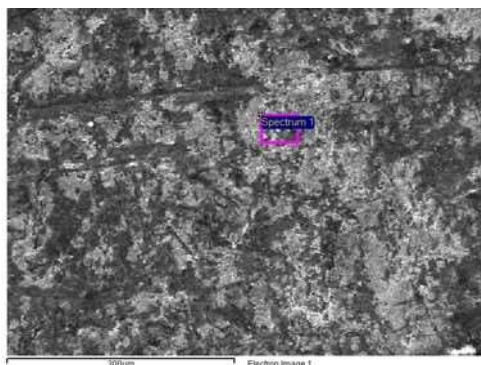


Figure 6.36: SEM image of area 3 of obverse of V106 demonstrating site 1 of analysis

Element	Atomic percentage/ %
O	68.01
Ag	13.17
C	8.22
Fe	2.85
Cu	2.80
P	1.84
Si	1.17
Ca	0.56
Zn	0.45
Al	0.34
Cl	0.31
U	0.28

Table 6.20: SEM-EDS Elemental Composition of site 1 on area 3 of the obverse of V106

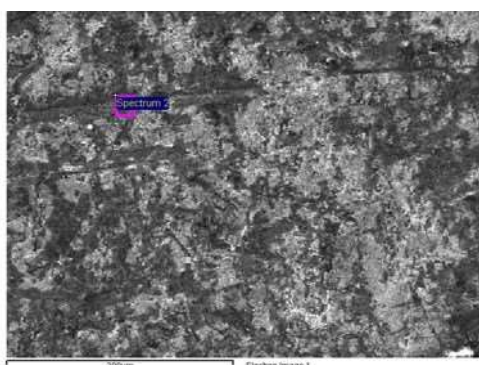


Figure 6.37: SEM image of area 3 of obverse of V106 demonstrating site 2 of analysis

Element	Atomic percentage/ %
O	68.87
C	11.29
Ag	6.49
Fe	3.29
Si	2.55
Cu	2.23
P	2.16
Al	1.19
Ca	0.62
Cl	0.42
Zn	0.42
Ni	0.27
U	0.21

Table 6.21: SEM-EDS Elemental Composition of site 2 on area 3 of the obverse of V106

Area 3 appears to have a general corrosion layer affecting the entire surface with the creation of a layered morphology. The external layer seems to have a smooth even surface with some holes and cracks forming, in the deeper cracks and shallow pitting the layer underneath has more of a grainy powdery appearance. The smooth external surface (figure 6.36) has a very high content of silver at 13.17% and a relatively large amount of copper at 2.23%. The content of iron is higher than copper which is not as expected from the XRF results where silver was followed by copper and then iron. There could be several reasons for this difference, one being the inclusion of iron from the soil, this area could have been subject to decuprification or it could be statistical fluctuation as the areas studied do differ. The inclusion of P, Si, Ca, Al, Cl are from the soil, the oxygen and carbon present may be



part of some corrosion product on the surface or from the atmosphere. Site 2, the analysis of the crack, shows a lower percentage of silver, copper and zinc; the base metal of the coin, and an increase in the amount of soil elements demonstrating the diffusion of these elements into the coin through cracks such as these.

From the SEM-EDS analysis a better idea is obtained about which elements have been introduced from the soil and therefore an estimate of the corrosion products present is formed. The alloy is certainly a silver-copper alloy and therefore any silver or copper corrosion products could be present. It is highly likely that quartz is present alongside cuprite with the possibility of other copper alteration products such as copper carbonates or copper silicates. As for the silver corrosion products, there is an absence of sulfur and bromine and only a small amount of chlorine present in some areas and so it is assumed that no silver corrosion has occurred.

### 6.3.5 XRD results

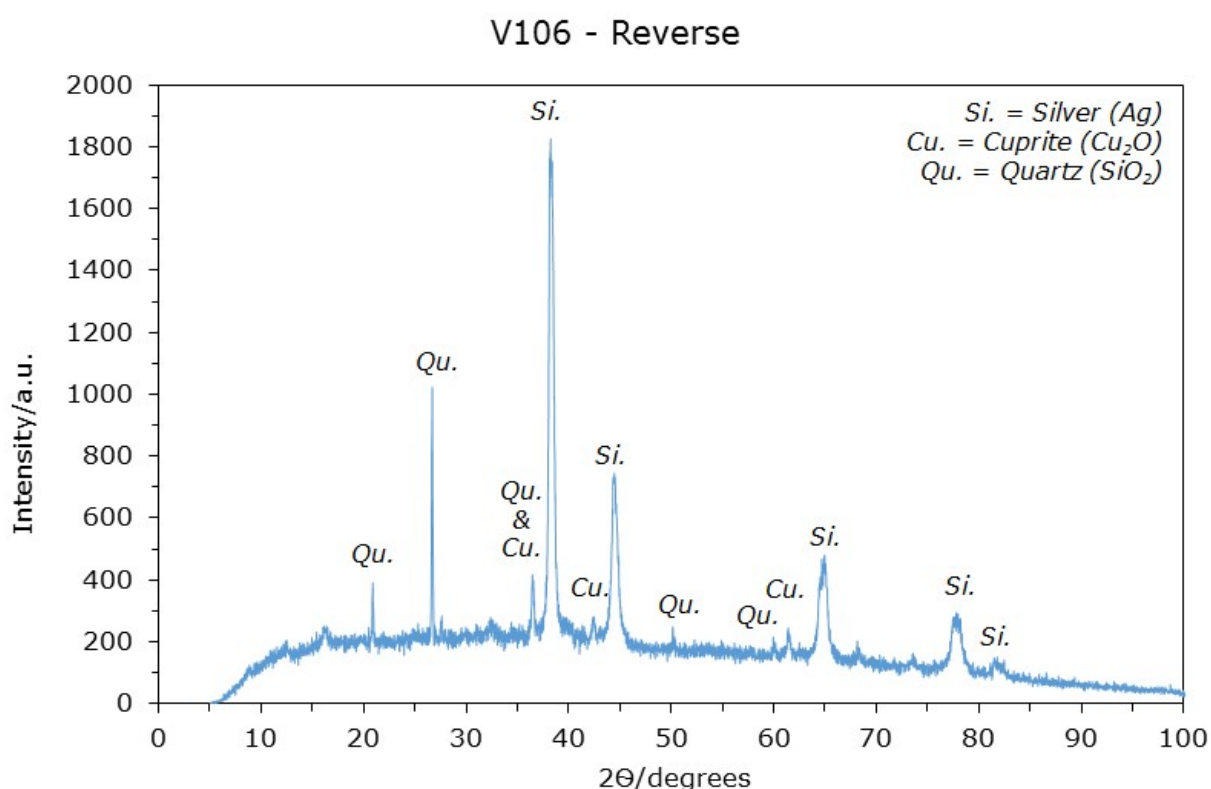


Figure 6.38: XRD pattern of the reverse of coin V106

Silver (Ag), quartz (SiO<sub>2</sub>) and cuprite (Cu<sub>2</sub>O) were all identified as crystalline compounds present on the surface of V106 due to the d-spacing values of these matching the standard reference pattern (table 4.1). The five peaks at 38.33°, 44.50°, 64.72°, 77.76° and 81.79° for the (111), (200), (220), (311) and (222) planes of cubic face-centered silver were present as in the XRD analyses for coin B and M516. The five peaks in order of intensity by

their d-spacing values at 3.33Å, 4.25Å, 1.82Å, 1.54Å and 2.46Å correlate to the first five peaks in the diffraction pattern of quartz. Finally, cuprite was identified with the first three peaks of its reference values appearing at 36.52°, 42.38° and 61.46° representing the planes (111), (200) and (220) of the cubic face-centered structure. The XRD pattern collected from the obverse of coin V106 showed exactly the same crystalline compounds.

The use of the initial results reported on the main elements in the alloy alongside the SEM-EDS analysis fully support the presence of crystalline silver, quartz and cuprite in the corrosion layer.

### **6.3.6 Conclusion**

The George V Sixpence from 1934 was that of a silver-copper alloy and consequently showed a different morphology and corrosion products to the other silver coins studied. The XRD of this coin showed that silver was present as the base metal and the corrosion products present were cuprite and quartz. There were two types of morphology present on the surface of this coin, the first was of a rough powdery surface with deposits of corrosion. The powdery surface was oxygen rich with a high content of silver and copper as well as the inclusion of elements from the soil such as Fe, P, Si, Al and Ca. The deposits present on this powdery surface contained a high amount of oxygen and silicon followed by a higher atomic percentage of Al, Fe and P from the soil; thus showing that the influence of the soils composition extended over the entire surface and the white deposits were concentrated inclusions of these elements. The second type of morphology showed a general smooth even corrosion layer affecting the entire surface with cracks and pitting. This type of morphology had a higher silver and copper content in comparison to the powdery surface as well as the presence of oxygen showing a more metal like surface. There was still a large amount of common soil elements across the surface with an increased amount in the cracks present as these increased diffusion. The corrosion here formed as a discontinuous general layer, the corrosion isn't by definition localised but nor is it present over the entire surface as shown in the two different morphologies. The surface does not visibly represent silver corrosion instead appears more like copper corrosion confirmed by the fact that the only corrosion product present on the surface is that of cuprite, a copper alteration product. The cuprite will have formed initially on this coin as the more active copper in the alloy preferentially corroded and redeposited onto the surface providing an enriched layer for cuprite formation. The quartz present on the surface of the coin would have diffused from the soil via the porous cuprite layer.

## 6.4 Summary of Silver Coinage Results

A summary of the corrosion products of all the silver coins studied in this project as well as the coins composition is found in the table below.

	Coin sample	Crystalline corrosion products identified			
		Coin Composition	Initial corrosion products	Exterior corrosion products	Soil compounds
Roman	Coin A	Ag		Chlorargyrite (AgCl)	
	Coin B	Ag		Chlorargyrite (AgCl)	
Medieval	M516	Ag		Chlorargyrite (AgCl)	
	M805	Ag	Hexagonal Silver Oxide (Ag <sub>2</sub> O)	Chlorargyrite (AgCl)	
	M804	Ag	Hexagonal Silver Oxide (Ag <sub>2</sub> O)	Chlorargyrite (AgCl)	
	M821	Ag	Hexagonal Silver Oxide (Ag <sub>2</sub> O)	Chlorargyrite (AgCl)	
	M333	Ag	Hexagonal Silver Oxide (Ag <sub>2</sub> O)		
Modern	V106	Ag-Cu	Cuprite (Cu <sub>2</sub> O)		Quartz (SiO <sub>2</sub> )

Table 6.22: Summary of composition and corrosion products of all silver coins in the study

Chlorargyrite was the major component of all but one of the silver coins studied. The addition of hexagonal Ag<sub>2</sub>O was found in a few cases, with one coin M333 having only hexagonal Ag<sub>2</sub>O on its surface and no Chlorargyrite. The exception to the presence of silver corrosion only on the surface was V106 which was a silver-copper alloy and demonstrated the copper corrosion product cuprite and quartz from the soil. The age of the silver coins does not make any difference towards the corrosion products expected, for a relatively pure silver coin the corrosion product to expect is always Chlorargyrite. The samples were all excavated from different areas within East Midlands and South Yorkshire and so different burial environments were present for each coin. The burial environment is a major factor to influence what corrosion products will form and it appears that in the case of M333 the burial environment in Holymoorside, Derbyshire did not support the formation of AgCl. Apart from this case and coin V106, the silver coins all had an alteration layer of Chlorargyrite.

The morphology of all the silver coins was found to be the same apart from the two earlier exceptions M333 and V106. This morphology was that of a general lumpy and raised

globular surface with the development of two stratum. The initial stratum was an oxygen rich lumpy powder and the exterior was a more flattened globular powder with a high chlorine content due to the presence of AgCl. The influence of elements such as Si and Al from the burial environment were seen across both stratum. Coin M333 had a very smooth general oxide layer and the presence of some surface cracks, it appeared more slab like rather than powder. The surface of M333 was high in oxygen and silver, Cl absent from the layer as the external layer of Chlorargyrite did not form. V106 saw the formation of copper corrosion products and so appeared similar to copper corrosion rather than silver corrosion. The corrosion did form generally across the surface as the compositions of the two different types of morphology were similar. The smooth and flat surface is that of an oxide, cuprite, and the rough powdery surface is once again oxygen rich, a general oxide layer. The white deposits present on the rough powdery surface have concentrated amounts of elements from the soil and so are concretions of compounds from the soil. The same distinct layered structure is present here as is on all silver coins, a metal core, an initial oxide layer with some soil markers and an external layer containing concretions of soil compounds and corrosion products directly influenced by the content of the burial environment.

All silver coins exhibit the major corrosion product Chlorargyrite, with one exception, therefore the age of the coin does not affect the corrosion products expected. The burial environment heavily influences what will form and remain stable, there were several differing locations of excavations and in general the same corrosion products were found; M333 again the exception to this rule. The environment that M333 was buried in for some reason did not support the formation of Chlorargyrite, demonstrating the huge impact the environment has on corrosion formation.

## Chapter 7 - MEIS analysis

A novel technique, in the field of corrosion studies on artefacts, Medium Energy Ion Scattering, was applied to one copper and one silver coin with the intention of attaining information about the structure and composition of the samples surface, as well as possible depth profiling, with the preliminary results discussed.

### 7.1 Copper coinage

A Victorian copper coin was analysed by MEIS with the intention of also gaining information about the depth of the oxide layer present. Coin V112 was very severely corroded and so it was almost impossible to identify; possible Victorian farthing due to being the correct size. As the excavation of this coin was from a field in Collingham where the majority of other finds and certainly the finds within this project are Victorian; it is possible to conclude that this coin is of Victorian heritage. Due to the severity of the corrosion and inclusion of soil, the surface was too thick to attain any information on the depth of the oxide layer. A chemical etching procedure was developed which initially stripped away the exterior soil stratum leaving the copper oxide layer whilst causing as little harm as possible to the base metal. A second stage of chemical etching aimed to remove any alteration layer to reveal the base metal. The alteration layer was still too thick to penetrate and so the surface was scraped after etching as the third stage.

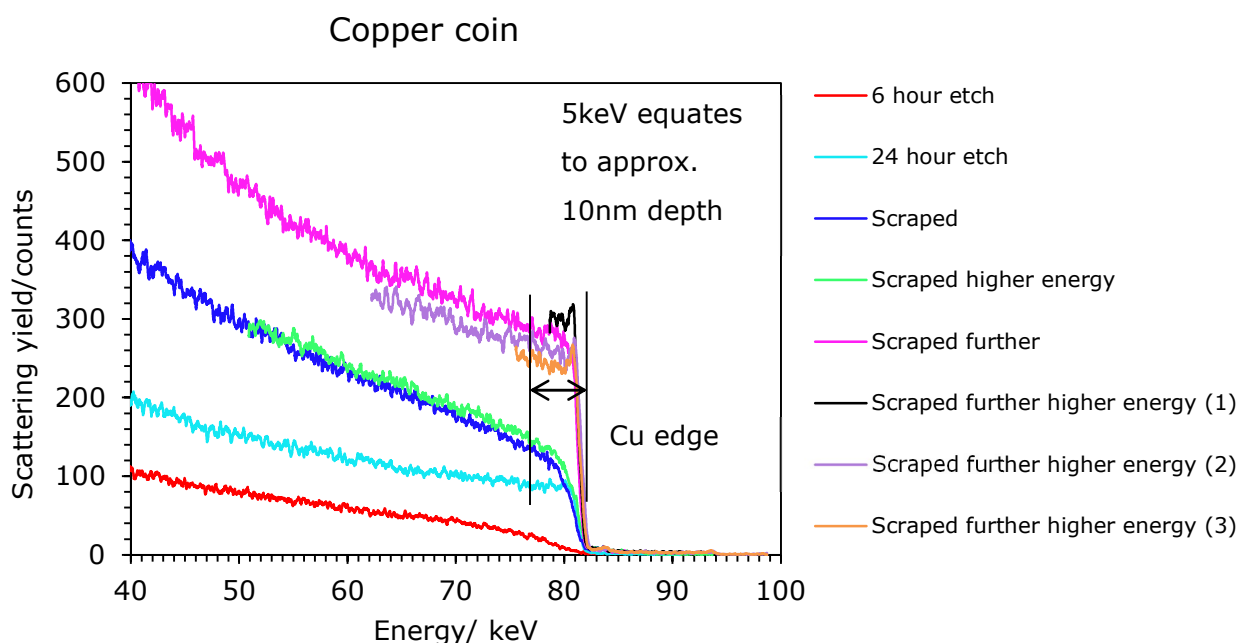


Figure 7.1: MEIS spectrum of coin V112

The first stage of chemical etching required leaving coin V112 in 10% acetic acid solution for 6 hours represented by the red line where the sample was analysed from 40keV to

83keV. The second stage of chemical etching saw the coin submerged for 24 hours in total represented by the light blue line (35.7keV to 90keV). The coin was lightly scraped at the top where the layer had been etched for 24 hours shown by the dark blue line (40keV to 83keV). This scraped area was analysed at a higher energy from 50.89keV to 93keV represented by the green line. The initial scraped area was then scraped further to reveal a shiny copper surface and analysed from 40.07keV to 85keV shown by the pink line. The further scraped area was analysed at higher energy masses with the black line representing 78.67keV to 92.67keV, the purple line from 62.23keV to 98.72keV and finally the orange line represents the analysis at 75.52keV to 98.72keV. A truer estimation of the base metal surface was revealed with the further removal of alteration layers, shown by the increasing sharpness of the copper edge at ~81.35keV (as expected from the literature calculations of where copper should be found on the graph, table 4.4, chapter 4). The only other elements expected at this energy from backscattering would be nickel at 80.03keV and zinc at 81.81keV. Copper was the best fit and as previous XRF measurements of this coin revealed that the majority of the surface was made up of copper ( $88.69 \pm 0.79\%$ ) as shown in the table below, the edge present on the MEIS graph is certainly copper.

Element	Composition/ %	Error/ $\pm$ %
Cu	88.69	0.79
Pb	6.08	0.63
Si	2.25	0.28
Fe	1.57	0.06
Al	0.92	1.20
As	0.31	0.03
Bi	0.06	0.03
Sn	0.05	0.06
Ag	0.05	0.01
Ni	0.03	0.02
Sb	0.01	0.02
Zr	0	0

*Table 7.1: Average XRF Elemental Composition of multi-coloured corrosion on V112*

The high energy part of the MEIS spectrum is shown below:

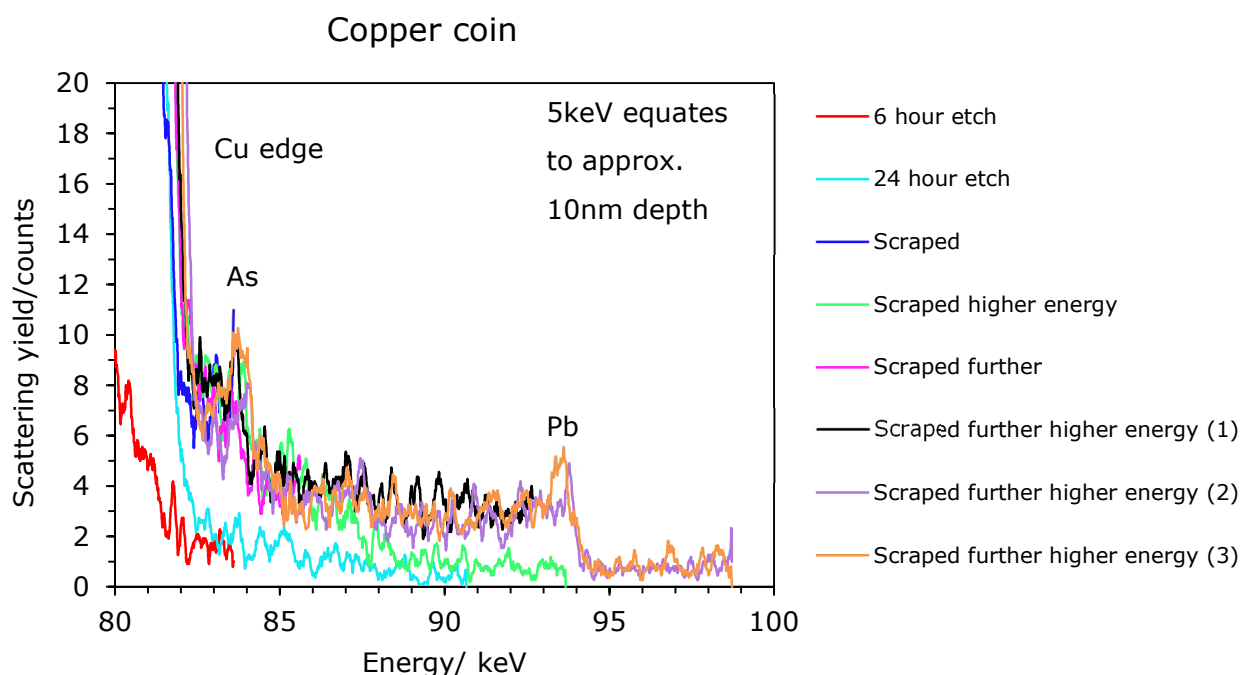


Figure 7.2: Higher energy part of the MEIS spectrum of coin V112

Focusing on the higher energy part of the spectrum revealed additional elements As and Pb at approximately 83keV and 93keV respectively. At 83keV Ge could have been identified as the energy of this should fall at 83.41keV, however As is present in the XRF spectrum of V112 and consequently labelled. At 93keV Bi could be present rather than Pb but as Pb is found in a higher amount on the surface in the XRF analysis the peak at 93keV was labelled as Pb.

Unfortunately, this MEIS pilot test did not provide any further information to that already attained via other analytical methods. The exterior stratum of V112 was too thick with the inclusion of soil minerals meaning that it was not possible to see the depth of the oxide layer. In order to see the surface composition the sample had to be chemically etched and scraped which caused harm to the object and so is not advised for the analysis of artefacts. The XRF results provided the elemental composition of the surface in a non-destructive manner and so is found to be the better technique for estimating the metal alloy.

## 7.2 Silver coinage

The medieval coin M804 was identified as an Edward I penny from 1279 – 1327. This particular sample could not undergo destructive analysis and so was not chemically etched in any way. The results for coin M804 from MEIS are displayed below:

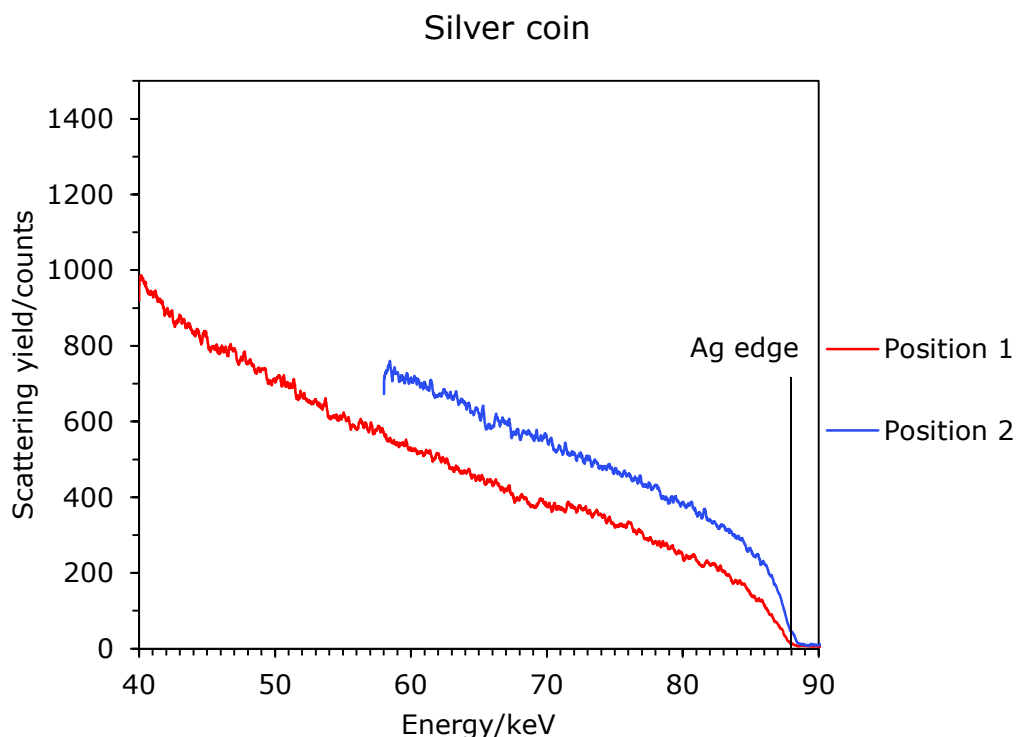


Figure 7.3: MEIS spectrum of coin M804

Initially the silver coin M804 was analysed from 40.29keV to 90keV shown by the red line, it was then moved to a height of 6mm and analysed from 58keV to 90keV demonstrated by the blue line. A silver edge is present at approximately 88keV as expected from the calculations of energies to be found in the MEIS spectrum in table 4.4. The other elements that would have signals at ~88keV are Pd and Cd but seeing as the XRF results shown in table 7.2 below of M804 demonstrate that the surface is made of a majority of silver it is clear that this peak in the spectrum is that of silver. No analysis was run at a higher energy as there would be nothing additional to the silver edge to be seen in the spectrum.

Element	Composition/ %	Error/ ± %
Ag	93.80	0.35
Cu	2.23	0.04
Pb	1.52	0.04
Fe	1.35	0.06
Pd	0.74	0.03
Au	0.33	0.03
Bi	0.03	0.011
Cd	0	0
Ru	0	0

Table 7.2: Average XRF Elemental Composition of metal areas on M804



Unfortunately the MEIS pilot again did not give any edge over the information already attained by the various analytical methods used on M804. The soil stratum was too thick to enable depth profiling and as this coin could not be subject to destructive analysis no further information could be gained over the results from XRF, XRD and SEM-EDS analysis as shown in appendix F.

### **7.3 Conclusion of MEIS studies**

MEIS analysis on the two samples provided compositional information; a copper edge and signals for As and Pb were identified at 81.35keV, 83keV and 93keV respectively for the copper coin and a silver edge was identified at 88keV for the silver coin. Unfortunately the information that was obtained was no more than that which could be obtained by traditional techniques. The alteration products on the coins including the soil stratum made the surface too thick to enable depth profiling of the corrosion layers. In order to reveal the surface composition of the copper coin chemical etching was employed to remove the alteration layer in stages, this caused harm to the object but in the least amount possible and so not advised for the preparation of artefacts in order to use MEIS as an analysis technique.

## Chapter 8 - Conclusion

The study of the corrosion layers on excavated copper and silver coins from varying periods was carried out so that the morphology and characterisation of these layers were understood in great detail. A combination of analytical techniques was pivotal in allowing a full and detailed account of the constituents of the artefacts providing information not only about the corrosion process but also for archaeological purposes. This data is extremely important for the archaeologist and the curator as the knowledge that certain elements or products are present, such as chlorine on the surface of copper or active corrosion products, gives an indication of future corrosion processes that may occur if stored incorrectly.

In this study, the present state of degradation for all coins was relatively similar; the samples were covered in an alteration layer containing an external mineral stratum - consisting of corrosion influenced by the burial environment as well as soil markers themselves, initial oxide layers with the metal core intact. The corrosion products identified, as well as the morphology, did not alter with the age of the coins with this and all results collated providing useful information for the future conservation and preservation of these types of metallic artefacts.

Key features of the coins were identified visually and with an OM to enable the historical information to be determined. The XRF measurements provided an estimate of the metallic alloy of the coins and the use of this in combination with the SEM-EDS measurements provided a clearer indication of the composition of the metal and various corrosion layers. The identification of the exact corrosion products was determined by XRD with the nature of the copper coins consisting mainly of copper, cuprite and quartz, with the inclusion of other compounds from the soil such as kaolinite found in coin D. Sample R02 exhibited secondary corrosion products in the form of the copper carbonate malachite. Even though the burial environment is a huge factor in influencing what may form and remain stable, it is the metal alloy and the majority components of this that will influence which metal oxide will form. Other coins in the study had differing metal oxides present dependent on the major components of the alloy. All silver coins studied had silver and Chlorargyrite as the major components of the surface, the addition of hexagonal  $\text{Ag}_2\text{O}$  was found in some cases presented in appendix F; M333 had silver and hexagonal  $\text{Ag}_2\text{O}$  only.

The production of oxides such as cuprite are not an issue for copper alloys, however the presence of atmospheric oxygen or atmospheric pollutants such as  $\text{SO}_2$  could be key for further active corrosion to take place in both copper and silver alloys. Therefore, the samples would be required to be kept in a de-oxygenated environment, a dehumidified

atmosphere, in order to preserve the coins and stop any other corrosion transpiring that may ultimately destroy the samples. Any storage facility would need to be checked to ensure the materials used were void of elements such as S or Cl and a dehumidified environment was obtained as corrosion is the spontaneous oxidation by atmospheric oxygen or atmospheric pollutants.

The major morphological features present on the surfaces were similar for both metals and their alloys identified by SEM-EDS. Uniform corrosion was observed across both metals with a general attack of the entire surface and no localised corrosion. The two metals exhibited slightly different textural features with the initial oxide layer of copper very smooth and flat followed by a secondary layer of grainy/smooth powder rich in common soil elements Si, P, Ca and Al; the initial oxygen rich layer of silver was a lumpy powder followed by an external flattened globular powder containing a high amount of Cl, Si and Al. Both metals had distinct similar layers observed, that of the metal core followed by the growth of an oxide layer with some additional elements in this stratum that had diffused from the soil into the surface via the initial porous oxide layer. The additional elements gradually lead to the formation of an external layer bearing soil markers such as quartz concretions as well as any secondary corrosion directly influenced by the content of the burial environment such as malachite and Chlorargyrite.

There was one sample that did not exhibit the same traits as the other coins studied and that was of a George V Sixpence (V106); a silver-copper alloy. The XRD of this coin showed silver as part of the base metal as well as a copper alteration product, cuprite and the presence of quartz. This sample highlighted two types of morphology one similar to the smooth and flat initial oxide layer of copper, identified as cuprite, with some surface cracks present that had increased the diffusion of common soil elements. The second type of morphology present was of a rough powdery oxygen rich surface including copper and silver as well as white deposits of concentrated amounts of elements from the soil - particularly silicon, possibly representing quartz. The corrosion did not form defined localised corrosion but more of a discontinuous general layer with different surface appearances but similar compositions. The surface appeared more like copper corrosion rather than silver corrosion due to the fact that the surface was covered by a copper alteration product. The sample followed the distinct layered structure common to both copper and silver; the metal core followed by an initial oxide layer containing elements from the soil with a final external layer containing soil sediments and elements (as well as any secondary corrosion products were they present).

The adhering soil samples studied had very similar properties, the two discussed were both loamy sands consisting mainly of Si in the form of quartz with high amounts of Fe, Al and

other common soil elements. Soil D the adhering sample to the copper coin, coin D, had a reserve acidity of  $6.51 \pm 0.0166$  meaning that the products expected to form as predicted by the Pourbaix diagram in figure 5.3 were copper, cuprite,  $\text{Cu}^+$  and  $\text{Cu}^{2+}$ ; the only products to form on coin D were copper and cuprite showing the influence the environment had on the formation and stability of corrosion products. Quartz and kaolinite were present across the exterior surface of this coin; elements such as Si, Fe and Al were found across both the initial and exterior stratum demonstrating the compositional influence of the soil on the copper coin. Soil A was taken from around the silver coin, coin B, and its reserve acidity was  $5.68 \pm 0.01$  with the expectant products of Chlorargyrite and silver sulfide as well as silver being stable. The only alteration products present on coin B were silver and Chlorargyrite once again demonstrating the influence of the burial environment upon the formation and stability of corrosion products. Elements such as Si and Al were found across the initial and exterior stratum as well as Cl showing the compositional influence of the soil, however no soil concretions were found on the surface of the silver coins the environment not altering the corrosion products present just influencing what will form.

Preliminary studies using MEIS to enhance corrosion studies on artefacts provided compositional information of the copper and silver samples identifying a copper edge at 81.35keV and the presence of As and Pb (in the higher energy part of the spectrum) for a chemically etched Victorian copper coin; a silver edge was identified at ~88keV for a silver medieval coin. The alteration products and inclusion of soil markers on the exterior layer meant that the surface was too thick to enable depth profiling of the layers and so no structural information was retrieved. Although compositional information was attained, there was nothing added than what could already be achieved by existing techniques regularly applied to corrosion studies of artefacts. The complexity of sample preparation and the limitations on sample size mean that MEIS is unlikely to be a significant technique in the study of artefacts, although it may play a part in the study of corrosion on metals more generally.

## **8.1 Future Work**

Although the majority of the coins were identified in this study, some of the samples had corrosion so severe that the identification of its type was an estimation based on the recorded location, the metallic alloy, the size of the coin and remaining worn details. Without key features of the artefacts visible, it becomes increasingly difficult to identify the objects to assist in dating historical events and for use as evidence of previous social and economic activity; an issue for the archaeologist and one identified in this project. Therefore, future work would include an attempt to solve this issue with the use of ion sputtering. Sputtering has previously been successfully implemented to visualise areas of

deformation on metal surfaces in order to reveal erased pictures on a modern 50 kopek coin. It works on the premise that atoms located on grain boundaries have smaller binding energies than those on crystallite sites and so are more easily sputtered. A new investigation of this process by molecular-dynamic simulation was performed by K.A. Tolpin and V.E. Yurasova [65]. Development of this present work with use of the results obtained by K.A. Tolpin et al. will allow the lost markings and patterns of coins to be revealed; detrimental information for archaeological interpretation.

Furthering the work completed on this project, the investigation of the soils' composition using SEM-EDS would be helpful in clarifying the differences between the metal and soils' composition in the corrosion layers of the coins. The XRF measurements of the soil samples provided the major components present in the loamy sands such as the element silicon. Elements such as Ca, Al and P that were identified as elements that had diffused from the soil into the samples studied were done so using information of 'common' soil elements as reported by R.Reale (2010) et al. [66], it would be of use to perform these tests in the future. The burial environment of the artefacts is extremely important in influencing the corrosion to transpire and if the products remain stable. This study revealed that the soil did influence which elements would diffuse into the metal coins and the corrosion products produced. It became clear that the corrosion products and morphology of the samples remained unaffected by the age of the samples; as only one type of soil was studied it would be helpful to attain different types of soil and to see if these had a different effect on the corrosion. Furthering this work on the burial environment would be to model artificially what has been happening in the soil in the last 50 years or so as some artefacts that were once safe are now being affected by changes in chemical processing, ploughing techniques and so on. This work is necessary to understand how best to preserve and conserve these artefacts or even to provide information for heritage management bodies such as Historic England in order to protect the remaining historical evidence underground. Pre modelling the expected changes in agriculture in the next 10 to 20 years would be highly useful to understand whether archaeological sites containing buried assemblages need to be rescued or are safe to remain in situ.

MEIS measurements conducted in this study didn't provide any more substance to what was already identified using other techniques. Artificially simulating corrosion in order to grow an oxide layer could be undertaken as described by Constantinides et al. (2001) [67] and investigated using MEIS to see the growth of the oxide layer at the metal-oxide interface. The thickness of the oxide layer at different stages in the artificial growth could be used to indicate the severity of the corrosion and ultimately assist in how best to preserve excavated coins.

# References

## References

1. M. Pollard, C. Batt, B. Stern, and S.M.M. Young, *Analytical Chemistry in Archaeology* Cambridge Manuals in Archaeology. 2007, Cambridge University Press: Cambridge, United Kingdom. p. 3.
2. O. Mircea, I. Sandu, I. Sarghie, and A.V. Sandu, *International Journal of Conservation Science*, 2010. **1**(1): 27-40.
3. G. Artioli, *Rendiconti Lincei* 2013. **24**(1): 55-62.
4. N.H. Tennent, *Conservation Science: A View From Four Perspectives*, in *The Interface Between Science and Conservation*, ed. S.Bradley, 1997, British Museum Press: London. p. 15 – 23.
5. S. Bradley, *Journal of the American Institute for Conservation*, 2005. **44**(3): 159-173.
6. S. Bradley, *The Impact of Conservation Science in the British Museum*, in *The Interface Between Science and Conservation*, ed. S.Bradley, 1997, British Museum Press: London. p. 1-7.
7. D. Thickett and L.R.Lee, *The British Museum Occasional Papers*, 2004. **No. 11**: 1-30.
8. J.Y. Akerman, *An Introduction to the Study of Ancient and Modern Coins*. 1848, J.R. Smith,London. p. 1 - 3 [Accessed:6 October 2014]
9. J.H. Kroll and N.M. Waggoner, *American Journal of Archaeology*, 1984. **88**(3): 325 - 340.
10. C. Howgego, *Approaching the Ancient World: Ancient History from Coins*. 1995 Routledge London and New York. p. 1-12
11. *The Royal Mint, UK coins: Coin designs and specifications*. 2014; Available from: <http://www.royalmint.com/discover/uk-coins/coin-design-and-specifications>. [Accessed: 8 October 2014]
12. A.A. Zahrani and M. Ghoniem, *International Journal of Conservation Science*, 2012. **3**(3): 143-152.
13. P.H. Rieger, *Electrochemistry*. 1987, Prentice-Hall Inc. : Englewood Cliffs, New Jersey, USA. p. 423 - 424.
14. M. McNeil and L.S. Selwyn, *Electrochemical Processes in Metallic Corrosion*, in *Handbook of Archaeological Sciences*, ed. D.R. Brothwell and A.M. PollardEditors, 2001, John Wiley & Sons, Ltd. : Chichester, West Sussex. p. 605 - 614.
15. Z. Ahmad, *Principles of Corrosion Engineering and Corrosion control*. 2006, Butterworth-Heinemann/ICHEME series: Oxford. p. 9 - 14, 520 - 521.
16. D.A. Jones, *Principles and Prevention of Corrosion*. Second ed. 1996, Prentice-Hall, Inc. : Upper Saddle River, New Jersey.
17. T.K. Ross, *Metal Corrosion*. Engineering Design Guides. 1977, Oxford University Press. p. 2.
18. S. Syed, *Emirates Journal for Engineering Research*, 2006. **11**(1): 1-24.
19. K.R. Trethewey and J. Chamberlain, *Corrosion for science and engineering*. Second ed. 1995, Longman Group Limited: Harlow, Essex p. 299-300.
20. R.F. Tylecote, *Journal of Archaeological Science*, 1979. **6**(4): 345-368.
21. V.S. Bagotsky, *Fundamentals of Electrochemistry*. Second ed. 2006, John Wiley & Sons Inc: Hoboken, New Jersey p. 380-383.
22. H.H. Uhlig and R.W. Revie, *Corrosion and Corrosion control: An Introduction to Corrosion Science and Engineering*. 3rd ed. 1985, John Wiley & Sons, Inc.: Chichester, New York.
23. L. Robbiola, J.-M. Blengino, and C. Fiaud, *Corrosion Science*, 1998. **40**(12): 2083-2111.
24. F. Noli, P. Misaelides, A. Hatzidimitriou, and M. Kokkoris, *Journal of Materials Chemistry*, 2003. **13**(1): 114-120.
25. C.M.B. Martins and J.I. Martins, *Protection of Metals and Physical Chemistry of Surfaces*, 2011. **47**(1): 128-132.

26. J. Wang, C. Xu, and G. Lv, *Applied Surface Science* 2006. **252**(18): 6294-6303.
27. E. Schindelholz and P.S. Storch, *A Simple Guide for Archaeological Materials Characterization*. 2001, Department of Anthropology, University of Minnesota: Minneapolis.
28. F. Clarelli, *Applied mathematical modelling*, 2014. **38**(19-20): 4804-4816.
29. A. Mezzi, C. Riccucci, T. de Caro, E. Angelini, F. Faraldi, S. Grassini, and V.K. Gouda, *Surface and Interface Analysis*, 2014. **46**(10-11): 801-806.
30. G.M. Ingo, S. Balbi, T.D. Caro, I. Fragala, E. Angelini, and G. Bultrini, *Applied Physics A*, 2006. **83**: 493 - 497.
31. G. Marchand, E. Guilminot, S. Lemoine, L. Rossetti, M. Vieau, and N. Stephant, *Heritage Science*, 2014. **2**(5).
32. Y. Wan, X. Wang, X. Wang, Y. Li, H. Sun, and K. Zhang, *International Journal of Electrochemical Science*, 2015. **10**: 2336 - 2354.
33. C. Liang, C. Yang, and N. Huang, *Surface and Interface Analysis*, 2011. **43**(4): 763-769.
34. *Grid Reference Finder*, 2008. Brough, Nottinghamshire. Available from: <http://www.gridreferencefinder.com>. [Accessed: 21 July 2015]
35. *Geology of Britain Viewer*. British Geological Survey materials © NERC, 2015. Available from: <http://mapapps.bgs.ac.uk/geologyofbritain/home.html>. [Accessed: 24 July 2015]
36. J. Gerrard, *Fundamentals of soils*. Routledge fundamentals of physical geography series. 2000, Routledge: London. p. 1, 13, 30, 36-39, 43, 190-192.
37. *Nottingham Climate*. Met Office. Available from: <http://www.metoffice.gov.uk/public/weather/climate/gcrjm8jf7>. [Accessed: 27 July 2015]
38. H.D. Foth, *Fundamentals of soil science*. 8th ed. 1980, Wiley: Chichester, New York. p. 12.
39. M. Bishop. *An Archaeological Resource Assessment of Roman Nottinghamshire*. East Midlands Archaeological Research Framework, 2001; Available from: [https://www.le.ac.uk/ulas/publications/documents/25nottrom\\_000.pdf](https://www.le.ac.uk/ulas/publications/documents/25nottrom_000.pdf). [Accessed: 30 July 2015]
40. M. Bennet. *An Archaeological Resource Assessment of the Roman Period in Lincolnshire*. East Midlands Archaeological Research Framework, 2001; Available from: [https://www.le.ac.uk/ulas/publications/documents/23linrom\\_000.pdf](https://www.le.ac.uk/ulas/publications/documents/23linrom_000.pdf). [Accessed: 30 July 2015]
41. *Magic Map, Ordnance Survey*, 2015. Brough, Nottinghamshire. Grid Ref: SK836585, Scale: 1:10000. Available from: <http://www.magic.gov.uk/MagicMap.aspx>. [Accessed: 21 July 2015]
42. *Google Earth V 7.1.5.1557*, 2015. Nottinghamshire. Available from: <http://www.google.com/earth/index.html>. [Accessed: 29 July 2015]
43. M. Bishop. *An Archaeological Resource Assessment of Medieval Nottinghamshire*. East Midlands Archaeological Research Framework, 2001; Available from: [https://www.le.ac.uk/ulas/publications/documents/35nottmed\\_000.pdf](https://www.le.ac.uk/ulas/publications/documents/35nottmed_000.pdf). [Accessed: 30 July 2015]
44. M. Bishop, V. Baddeley, and J. Mordan. *An Archaeological Resource Assessment of Post-Medieval Nottinghamshire (1500-1750)*. East Midlands Archaeological Research Framework, 2001; Available from: [https://www.le.ac.uk/ulas/publications/documents/40nottpmmed\\_000.pdf](https://www.le.ac.uk/ulas/publications/documents/40nottpmmed_000.pdf). [Accessed: 30 July 2015]
45. A.P. Nicholson. *Street map of Nottingham (c. 1960)*. Nottinghamshire History 2014; Available from: <http://www.nottshistory.org.uk/resources/maps/Nottingham/nottinghamstreetmapc1960.pdf>. [Accessed: 30 July 2015]
46. U. Spence and M. Bishop. *An Archaeological Resource Assessment of Modern Nottinghamshire (1750 onwards)*. East Midlands Archaeological Research Framework, 2001; Available from: [https://www.le.ac.uk/ulas/publications/documents/45nottmod\\_000.pdf](https://www.le.ac.uk/ulas/publications/documents/45nottmod_000.pdf). [Accessed: 30 July 2015]

47. *Google Earth V 7.1.5.1557, 2015. East Midlands and South Yorkshire.* Available from: <http://www.google.com/earth/index.html>. [Accessed: 29 July 2015]
48. *Handbook of Mineralogy*, ed. J.W. Anthony, R.A. Bideaux, K.W. Bladh, and M.C. Nichols. Mineralogical Society of America: Chantilly, VA 20151-1110, USA.
49. *X-Ray Data Booklet*. 07.01.2015; Available from: [http://xdb.lbl.gov/Section1/Table\\_1-2.pdf](http://xdb.lbl.gov/Section1/Table_1-2.pdf). [Accessed: 07.01.2015]
50. *Handheld XRF for Art and Archaeology*. Studies in Archaeological Sciences 3, ed. A.N. Shugar and J.L. Mass. 2012, Leuven University Press: Leuven. p. 1-35.
51. *Munsell Soil Color Charts*. 2000 Revised Washable Edition ed. 2000, Gretag Macbeth: New Windsor, New York.
52. *Field Recording Manual* 2007, National Museums Liverpool, Museum of Liverpool, Field Archaeology Unit, Version 2.0a.
53. B. Minasny, A.B. McBratney, D.M. Brough, and D. Jacquier, *European Journal of Soil Science*, 2011. **62**(5): 728 – 732.
54. *Coin Database - 1861 Farthing* Available from: [http://www.coindatabase.com/coin\\_detail\\_libras.php?cdb=K040302](http://www.coindatabase.com/coin_detail_libras.php?cdb=K040302). [Accessed: 11 August 2015]
55. C. Flament and P. Marchetti, *Nuclear Instruments and Methods in Physics Research Section B: Beam Interactions with Materials and Atoms*, 2004. **226**(1-2): 179-184.
56. S. Moorhead, *A History of Roman Coinage in Britain* ed. G. Payne. 2013, Greenlight Publishing Essex, Great Britain p. 10, 25.
57. B. McMullen. *SOILpak for vegetable growers*. 2000; Available from: [http://www.dpi.nsw.gov.au/\\_data/assets/pdf\\_file/0018/127215/Features-of-soil.pdf](http://www.dpi.nsw.gov.au/_data/assets/pdf_file/0018/127215/Features-of-soil.pdf). [Accessed: 30 September 2015]
58. M.B. McNeil and B.J. Little, *Journal of the American Institute for Conservation* 1992. **31**(3): 355 - 366.
59. A.W. Pense, *Materials Characterization*, 1992. **29**(2): 213 - 222.
60. X. Zhao, J. Zhang, B. Wang, A. Zada, and M. Humayun, *Materials* 2015. **8**(5): 2043 - 2053.
61. C. Savage, *Introduction to medieval coins & identification guide for archaeologists*, Guide 37, in BAJR Practical Guide Series. 2014.
62. *Magic Map, Ordnance Survey, 2015. Thorpe Salvin, South Yorkshire. Grid Ref: SK521812, Scale: 1:2500.* Available from: <http://www.magic.gov.uk/MagicMap.aspx>. [Accessed: 31 July 2015]
63. *London Coins*. Available from: [http://www.londoncoins.co.uk/?page=retailv2\\_details&uin=0012211](http://www.londoncoins.co.uk/?page=retailv2_details&uin=0012211). [Accessed: 14 January 2015]
64. *Coin Database - George V Sixpence 1934*. Available from: [http://www.coindatabase.com/coin\\_detail\\_libras.php?cdb=M110308](http://www.coindatabase.com/coin_detail_libras.php?cdb=M110308). [Accessed: 14 January 2015]
65. K.A. Tolpin and V.E. Yurasova, *Vacuum*, 2014. **105**: 74-79.
66. R. Reale, S.H. Plattner, G. Guida, M.P. Sammartino, and G. Visco, *Chemistry Central Journal* 2010. **6** (2).
67. I. Constantinides, A. Adriaens, and F. Adams, *Applied Surface Science*, 2002. **189**: 90 - 101
68. *Powder Diffraction: Theory and Practice*, ed. R.E. Dinnebier, S.J.L. Billinge, and A.L. Bail. 2008, The Royal Society of Chemistry: Cambridge. p. 1 - 6
69. *Handbook of X-Ray Spectrometry*. Second Edition ed. Practical Spectroscopy Series, ed. R.V. Grieken and A. Markowicz. 2001, CRC Press. p. 7-8
70. P.J. Goodhew, J. Humphreys, and R. Beanland, *Electron Microscopy and Analysis* Third Edition ed. 2001, Taylor & Francis: London.
71. M.W. Davidson and M. Abramowitz. *Optical Microscopy*. Microscopy Resource Center, 1999; Available from: <http://www.olympusmicro.com/primer/microscopy.pdf>. [Accessed: 29.05.2015]
72. T. Noakes, *Medium Energy Ion Scattering*, in 4th Annual Accelerator Symposium 03.03.15: University of Huddersfield



73. R. Barlow, P. Bailey, and J.A. vandenBerg. The UK MEIS facility: A new future. in Proceedings of the Third International Particle Accelerator Conference IPAC2012. 2012. New Orleans, Louisiana, USA
74. W.K. Chu, *Backscattering Spectrometry*. 1978, Academic Press, Inc.: London p. 22-23.
75. CAICISS. *Kinematic factor derivation* Available from: <http://www.caiciss.co.uk/kinematic.pdf>. [Accessed: 01.06.2015]

# Appendices

## Appendices' Contents

Appendix A - Principles of techniques .....	123
A.1 X-ray Diffraction .....	123
A.2 X-ray Fluorescence .....	124
A.3 SEM-EDS .....	124
A.4 Optical Microscopy .....	124
A.5 MEIS .....	125
 Appendix B – Derivation of the Kinematic factor .....	 127
 Appendix C – Averaging and error equations.....	 130
 Appendix D – Raw soil sample data, average and error calculations .....	 131
D.1 Raw soil sample data, average and error for pH tests.....	131
D.2 Raw XRF data for soil A .....	131
D.3 Raw XRF data for soil C .....	132
D.4 Raw XRF data for soil D .....	132
 Appendix E – Raw XRF data, average and error calculations.....	 133
E.1 Raw XRF data and average data for R06 .....	133
E.2 Raw XRF data and average data for R02 .....	134
E.3 Raw XRF data and average data for R294 .....	137
E.4 Raw XRF data and average data for R253B.....	139
E.5 Raw XRF data and average data for R03 .....	140
E.6 Raw XRF data and average data for V186 .....	142
E.7 Raw XRF data and average data for V112 .....	143
E.8 Raw XRF data and average data for V114 .....	145
E.9 Raw XRF data and average data for Coin C.....	147
E.10 Raw XRF data and average data for Coin D .....	148
E.11 Raw XRF data and average data for Coin A.....	150
E.12 Raw XRF data and average data for Coin B.....	151
E.13 Raw XRF data and average data for M516 .....	152
E.14 Raw XRF data and average data for M805 .....	153
E.15 Raw XRF data and average data for M804 .....	154
E.16 Raw XRF data and average data for M821 .....	156
E.17 Raw XRF data and average data for M333 .....	157
E.18 Raw XRF data and average data for V106.....	158

Appendix F – Results pages .....	160
F.1 Results for R294 .....	160
F.2 Results for R253B .....	161
F.3 Results for R03 .....	162
F.4 Results for V186 .....	163
F.5 Results for V112 .....	164
F.6 Results for V114 .....	165
F.7 Results for Burial environment C .....	166
F.8 Results for Coin C.....	167
F.9 Results for Coin A.....	168
F.10 Results for M805 .....	169
F.11 Results for M804 .....	170
F.12 Results for M821 .....	171
F.13 Results for M333 .....	172

## Appendix A - Principles of techniques

### A.1 X-ray Diffraction

Compounds and minerals have crystallographic structures that are completely unique, allowing them to be identified precisely by X-ray diffraction (XRD) through comparison of their diffraction data to a database of known compounds and minerals. In cultural heritage XRD is therefore the ultimate tool for revealing the crystalline corrosion products present in a corrosion layer [3].

The interatomic distances in most crystalline solids fall in the angstrom range, as X-rays have wavelengths with a typical order of  $1\text{\AA}$ ; they can be diffracted from repeating atomic patterns characteristic of crystalline solids. In XRD, X-rays are scattered from core electrons in atoms with the intensity of these scattered X-rays measured. Atoms at different positions scatter waves so that they arrive at the detector with a relative phase shift, meaning that the measured intensities in the diffraction pattern correlates to the atoms and their positions, providing structural information [68].

XRD can be described by the Bragg equation in terms of X-rays reflected by lattice planes, where lattice planes are characterised by the Miller Indices  $hkl$ . The layers of atoms are treated as parallel reflecting planes, with a monochromatic X-ray beam on these planes producing a diffraction set. The scattered waves must stay in phase to produce constructive interference for the intensity to be at the maximum where  $n$  is an integer. If destructive interference is produced, the waves are out of phase meaning that no peaks will be visible as  $n$  is no longer an integer. Each reflection occurs at an angle  $2\theta$  which corresponds to the separation of the planes of atoms in the sample being analysed. The measured angles of diffraction ( $2\theta$ ) are used to calculate d-spacing values ( $d$ ) according to Bragg's law:

$$n\lambda = 2d\sin\theta \quad (A1)$$

$n$  = order of diffracted beam

$\lambda$  = wavelength of the incident beam

$\theta$  = angle of diffracted wave

$d$  = lattice spacing

[68]

Once the  $d$  spacing is calculated the mineral or compound can be identified through comparison to standard reference materials. The technique itself is non-destructive if the sample can fit directly into a sample holder and into the XRD machine, for larger items of cultural heritage the corrosion layer would require scraping to produce a powder for analysis rendering the technique as destructive.

## **A.2 X-ray Fluorescence**

X-ray Fluorescence (XRF) provides an instant elemental description of the surface of an object. The XRF technique is growing so rapidly in popularity that in publications analysing items of cultural heritage it is often used as the main analytical technique [50].

In XRF a sample is exposed to short wavelength X-rays which ionizes the core electrons allowing their transition from atomic shells; thus creating an energy difference. A vacancy produced by an ejected electron from the K shell filled by an electron from a higher energy level, the L level is accompanied by the emission of secondary X-rays in the form of a K $\alpha$  X-ray line. This process continues with vacancies created in other shells being filled by electrons from different higher energy levels giving rise to K $\beta$  lines, L $\alpha$  lines, L $\beta$  lines and so on [69]. The secondary X-rays are collected in a detector that gives rise to signals with varying amplitudes dependent on the atomic number of the collided atom. The energy of these signals are compared to characteristic X-rays of elements to identify the presence of a particular element [55]. The intensity of the radiation is directly related to the amount of the element in the sample, so with calibration most elements with  $Z > 8$  can be determined quantitatively.

## **A.3 SEM-EDS**

The semi-quantitative chemical elemental distribution was studied by Scanning Electron Microscopy in combination with Energy Dispersive X-ray Spectroscopy (SEM-EDS) in order to understand the composition and morphology of corrosion products present on the samples surface. The SEM employs a beam of electrons for imaging that are directed and focused at the sample by electric and magnetic fields whilst moving over the samples surface from point to point. Back scattered and secondary electrons emitted by the surface have associated energies characteristic to the shape and crystal orientation of the sample, these are imaged by the detector giving rise to a micrograph. As well as scattered and secondary electrons, other forms of radiation such as X-rays can be reflected from the surface which are used with energy dispersive spectroscopy (EDS) to quantify the elemental composition of the sample [70].

## **A.4 Optical Microscopy**

An optical microscope is a microscope that makes use of visible light to produce a micrograph of the sample of interest. The microscope uses a conventional lens system to magnify an image in order to investigate the surface morphology of a sample and to characterise the morphological features present [71].

## A.5 MEIS

Medium Energy Ion Scattering (MEIS) is a very powerful tool used across a broad range of fundamental and applied studies to probe the surface and near surface of materials [72]. MEIS is in essence a low energy enhancement of Rutherford backscattering/channelling and is capable of giving compositional and structural information as a function of depth with much higher depth resolution (in the nm range). A H or He beam is used to probe the surface structure of materials, with the mass of the nucleus that the initial beam particles collide with directly correlating to the energy of the scattered ion. Energy loss occurs in two forms during scattering; elastic and inelastic. Elastic energy loss occurs in the hard collision of the ion with a target atom and from the energy analysis of the backscattered ion the mass of the target atom can be calculated which leads to compositional analysis. In this elastic collision, a transfer of energy takes place from the moving particle to the target atom. The consequent energy loss of the ion depends on the mass ratio of the incident ion/target atom and the scattering angle. By application of the principles of conservation of energy and momentum, the kinematic factor can be calculated and consequently the energy of the target atom. The derived equation used for calculating the kinematic factor is as follows:

$$k = \frac{E_1}{E_0} = \frac{1}{(1+A)^2} (\cos \theta \pm \sqrt{A^2 - \sin^2 \theta})^2 \quad (4.1)$$

$k$  = kinematic factor

$E_1$  = energy of the projectile atom after collision

$E_0$  = energy of the incident projectile atom

$A = \frac{m_2}{m_1}$  where  $m_1$  is the mass of the incident projectile atom and  $m_2$  is the mass of the target atom

$\theta$  = scattering angle

The full derivation process for the kinematic factor in ion scattering is found and referenced in appendix B.

Depth analysis can be undertaken because inelastic energy loss processes occur during penetration of the target by the ion. This extra energy loss can be related to the depth of the scattering event since the energy loss rates are well known. In a MEIS experiment a 2-D spectrum of the scattered ion as a function of energy and scattering angle is acquired from which the energy spectrum at a specific scattering angle is cut. This spectrum can then be converted into depth profiles of the first 30nm of a surface layer. For crystalline samples,

energy spectra are often taken by using double alignment conditions (channelling and blocking) to enhance surface information [73].

## Appendix B - Derivation of the Kinematic factor

The elastic collision between two isolated particles (of masses  $m_1$  and  $m_2$ ) can be solved by applying the principles of conservation of energy and the principles of conservation of momentum parallel and perpendicular to the direction of incidence. Let  $v_0$  and  $E_0 = m_1 v_0^2$  be the velocity and energy of an incident projectile atom of mass  $m_1$  before collision while the target atom of mass  $m_2$  is at rest. After collision,  $v_1$  is the velocity of the projectile atom and the energy of the projectile atom is represented by  $E_1 = m_1 v_1^2$ . The velocity and energy of the target atom after collision are  $v_2$  and  $E_2$  respectively where  $E_2 = m_2 v_2^2$ . The scattering angle is  $\theta$ , the recoil angle  $\phi$  and kinematic factor  $k$  [74].

Derivation based on the work of the CAICISS group in the Department of Physics at the University of Warwick [75].

Conservation of energy:

$$\frac{1}{2}m_1 v_0^2 = \frac{1}{2}m_1 v_1^2 + \frac{1}{2}m_2 v_2^2 \quad (B1)$$

Simplifying and rearranging for  $v_2^2$  :

$$v_2^2 = \frac{m_1 (v_0^2 - v_1^2)}{m_2} \quad (B2)$$

Conservation of momentum parallel to the incident direction:

$$m_1 v_0 = m_1 v_1 \cos \theta + m_2 v_2 \cos \phi \quad (B3)$$

Rearranging for  $m_2 v_2 \cos \phi$  and squaring:

$$m_1^2 v_0^2 + m_1^2 v_1^2 \cos^2 \theta - 2m_1^2 v_0 v_1 \cos \theta = m_2^2 v_2^2 \cos^2 \phi \quad (B4)$$

Conservation of momentum perpendicular to the incident direction:

$$0 = m_1 v_1 \sin \theta - m_2 v_2 \sin \phi \quad (B5)$$

Rearranging and squaring:

$$m_1^2 v_1^2 \sin^2 \theta = m_2^2 v_2^2 \sin^2 \phi \quad (B6)$$

Adding together equations (B4) and (B6):

$$m_1^2 v_0^2 + m_1^2 v_1^2 (\cos^2 \theta + \sin^2 \theta) - 2m_1^2 v_0 v_1 \cos \theta = m_2^2 v_2^2 (\cos^2 \phi + \sin^2 \phi) \quad (B7)$$



Recognising and substituting  $\cos^2\theta + \sin^2\theta = 1$ :

$$m_1^2 v_0^2 + m_1^2 v_1^2 - 2m_1^2 v_0 v_1 \cos\theta = m_2^2 v_2^2 \quad (B8)$$

Substituting equation (B2) into equation (B8):

$$m_1^2 v_0^2 + m_1^2 v_1^2 - 2m_1^2 v_0 v_1 \cos\theta = m_2 m_1 (v_0^2 - v_1^2) \quad (B9)$$

Dividing by  $m_1^2 v_0^2$  :

$$1 + \frac{v_1^2}{v_0^2} - \frac{2v_1 \cos\theta}{v_0} = \frac{m_2}{m_1} \left(1 - \frac{v_1^2}{v_0^2}\right) \quad (B10)$$

Setting  $\frac{m_2}{m_1} = A$  and rearranging:

$$(1 + A) \frac{v_1^2}{v_0^2} - \frac{2v_1 \cos\theta}{v_0} + (1 - A) = 0 \quad (B11)$$

Solving equation (B11) as a quadratic where  $X = \frac{v_1}{v_0}$  and simplifying gives:

$$\frac{v_1}{v_0} = \frac{\cos\theta \pm \sqrt{\cos^2\theta - (1+A)(1-A)}}{(1+A)} \quad (B12)$$

Multiplying out the terms in the square root:

$$\frac{v_1}{v_0} = \frac{\cos\theta \pm \sqrt{A^2 + \cos^2\theta - 1}}{(1+A)} \quad (B13)$$

Recognising and substituting  $\cos^2\theta - 1 = -\sin^2\theta$ :

$$\frac{v_1}{v_0} = \frac{\cos\theta \pm \sqrt{A^2 - \sin^2\theta}}{(1+A)} \quad (B14)$$

The kinematic factor is  $k = \frac{E_1}{E_0} = \frac{m_1 v_1^2}{m_1 v_0^2}$  therefore equation (B14) can be substituted in for  $\frac{v_1}{v_0}$  to give:

$$k = \frac{E_1}{E_0} = \frac{1}{(1+A)^2} (\cos\theta \pm \sqrt{A^2 - \sin^2\theta})^2 \quad (4.1)$$

K = kinematic factor

$m_1$  = mass of incident projectile atom

$v_0$  = velocity of incident projectile atom

$E_0$  = energy of the incident projectile atom

$m_2$  = mass of the target atom at rest

$v_1$  = velocity of the projectile atom after collision

$v_2$  = velocity of the target atom after collision

$E_1$  = energy of the projectile atom after collision

$E_2$  = energy of the target atom after collision

$\theta$  = scattering angle

$\phi$  = recoil angle

## Appendix C - Averaging and error equations

The average for pH data and XRF data was calculated using the following equation:

$$\bar{X} = \frac{x_1 + x_2 + x_3 + \dots + x_n}{n} \quad (C1)$$

$\bar{X}$  = mean average

$x$  = each value in the data set

$n$  = number of values in the data set

The errors for the pH data were calculated using the standard deviation of the mean as follows:

$$\sigma = \sqrt{\frac{(x_1 - \bar{X})^2 + (x_2 - \bar{X})^2 + (x_3 - \bar{X})^2 + \dots + (x_n - \bar{X})^2}{n}} \quad (C2)$$

$$error = \frac{\sigma}{\sqrt{n}} \quad (C3)$$

$\sigma$  = standard deviation

$x$  = each value in the data set

$\bar{X}$  = mean average

$n$  = number of values in the data set

The combined errors for the XRF data were calculated using the following equation:

$$combined\ error = \sqrt{(ex_1)^2 + (ex_2)^2 + (ex_3)^2 + \dots + (ex_n)^2} \quad (C4)$$

$ex_n$  = error of value n in the data set

## Appendix D - Raw soil sample data, average and error calculations

### D.1 Raw soil sample data, average and error for pH tests

*Raw soil sample data for pH tests*

Soil sample	Water pH			CaCl <sub>2</sub> pH		
AB	6.29	6.18	6.23	5.71	5.67	5.65
C	6.73	6.74	6.65	5.72	5.75	5.67
D	7.28	7.37	7.31	6.47	6.54	6.51

*Table D1: All raw soil experimental data*

*Average and error for pH tests*

Soil sample	Water pH			CaCl <sub>2</sub> pH		
	Average	Standard Deviation	Error	Average	Standard Deviation	Error
AB	6.233333	0.0449691	0.0260	5.676667	0.0249444	0.0144
C	6.706667	0.0402768	0.0233	5.713333	0.0329983	0.0191
D	7.320000	0.0374166	0.0216	6.506667	0.0286744	0.0166

*Table D2: Average and error calculations for all soil data*

### D.2 Raw XRF data for Soil A

Element	Composition/%	Error/± %
Si	75.30	1.4778
Fe	11.10	0.3359
Al	10.50	1.2280
Ti	1.73	0.0549
Pd	0.856	0.0710
Zr	0.239	0.0215
Mn	0.17	0.1064
Cu	0.0969	0.0291
V	0.0578	0.0296
Zn	0.0497	0.0199
Ni	0.0035	0.0251

*Table D3: Raw XRF Elemental Composition of soil A*

### D.3 Raw XRF data for Soil C

Element	Composition/%	Error/± %
Si	70.70	1.6169
Fe	15.40	0.4319
Al	11.60	1.4338
Ti	1.57	0.0574
Zr	0.345	0.0292
Cu	0.158	0.0413
Cr	0.133	0.0251
Zn	0.0646	0.0262
V	0.0398	0.0313
Ni	0.0049	0.0321

*Table D4: Raw XRF Elemental Composition of soil C*

### D.4 Raw XRF data for soil D

Element	Composition/%	Error/± %
Si	69.70	1.537
Fe	16.40	0.4344
Al	10.30	1.4268
Ti	1.56	0.0565
Pd	1.27	0.1046
Zr	0.384	0.0312
Cu	0.162	0.0409
Cr	0.102	0.0257
Zn	0.0784	0.0271
Mn	0.0579	0.1122
V	0.0228	0.032

*Table D5: Raw XRF Elemental Composition of soil D*

## Appendix E - Raw XRF data, average and error calculations

### E.1 Raw XRF data and average data for R06

#### Raw XRF data for R06

Obverse

Element	Metal (270)		Lime green (269)		Cream and green (271)	
	Composition/ %	Error/ ± %	Composition/ %	Error/ ± %	Composition/ %	Error/ ± %
Cu	48.3	0.1254	48.5	0.1254	46	0.1327
Sn	43.3	0.2453	43.3	0.245	46.1	0.2739
Pb	3.79	0.0481	3.75	0.0479	3.53	0.0502
Fe	2.11	0.04	2.11	0.0399	1.95	0.0425
Pd	0.775	0.02	0.773	0.0199	0.769	0.0213
Zn	0.532	0.017	0.529	0.017	0.623	0.0193
Rh	0.453	0.0165	0.444	0.0163	0.442	0.0176
Sb	0.372	0.0601	0.356	0.0593	0.276	0.0662
Ag	0.226	0.0198	0.204	0.0197	0.188	0.021
Ti	0.0693	0.1001	0	0	0	0
Mn	0.0607	0.0264	0.047	0.026	0	0
Co	0	0	0.0576	0.0149	0.0467	0.0165
Ru	0	0	0	0	0.0832	0.0094
Total/‰:	99.99		100.07		100.01	

Table E1: Raw XRF data for the obverse of R06

Reverse

Element	Metal and green (273)		Lime green (274)	
	Composition/ %	Error/ ± %	Composition/ %	Error/ ± %
Cu	51.9	0.1361	51.1	0.1414
Sn	41.8	0.2549	42.4	0.269
Pb	3.23	0.0481	3.55	0.0521
Fe	1.38	0.0348	1.35	0.0363
Pd	0.762	0.0212	0.776	0.0223
Rh	0.453	0.0177	0.451	0.0184
Zn	0.367	0.0174	0.182	0.0173
Ru	0.102	0.0097	0	0
Ag	0	0	0.194	0.0218
Sb	0	0	0	0
Ti	0	0	0	0
Mn	0	0	0	0
Co	0	0	0	0
Total/‰:	99.99		100	

Table E2: Raw XRF data for the reverse of R06

## Average and combined error for XRF data for R06

Average for metal areas

Element	Composition/ %	Error/ ± %
Cu	50.10	0.19
Sn	42.55	0.35
Pb	3.51	0.07
Fe	1.75	0.05
Pd	0.77	0.03
Rh	0.45	0.02
Zn	0.45	0.02
Sb	0.19	0.06
Ag	0.11	0.02
Ru	0.05	0.01
Ti	0.03	0.10
Mn	0.03	0.03
Co	0	0

Table 5.9: Average XRF Elemental Composition of metal areas on R06

Average for green areas

Element	Composition/ %	Error/ ± %
Cu	49.80	0.19
Sn	42.85	0.36
Pb	3.65	0.07
Fe	1.73	0.05
Pd	0.77	0.03
Rh	0.45	0.03
Zn	0.40	0.02
Ag	0.20	0.03
Sb	0.18	0.06
Co	0.03	0.02
Mn	0.02	0.03
Ti	0	0
Ru	0	0

Table 5.10: Average XRF Elemental Composition of green areas on R06

## E.2 Raw XRF data and average data for R02

### Raw XRF data for R02

Obverse

Element	Green (447)		Orange crust (301)	
	Composition/ %	Error/ ± %	Composition/ %	Error/ ± %
Cu	83.1	0.4006	80.2	0.3969
Pb	6.02	0.2349	7.1	0.2419
Sn	4.65	0.297	5.53	0.2849
Al	4.3	1.1471	4.19	1.1696
Fe	1.51	0.044	2.24	0.0596
Ni	0.158	0.0306	0.177	0.0319
Ti	0.133	0.0153	0.192	0.0168
Zn	0.0977	0.0359	0.209	0.0374
Si	0	0	0	0
Ag	0	0	0	0
Pd	0	0	0	0
Zr	0	0	0	0
Co	0	0	0.0939	0.015
V	0	0	0.0044	0.0135
As	0	0	0	0
Sb	0	0	0	0
Mn	0	0	0.0196	0.0247
Bi	0	0	0	0
Cr	0	0	0.0248	0.0113
Total/%:		99.97	99.9807	

Table E3: Raw XRF data for the obverse of R02

## Reverse

Element	Green (299)		Orange crust (298)	
	Composition/ %	Error/ ± %	Composition/ %	Error/ ± %
Cu	82.1	0.5042	67.5699	0.4092
Si	0	0	10.396	0.4695
Al	0	0	8.8603	2.2579
Ag	0	0	3.8847	0.1634
Pb	8.27	0.344	3.6086	0.3777
Sn	5.87	0.475	3.7446	0.2181
Fe	2.24	0.0715	1.1817	0.0608
Pd	0.842	0.1394	0	0
Ti	0.191	0.0214	0	0
Zr	0.177	0.0374	0.0204	0.0114
Ni	0.166	0.0392	0	0
Zn	0.0964	0.0451	0.1241	0.0286
Co	0.0869	0.0186	0	0
V	0.0007	0.0179	0	0
As	0	0	0.2701	0.0713
Sb	0	0	0.2309	0.0706
Mn	0	0	0.0623	0.0149
Bi	0	0	0.0464	0.0455
Cr	0	0		
Total/%:	100.04		100	

Table E4: Raw XRF data for the reverse of R02



### Average and combined error for XRF data of R02

Average for green areas

Element	Composition/ %	Error/ ± %
Cu	82.60	0.64
Pb	7.15	0.42
Sn	5.26	0.56
Al	2.15	1.15
Fe	1.88	0.08
Pd	0.42	0.14
Ti	0.16	0.03
Ni	0.16	0.05
Zn	0.10	0.06
Zr	0.09	0.04
Co	0.04	0.02
V	0	0.02
As	0	0
Sb	0	0
Mn	0	0
Bi	0	0
Si	0	0
Ag	0	0
Cr	0	0

Table 5.14: Average XRF Elemental Composition of green areas on R02

Average for orange crust

Element	Composition/ %	Error/ ± %
Cu	73.89	0.57
Al	6.53	2.54
Pb	5.35	0.45
Si	5.20	0.47
Sn	4.64	0.36
Ag	1.94	0.16
Fe	1.71	0.09
Zn	0.17	0.05
As	0.14	0.07
Sb	0.12	0.07
Ti	0.10	0.02
Ni	0.10	0.03
Co	0.05	0.02
Mn	0.04	0.03
Cr	0.03	0.01
Bi	0.02	0.05
Zr	0.01	0.01
V	0.00	0.01
Pd	0	0

Table 5.15: Average XRF Elemental Composition of orange crust on R02

### E.3 Raw XRF data and average data for R294

#### Raw XRF data for R294

Obverse

Element	Metal (282)		Orange (280)		Cream and green (281)	
	Composition/	Error/	Composition/	Error/	Composition/	Error/
	%	± %	%	± %	%	± %
Fe	55.6	0.1605	66.5	0.1762	31.5	0.1339
Cu	24.8	0.1062	14.7	0.0853	45.9	0.1464
Pb	8.78	0.073	9.14	0.0735	9.66	0.089
Sn	6.52	0.0906	5.69	0.0841	7.38	0.116
Ag	3.29	0.0419	3.04	0.0397	4.99	0.0595
Rh	0.332	0.017	0.337	0.0166	0.315	0.0205
Pd	0.29	0.0169	0.299	0.0165	0.269	0.0201
Zn	0.183	0.0148	0.283	0.0151	0.0539	0.0178
Ru	0.0934	0.0093	0	0	0	0
Ni	0.072	0.0153	0	0	0	0
Zr	0.0156	0.0044	0.0153	0.0044	0.0161	0.0053
Se	0.0004	0.0059	0	0	0	0
Cr	0	0	0	0	0	0
Au	0	0	0	0	0	0
Bi	0	0	0	0	0	0
Sb	0	0	0	0	0	0
Total/%:	99.98		100		100.08	

Table E5: Raw XRF data for the obverse of R294

Reverse

Element	Metal (285)		Orange (283)		Green (284)	
	Composition/	Error/	Composition/	Error/	Composition/	Error/
	%	± %	%	± %	%	± %
Fe	58.1	0.1654	69.1	0.1854	42.3	0.1421
Cu	21.2	0.0987	12.4	0.0812	37.7	0.127
Pb	9.27	0.0741	7.28	0.0673	8.93	0.0782
Sn	6.96	0.0932	6.59	0.0901	6.52	0.0951
Ag	3.42	0.0422	3.47	0.0422	3.45	0.0449
Rh	0.352	0.0168	0.3	0.016	0.309	0.0175
Pd	0.324	0.0168	0.294	0.0161	0.261	0.0174
Cr	0.178	0.0265	0	0	0	0
Zn	0.174	0.0142	0.114	0.0125	0.232	0.0163
Au	0.0272	0.0174	0	0	0	0
Bi	0.0063	0.0182	0.0512	0.0172	0	0
Se	0.0041	0.0061	0	0	0.0006	0.0063
Sb	0	0	0.36	0.0426	0.292	0.0455
Ru	0	0	0	0	0	0
Ni	0	0	0	0	0	0
Zr	0	0	0	0	0	0
Total/%:	100.02		99.96		99.99	

Table E6: Raw XRF data for the reverse of R294

### Average and combined error for XRF data of R294

Average for metal areas

Element	Composition/ %	Error/ ± %
Fe	56.85	0.23
Cu	23.00	0.20
Pb	9.03	0.10
Sn	6.74	0.13
Ag	3.36	0.06
Rh	0.34	0.02
Pd	0.31	0.02
Zn	0.18	0.02
Cr	0.09	0.03
Ru	0.05	0.01
Ni	0.04	0.02
Au	0.01	0.02
Zr	0.01	0.00
Bi	0.00	0.02
Se	0.00	0.02
Sb	0.00	0.01

Table E7: Average XRF elemental composition of metal areas on R294

Average for orange areas

Element	Composition/ %	Error/ ± %
Fe	67.80	0.30
Cu	13.55	0.12
Pb	8.21	0.10
Sn	6.14	0.12
Ag	3.26	0.06
Rh	0.32	0.02
Pd	0.30	0.02
Zn	0.20	0.02
Sb	0.18	0.04
Bi	0.03	0.02
Zr	0.01	0.00
Cr	0	0
Ru	0	0
Ni	0	0
Au	0	0
Se	0	0

Table E8: Average XRF elemental composition of orange areas on R294

Average for green areas

Element	Composition/ %	Error/ ± %
Cu	41.80	0.20
Fe	36.90	0.20
Pb	9.30	0.12
Sn	6.95	0.15
Ag	4.22	0.08
Rh	0.31	0.03
Pd	0.27	0.03
Sb	0.15	0.05
Zn	0.14	0.02
Zr	0.01	0.01
Se	0.00	0.01
Bi	0	0
Cr	0	0
Ru	0	0
Ni	0	0
Au	0	0

Table E9: Average XRF elemental composition of green areas on R294

## E.4 Raw XRF data and average data for R253B

### Raw XRF data for R253B

Obverse

Element	Metal (289)		Green/Cream (290)	
	Composition/ %	Error/ ± %	Composition/ %	Error/ ± %
Sn	42.5	0.2283	40.4	0.3182
Fe	28.1	0.1391	16.4	0.1431
Cu	25.3	0.1016	40.5	0.1699
Cd	1.39	0.0224	0	0
Pb	1	0.0256	1.23	0.0418
Pd	0.718	0.0176	0.699	0.0258
Rh	0.389	0.0142	0.417	0.0217
Ti	0.214	0.1064	0.127	0.1452
Ag	0.113	0.0167	0.165	0.0245
As	0.0821	0.0141	0	0
Zn	0.0614	0.0115	0	0
Ni	0.0355	0.0131	0	0
Se	0.0114	0.0043	0.0158	0.007
Mn	0.0038	0.0326	0.036	0.0443
Sb	0	0	0	0
Ru	0	0	0	0
Total/ %:	99.92		99.99	

Table E10: Raw XRF data for the obverse of R253B

Reverse

Element	Metal (286)		Green (287)		Cream (288)	
	Composition/ %	Error/ ± %	Composition/ %	Error/ ± %	Composition/ %	Error/ ± %
Sn	45.1	0.2532	45.1	0.2518	45.3	0.2655
Cu	31.5	0.1166	34.3	0.1185	27.7	0.1164
Fe	20.8	0.1262	17.6	0.1144	24.1	0.1436
Pb	1.2	0.03	1.21	0.0298	1.22	0.0315
Pd	0.748	0.0192	0.75	0.0189	0.73	0.0199
Rh	0.431	0.0159	0.422	0.0154	0.454	0.0168
Sb	0	0	0.307	0.0591	0	0
Ti	0	0	0	0	0.315	0.1221
Ag	0.173	0.0183	0.161	0.0183	0.156	0.0196
Ru	0	0	0.0978	0.0084	0.105	0.0092
As	0	0	0.0484	0.0165	0	0
Zn	0.0319	0.0129	0.018	0.0126	0	0
Se	0.0189	0.0051	0.0161	0.005	0.0107	0.0051
Cd	0	0	0	0	0	0
Ni	0	0	0	0	0	0
Mn	0	0	0	0	0	0
Total/ %:	100		100.03		100.09	

Table E11: Raw XRF data for the reverse of R253B

### Average and combined error for XRF data of R253B

Average for metal areas

Element	Composition/ %	Error/ ± %
Sn	43.80	0.30
Cu	28.40	0.20
Fe	24.45	0.19
Pb	1.10	0.04
Pd	0.73	0.03
Cd	0.70	0.02
Rh	0.41	0.02
Ag	0.14	0.03
Ti	0.11	0.11
Zn	0.05	0.02
As	0.04	0.01
Ni	0.02	0.01
Se	0.02	0.01
Mn	0.00	0.03
Sb	0	0
Ru	0	0

Table E12: Average XRF elemental composition of metal areas on R253B

Average for green and cream areas

Element	Composition/ %	Error/ ± %
Sn	43.60	0.50
Cu	34.17	0.24
Fe	19.37	0.23
Pb	1.22	0.06
Pd	0.73	0.04
Rh	0.43	0.03
Ag	0.16	0.04
Ti	0.15	0.19
Sb	0.10	0.06
Ru	0.07	0.01
As	0.02	0.02
Se	0.01	0.01
Mn	0.01	0.04
Zn	0.01	0.01
Cd	0	0
Ni	0	0

Table E13: Average XRF elemental composition of green and cream areas on R253B

## E.5 Raw XRF data and average data for R03

### Raw XRF data for R03

Obverse

Element	Green (309)		Cream (308)	
	Composition/ %	Error/ ± %	Composition/ %	Error/ ± %
Cu	39.6	0.1221	41.8	0.1272
Sn	34	0.2464	32.5	0.2448
Pb	18.5	0.1133	17.9	0.1143
Fe	4.67	0.0625	4.61	0.0626
Zn	1.32	0.0241	1.38	0.0252
Pd	0.734	0.0254	0.734	0.026
Rh	0.553	0.0226	0.582	0.0235
Ag	0.445	0.028	0.443	0.0284
Ru	0.116	0.012	0.113	0.0124
Zr	0.0394	0.0061	0.0307	0.0064
Mn	0.0304	0.0314	0	0
Ti	0	0	0.0145	0.1115
Sb	0	0	0	0
Re	0	0	0	0
Total/ %:				
100.01		100.11		

Table E14: Raw XRF data for the obverse of R03

Reverse

Element	Green (306)		Cream line (307)	
	Composition/ %	Error/ ± %	Composition/ %	Error/ ± %
Cu	42.1	0.1256	44.2	0.1271
Sn	33.2	0.2441	30.4	0.2317
Pb	17.8	0.1122	18.2	0.1141
Fe	3.65	0.0559	3.75	0.0551
Zn	1.01	0.0225	1.42	0.0246
Pd	0.728	0.0225	0.703	0.0252
Rh	0.573	0.0229	0.555	0.0228
Ag	0.479	0.0283	0.452	0.0271
Sb	0.305	0.0689	0.301	0.0654
Ru	0.109	0.012	0	0
Re	0.0705	0.0309	0	0
Zr	0.0291	0.0061	0.0356	0.0062
Mn	0	0	0	0
Ti	0	0	0	0
Total/ %:	100.05		100.02	

Table E15: Raw XRF data for the reverse of R03

### Average and combined error for XRF data of R03

Average for green areas

Element	Composition/ %	Error/ ± %
Cu	40.85	0.18
Sn	33.60	0.40
Pb	18.15	0.16
Fe	4.16	0.08
Zn	1.17	0.03
Pd	0.73	0.03
Rh	0.56	0.03
Ag	0.46	0.03
Ru	0.11	0.02
Re	0.04	0.03
Zr	0.03	0.01
Sb	0.15	0.07
Mn	0.02	0.03
Ti	0	0

Table E16: Average XRF elemental composition of green areas on R03

Average for cream areas

Element	Composition/ %	Error/ ± %
Cu	43.00	0.20
Sn	31.45	0.34
Pb	18.05	0.16
Fe	4.18	0.08
Zn	1.40	0.04
Pd	0.72	0.04
Rh	0.57	0.03
Ag	0.45	0.04
Sb	0.15	0.07
Ru	0.06	0.01
Zr	0.03	0.01
Re	0	0
Mn	0	0
Ti	0	0

Table E17: Average XRF elemental composition of cream areas on R03

## E.6 Raw XRF data and average data for V186

### Raw XRF data for V186

Obverse

Element	Cream/brown (186)		Light green (360)		Brown (361)	
	Composition/ %	Error/ ± %	Composition/ %	Error/ ± %	Composition/ %	Error/ ± %
Cu	72.9	0.1499	74.1	0.1565	73.5	0.1565
Sn	14	0.139	12.9	0.1388	13.3	0.1414
Fe	7.01	0.0534	7.03	0.055	6.99	0.0555
Zn	1.89	0.0266	1.78	0.0271	1.88	0.0277
As	1.57	0.0297	1.55	0.031	1.52	0.0324
Pb	0.868	0.0323	0.901	0.0345	1.19	0.0381
Bi	0.714	0.025	0.645	0.0256	0.601	0.0255
Rh	0.409	0.0186	0.399	0.0184	0.402	0.0185
Pd	0.406	0.0178	0.383	0.019	0.423	0.0194
Ag	0.106	0.0176	0.0824	0.018	0.107	0.018
Mn	0.0831	0.0209	0.0554	0.0213	0.0606	0.0216
Se	0.0238	0.0063	0.0222	0.0068	0.0125	0.0069
Pt	0.0019	0.029	0	0	0	0
Ru	0	0	0.0708	0.0099	0	0
Zr	0	0	0	0	0	0
Total/‰:	99.98		99.92		99.99	

Table E18: Raw XRF data for the obverse of V186

Reverse

Element	Cream (367)		Dark green (368)	
	Composition/ %	Error/ ± %	Composition/ %	Error/ ± %
Cu	72.1	0.1576	73	0.1515
Sn	12.8	0.1383	14.2	0.1422
Fe	9.07	0.063	6.53	0.0524
Zn	2.04	0.0288	2.1	0.0281
As	1.48	0.0305	1.64	0.0311
Pb	0.858	0.0338	0.954	0.0343
Bi	0.664	0.0257	0.727	0.0259
Rh	0.401	0.0186	0.403	0.0184
Pd	0.389	0.0191	0.409	0.0192
Ag	0	0	0	0
Mn	0.0612	0.0217	0.065	0.0213
Se	0.0219	0.0066	0.023	0.0066
Pt	0	0	0	0
Ru	0	0	0	0
Zr	0.0284	0.0056	0	0
Total/‰:	99.91		100.05	

Table E19: Raw XRF data for the reverse of V186

## Average and combined error for XRF data of V186

Average for cream areas

Element	Composition/ %	Error/ ± %
Cu	72.50	0.20
Sn	13.40	0.20
Fe	8.04	0.08
Zn	1.97	0.04
As	1.53	0.04
Pb	0.86	0.05
Bi	0.69	0.04
Rh	0.41	0.03
Pd	0.40	0.03
Mn	0.07	0.03
Ag	0.05	0.02
Se	0.02	0.01
Zr	0.01	0.01
Pt	0.00	0.03
Ru	0	0

Table E20: Average XRF elemental composition of cream areas on V186

Average for green/brown areas

Element	Composition/ %	Error/ ± %
Cu	73.53	0.27
Sn	13.47	0.24
Fe	6.85	0.09
Zn	1.92	0.05
As	1.57	0.06
Pb	1.02	0.06
Bi	0.66	0.04
Pd	0.41	0.03
Rh	0.40	0.03
Ag	0.06	0.03
Mn	0.06	0.04
Ru	0.02	0.01
Se	0.02	0.01
Pt	0	0
Zr	0	0

Table E21: Average XRF elemental composition of green/brown areas on V186

## E.7 Raw XRF data and average data for V112

### Raw XRF data for V112

Obverse

Element	Multi-coloured centre (184)		Brown (450)	
	Composition/ %	Error/ ± %	Composition/ %	Error/ ± %
Cu	86.9001	0.6039	92.4245	0.4992
Pb	7.5184	0.498	4.6925	0.3681
Si	2.6538	0.2042	0.9581	0.1662
Al	1.2025	0.9163	0.1899	0.6806
Fe	1.1158	0.0375	1.3932	0.0402
As	0.3749	0.0254	0.2437	0.0185
Sn	0.1024	0.0471	0.005	0.0368
Bi	0.0602	0.0213	0.0338	0.0182
Ag	0.0555	0.0105	0.0421	0.0093
Sb	0.0158	0.0236	0.016	0.0238
Zr	0.0005	0.0005	0.0012	0.0006
Ni			0	0
Total/%:		100	100	

Table E22: Raw XRF data for the obverse of V112



Reverse

Element	Multi-coloured top (449)		Brown edge (452)	
	Composition/ %	Error/ ± %	Composition/ %	Error/ ± %
Cu	90.4703	0.5102	91.2378	0.5764
Pb	4.6363	0.393	5.6036	0.4534
Si	1.8495	0.1905	1.3557	0.1994
Al	0.6391	0.7681	0.6846	2.5797
Fe	2.0193	0.0484	0.7309	0.0353
As	0.2457	0.0192	0.2841	0.0231
Sn	0.0063	0.0382	0.0201	0.0437
Bi	0.0594	0.0212	0.0269	0.0199
Ag	0.0441	0.0097	0.0355	0.01
Sb	0	0	0	0
Zr	0.0009	0.0006	0.0015	0.0007
Ni	0.029	0.0233	0.0194	0.0254
Total/‰:	99.9999		100.0001	

Table E23: Raw XRF data for the reverse of V112

### Average and combined error for XRF data of V112

Average for multi-coloured corrosion

Average for Brown areas

Element	Composition/ %	Error/ ± %
Cu	88.69	0.79
Pb	6.08	0.63
Si	2.25	0.28
Fe	1.57	0.06
Al	0.92	1.20
As	0.31	0.03
Bi	0.06	0.03
Sn	0.05	0.06
Ag	0.05	0.01
Ni	0.03	0.02
Sb	0.01	0.02
Zr	0	0

Table 7.1: Average XRF elemental composition of multi-coloured areas on V112

Element	Composition/ %	Error/ ± %
Cu	91.83	0.76
Pb	5.15	0.58
Si	1.16	0.26
Fe	1.06	0.05
Al	0.44	2.67
As	0.26	0.03
Ag	0.04	0.01
Bi	0.03	0.03
Sn	0.01	0.06
Ni	0.01	0.03
Sb	0.01	0.02
Zr	0	0

Table E24: Average XRF elemental composition of brown areas on V112

## E.8 Raw XRF data and average data for V114

### Raw XRF data for V114

Obverse

Element	Cream centre (185)		Maroon (372)		Green (441)	
	Composition/ %	Error/ ± %	Composition/ %	Error/ ± %	Composition/ %	Error/ ± %
Cu	94.0332	0.283	92.0541	0.1202	84.6829	0.3054
Ag	2.3598	0.1041	3.378	0.0525	3.432	0.1325
Zn	1.5045	0.0443	1.9139	0.0207	1.7979	0.0504
As	1.3638	0.0459	1.2108	0.0184	1.7379	0.0548
Sn	0.3162	0.0527	0.3386	0.023	0.3451	0.058
Fe	0.3008	0.0297	0.2819	0.0123	1.0375	0.048
Sb	0.0727	0.0399	0.0639	0.0165	0.0462	0.0383
Bi	0.0286	0.0195	0.0346	0.0085	0.0249	0.0204
Mn	0.0093	0.015	0	0	0.0584	0.0142
Zr	0.0091	0.0084	0.0073	0.0035	0.0068	0.0085
Si	0.002	0.1397	0	0	1.0586	0.214
Pb	0	0	0	0	0	0
Al	0	0	0	0	5.7719	1.2701
Ni	0	0	0	0	0	0
Total/ %:	100		99.28		100.0001	

Table E25: Raw XRF data for the obverse of V114

Reverse

Element	Cream (373)		Maroon (439)		Green (440)	
	Composition/ %	Error/ ± %	Composition/ %	Error/ ± %	Composition/ %	Error/ ± %
Cu	93.1439	0.1194	78.1533	0.9664	93.9479	0.2762
Ag	1.9685	0.0407	0.7895	0.0373	2.3712	0.1042
Zn	2.0977	0.0215	0	0	1.8488	0.0479
As	1.1938	0.0183	0.6102	0.0576	1.062	0.0406
Sn	0.2819	0.0214	0.2146	0.0556	0.2897	0.0505
Fe	0.3286	0.0129	0.1823	0.0208	0.3252	0.0299
Sb	0.0681	0.0167	0.0245	0.0244	0.1167	0.0445
Bi	0.0301	0.0083	0.0408	0.0205	0.0203	0.0182
Mn	0.0106	0.0064	0	0	0	0
Zr	0.0082	0.0035	0.0015	0.0006	0.0136	0.0087
Si	0	0	1.2323	0.1626	0	0
Pb	0	0	18.6763	0.8099	0	0
Al	0	0	0.0747	1.0641	0	0
Ni	0	0	0	0	0.0048	0.0273
Total/ %:	99.13		100		100.0002	

Table E26: Raw XRF data for the reverse of V114

### Average and combined error for XRF data of V114

Average for cream areas

Element	Composition/ %	Error/ ± %
Cu	93.59	0.31
Ag	2.16	0.11
Zn	1.80	0.05
As	1.28	0.05
Fe	0.32	0.03
Sn	0.30	0.06
Sb	0.07	0.04
Bi	0.03	0.02
Mn	0.01	0.01
Zr	0.01	0.01
Si	0.00	0.14
Pb	0	0
Al	0	0
Ni	0	0

*Table E27: Average XRF elemental composition of cream areas on V114*

Average for maroon areas

Element	Composition/ %	Error/ ± %
Cu	85.10	0.97
Pb	9.34	0.81
Ag	2.08	0.06
Zn	0.96	0.02
As	0.91	0.06
Si	0.62	0.16
Sn	0.28	0.06
Fe	0.23	0.02
Sb	0.04	0.03
Bi	0.04	0.02
Al	0.04	1.06
Zr	0	0
Mn	0	0
Ni	0	0

*Table E28: Average XRF elemental composition of maroon areas on V114*

Average for green areas

Element	Composition/ %	Error/ ± %
Cu	89.32	0.41
Ag	2.90	0.17
Al	2.89	1.27
Zn	1.82	0.07
As	1.40	0.07
Fe	0.68	0.06
Si	0.53	0.21
Sn	0.32	0.08
Sb	0.08	0.06
Mn	0.03	0.01
Bi	0.02	0.03
Zr	0.01	0.01
Ni	0.00	0.03
Pb	0	0

*Table E29: Average XRF elemental composition of green areas on V114*

## E.9 Raw XRF data and average data for Coin C

### Raw XRF data for Coin C

Obverse

Element	Brown (312)		Cream (313)	
	Composition/ %	Error/ ± %	Composition/ %	Error/ ± %
Cu	93.7253	0.2633	73.0424	0.6572
Si	4.0303	0.2657	11.9962	0.4118
Al	1.014	0.8487	12.756	1.8767
Bi	0.5273	0.0485	1.091	0.0713
As	0.2845	0.0227	0.5327	0.0568
Ag	0.1623	0.0325	0.0671	0.0126
Sn	0.092	0.0326	0.0729	0.0457
Zn	0.0883	0.0227	0	0
Fe	0.0398	0.0225	0.4071	0.0273
Sb	0.0248	0.0329	0.0324	0.0265
Mn	0.0077	0.0157	0	0
Zr	0.0036	0.0083	0.0021	0.0007
Total/%:	100		100	

Table E30: Raw XRF data for the obverse of Coin C

Reverse

Element	Black (310)		Green (311)	
	Composition/ %	Error/ ± %	Composition/ %	Error/ ± %
Cu	97.4613	0.2562	93.0233	0.2624
Si	1.4181	0.1997	3.9848	0.2562
Bi	0.4541	0.0448	0.8988	0.0633
As	0.2771	0.0218	0.6249	0.0326
Ag	0.1427	0.031	0.1639	0.0332
Zn	0.0881	0.0228	0.0985	0.0234
Sn	0.0685	0.0297	0.0914	0.0331
Fe	0.0324	0.0217	0.0856	0.0236
Sb	0.0285	0.0335	0.0287	0.0341
Al	0.027	0.7313	0.9977	0.8983
Mn	0	0	0	0
Zr	0.0023	0.0082	0.0024	0.0088
Total/%:	100		100	

Table E31: Raw XRF data for the reverse of Coin C

### Average and combined error for XRF data of Coin C

Average for green/brown area (as very similar)

Element	Composition/ %	Error/ ± %
Cu	93.37	0.37
Si	4.01	3.99
Al	1.01	1.36
Bi	0.71	0.08
As	0.46	0.04
Ag	0.16	0.05
Zn	0.09	0.03
Sn	0.09	0.05
Fe	0.06	0.03
Sb	0.03	0.05
Mn	0.00	0.02
Zr	0.00	0.01

*Table E32: Average XRF elemental composition of green/brown areas on Coin C*

### E.10 Raw XRF data and average data for Coin D

#### Raw XRF data

Obverse

Element	Green (314)		Orange (315)	
	Composition/ %	Error/ ± %	Composition/ %	Error/ ± %
Cu	81.0736	0.4265	71.525	0.4221
Sn	12.2419	0.3651	9.0092	0.3385
Al	2.179	1.0218	15.1437	2.0957
Zn	1.6566	0.0523	1.5679	0.0556
As	1.5964	0.0767	1.4307	0.0816
Fe	0.5116	0.0392	0.6944	0.0471
Bi	0.395	0.058	0.374	0.0622
Sb	0.2475	0.0701	0.1655	0.066
Ag	0.0632	0.0194	0.0466	0.021
Zr	0.0185	0.011	0.0173	0.0115
Mn	0.0167	0.0164	0.0258	0.016
Total/%:	100		100	

*Table E33: Raw XRF data for the obverse of coin D*

## Reverse

Element	Green (316)		Orange (317)	
	Composition/ %	Error/ ± %	Composition/ %	Error/ ± %
Cu	80.5412	0.4131	69.1731	0.4259
Sn	11.1736	0.3476	9.2834	0.3424
Al	3.611	1.222	17.5267	2.2343
Zn	1.7547	0.054	1.4063	0.0527
As	1.5914	0.0789	1.2661	0.0775
Fe	0.5507	0.0398	0.7211	0.0478
Bi	0.4999	0.0638	0.3615	0.0605
Sb	0.1915	0.0653	0.1563	0.0645
Ag	0.0576	0.02	0.0588	0.0212
Zr	0.0247	0.0117	0.0107	0.0107
Mn	0.0038	0.0154	0.036	0.0162
Total/ %:	100		100	

Table E34: Raw XRF data for the reverse of coin D

## Average and combined error for XRF data for Coin D

### Average for green areas

Element	Composition/ %	Error/ ± %
Cu	80.81	0.59
Sn	11.71	0.50
Al	2.90	1.59
Zn	1.71	0.08
As	1.59	0.11
Fe	0.53	0.06
Bi	0.45	0.09
Sb	0.22	0.10
Ag	0.06	0.03
Zr	0.02	0.02
Mn	0.01	0.02

Table 5.4: Average XRF Elemental Composition of green areas on Coin D

### Average for orange areas

Element	Composition/ %	Error/ ± %
Cu	70.35	0.60
Al	16.34	3.06
Sn	9.15	0.48
Zn	1.49	0.08
As	1.35	0.11
Fe	0.71	0.07
Bi	0.37	0.09
Sb	0.16	0.09
Ag	0.05	0.03
Mn	0.03	0.02
Zr	0.01	0.02

Table 5.5: Average XRF Elemental Composition of orange areas on Coin D

## E.11 Raw XRF data and average data for Coin A

### Raw XRF data for Coin A

Obverse

Element	Black/metal (260)		Orange (259)	
	Composition/ %	Error/ ± %	Composition/ %	Error/ ± %
Ag	96.8	0.2636	79.5	0.2067
Pb	0.808	0.0222	0.459	0.0172
Pd	0.741	0.0255	0.672	0.0218
Fe	0.658	0.0357	18.6	0.1282
Cu	0.548	0.0171	0.325	0.0132
Au	0.231	0.0171	0.135	0.0132
Bi	0.199	0.0128	0.32	0.0127
Total/‰:	99.99		100.01	

Table E35: Raw XRF data for the obverse of coin A

Reverse

Element	Raised metal (261)		Black/metal (262)	
	Composition/ %	Error/ ± %	Composition/ %	Error/ ± %
Ag	97.2	0.2505	97.3	0.2558
Pb	0.802	0.0209	0.819	0.0214
Pd	0.685	0.0246	0.762	0.0247
Cu	0.647	0.0173	0.386	0.0145
Fe	0.328	0.0277	0.393	0.0303
Au	0.166	0.0143	0.183	0.0152
Bi	0.16	0.0115	0.199	0.0122
Total/‰:	99.99		100.04	

Table E36: Raw XRF data for the reverse of coin A

### Average and combined error for XRF data of Coin A

Average for metal areas

Element	Composition/ %	Error/ ± %
Ag	97.10	0.50
Pb	0.81	0.04
Pd	0.73	0.04
Cu	0.53	0.03
Fe	0.46	0.05
Au	0.19	0.03
Bi	0.19	0.02

Table E37: Average XRF elemental composition of metal areas on coin A

## E.12 Raw XRF data and average data for Coin B

### Raw XRF data for coin B

Obverse

Element	Smooth metal (264)		Black (263)		Black (265)	
	Composition/ %	Error/ ± %	Composition/ %	Error/ ± %	Composition/ %	Error/ ± %
Ag	97.9	0.254	98.6	0.2588	98.4	0.2575
Pd	0.7	0.025	0.716	0.0253	0.795	0.0247
Pb	0.423	0.0175	0.0845	0.0129	0.0909	0.0131
Fe	0.397	0.0303	0.395	0.0309	0.453	0.0309
Cu	0.337	0.0136	0.116	0.01	0.134	0.0102
Bi	0.219	0.0121	0.102	0.0103	0.0962	0.0102
Au	0.04	0.0122	0	0	0	0
Total/ %:	100.02		100.01		99.97	

Table E38: Raw XRF data for the obverse of coin B

Reverse

Element	Metal (267)		Black/metal (266)		Black (268)	
	Composition/ %	Error/ ± %	Composition/ %	Error/ ± %	Composition/ %	Error/ ± %
Ag	97.4	0.261	97.4	0.2564	98	0.2578
Pd	0.72	0.0257	0.788	0.0246	0.712	0.0253
Pb	0.674	0.0207	0.618	0.0194	0.352	0.0168
Cu	0.6	0.0174	0.684	0.018	0.356	0.014
Bi	0.297	0.0135	0.215	0.0121	0.18	0.0117
Fe	0.216	0.0268	0.316	0.029	0.355	0.0293
Au	0.0571	0.0127	0	0	0.0345	0.0117
Total/ %:	99.96		100.02		99.99	

Table E39: Raw XRF data for the reverse of coin B



### Average and combined error for XRF data of coin B

Average for metal areas

Element	Composition/ %	Error/ ± %
Ag	97.57	0.45
Pd	0.74	0.04
Pb	0.57	0.03
Cu	0.54	0.03
Fe	0.31	0.04
Bi	0.24	0.02
Au	0.03	0.02

Table 6.4: Average XRF Elemental Composition of metal areas on coin B

Average for black areas

Element	Composition/ %	Error/ ± %
Ag	98.33	0.45
Pd	0.74	0.04
Pb	0.18	0.03
Cu	0.20	0.02
Fe	0.40	0.05
Bi	0.13	0.02
Au	0.01	0.01

Table 6.5: Average XRF Elemental Composition of black areas on coin B

### E.13 Raw XRF data and average data for M516

#### Raw XRF data for M516

Obverse

Element	Cream centre (243)		Light grey/Brown (244)	
	Composition/ %	Error/ ± %	Composition/ %	Error/ ± %
Ag	96.8	0.2506	96.8	0.2546
Cu	1.06	0.0216	0.94	0.0209
Pd	0.754	0.024	0.752	0.0244
Pb	0.597	0.019	0.589	0.0192
Fe	0.603	0.0333	0.778	0.0368
Au	0.177	0.015	0.176	0.0154
Ru	0	0	0	0
Zn	0	0	0	0
Total/%:	99.99		100.04	

Table E40: Raw XRF data for the obverse of M516

Reverse

Element	Cream (241)		Brown (242)	
	Composition/ %	Error/ ± %	Composition/ %	Error/ ± %
Ag	96.7	0.2485	96.7	0.2521
Cu	1.17	0.0224	0.781	0.0191
Pd	0.744	0.0238	0.745	0.0242
Pb	0.613	0.0189	0.576	0.0189
Fe	0.515	0.0319	0.981	0.0397
Au	0.187	0.015	0.162	0.0149
Ru	0.0233	0.0064	0	0
Zn	0	0	0.0137	0.0061
Total/%:	99.95		99.96	

Table E41: Raw XRF data for the reverse of M516

## Average and combined error for XRF data of M516

Average for cream areas

Element	Composition/ %	Error/ ± %
Ag	96.75	0.35
Cu	1.12	0.03
Pd	0.75	0.03
Pb	0.61	0.03
Fe	0.56	0.05
Au	0.18	0.02
Ru	0.01	0.01
Zn	0	0

Table 6.10: Average XRF elemental composition of cream areas on M516

Average for light grey/brown areas

Element	Composition/ %	Error/ ± %
Ag	96.75	0.36
Fe	0.88	0.05
Cu	0.86	0.03
Pd	0.75	0.03
Pb	0.58	0.03
Au	0.17	0.02
Zn	0.01	0.01
Ru	0	0

Table 6.11: Average XRF elemental composition of light grey/brown areas on M516

## E.14 Raw XRF data and average data for M805

### Raw XRF data for M805

Obverse

Element	Metal (254)		Brown/orange (253)	
	Composition/ %	Error/ ± %	Composition/ %	Error/ ± %
Ag	94.2	0.2359	92.1	0.2314
Cu	2.08	0.0283	2.01	0.0279
Pd	0.727	0.0228	0.71	0.0225
Fe	2.31	0.0516	4.66	0.0699
Pb	0.415	0.0162	0.41	0.0162
Au	0.104	0.0124	0.0969	0.0123
Bi	0.0328	0.0089	0.045	0.0091
Ti	0.146	0.1232	0	0
Total/‰:	100.01		100.03	

Table E42: Raw XRF data for the obverse of M805

Reverse

Element	Metal (250)		Brown (252)		Black (251)	
	Composition/ %	Error/ ± %	Composition/ %	Error/ ± %	Composition/ %	Error/ ± %
Ag	96.4	0.2504	92	0.238	96.3	0.2521
Cu	1.76	0.0271	1.36	0.0241	1.73	0.0271
Pd	0.754	0.0239	0.663	0.0237	0.746	0.0242
Fe	0.527	0.0321	5.36	0.0766	0.686	0.0351
Pb	0.396	0.0165	0.443	0.0174	0.405	0.017
Au	0.0945	0.0129	0.082	0.0137	0.0969	0.0133
Bi	0.0505	0.0094	0.051	0.0098	0.0511	0.0097
Ti	0	0	0	0	0	0
Total/‰:	99.98		99.96		100.02	

Table E43: Raw XRF data for the reverse of M805

### Average and combined error for XRF data of M805

Average for metal areas

Element	Composition/ %	Error/ ± %
Ag	95.30	0.30
Cu	1.92	0.04
Fe	1.42	0.06
Pd	0.74	0.03
Pb	0.41	0.02
Au	0.10	0.02
Ti	0.07	0.12
Bi	0.04	0.01

Table E44: Average XRF elemental composition of metal areas on M805

Average for brown areas

Element	Composition/ %	Error/ ± %
Ag	92.05	0.33
Fe	5.01	0.10
Cu	1.69	0.04
Pd	0.69	0.03
Pb	0.43	0.02
Au	0.09	0.02
Bi	0.05	0.01
Ti	0	0

Table E45: Average XRF elemental composition of brown areas on M805

## E.15 Raw XRF data and average data for M804

### Raw XRF data for M804

Obverse

Element	Metal (240)		Black (239)	
	Composition/ %	Error/ ± %	Composition/ %	Error/ ± %
Ag	92.4	0.2439	91.8	0.2333
Fe	2.46	0.0544	2.12	0.0498
Cu	2.27	0.0304	1.99	0.0275
Pb	1.68	0.0278	1.57	0.0257
Cd	0	0	1.37	0.0339
Pd	0.739	0.0241	0.729	0.0229
Au	0.344	0.0181	0.327	0.0169
Bi	0.0665	0.0107	0.0674	0.0101
Ru	0	0	0	0
Total/ %:	99.96		99.97	

Table E46: Raw XRF data for the obverse of M804

## Reverse

Element	Metal (238)		Black (237)	
	Composition/ %	Error/ ± %	Composition/ %	Error/ ± %
Ag	95.2	0.2457	93.9	0.2441
Cu	2.19	0.0295	2.11	0.0289
Cd	0	0	1.35	0.0358
Pb	1.36	0.025	1.31	0.0245
Pd	0.735	0.0238	0.75	0.0237
Au	0.32	0.0172	0.298	0.0166
Fe	0.241	0.0263	0.292	0.0266
Ru	0	0	0.0223	0.0064
Bi	0	0	0	0
Total/‰:	100.05		100.03	

Table E47: Raw XRF data for the reverse of M804

## Average and combined error for XRF data of M804

Average for metal areas

Element	Composition/ %	Error/ ± %
Ag	93.80	0.35
Cu	2.23	0.04
Pb	1.52	0.04
Fe	1.35	0.06
Pd	0.74	0.03
Au	0.33	0.03
Bi	0.03	0.01
Cd	0	0
Ru	0	0

Table 7.2: Average XRF elemental composition of metal areas on M804

Average for black areas

Element	Composition/ %	Error/ ± %
Ag	92.85	0.34
Cu	2.05	0.04
Pb	1.44	0.04
Cd	1.36	0.05
Fe	1.21	0.06
Pd	0.74	0.03
Au	0.31	0.02
Bi	0.03	0.01
Ru	0.01	0.01

Table E48: Average XRF elemental composition of black areas on M804

## E.16 Raw XRF data and average data for M821

### Raw XRF data for M821

Obverse

Element	Metal (245)		Brown (247)		Black (246)	
	Composition/ %	Error/ ± %	Composition/ %	Error/ ± %	Composition/ %	Error/ ± %
Ag	94.7	0.2382	90	0.2378	94.5	0.2365
Cu	3.25	0.0349	2.7	0.0334	3.13	0.0342
Pd	0.734	0.0229	0.742	0.0237	0.741	0.0228
Pb	0.652	0.0187	0.625	0.0194	0.696	0.0189
Fe	0.445	0.0294	4.27	0.0697	0.725	0.0334
Au	0.195	0.0147	0.207	0.0158	0.209	0.0149
Bi	0.0573	0.0095	0.0853	0.0105	0	0
Cd	0	0	1.38	0.0345	0	0
Ru	0	0	0	0	0.0294	0.0062
Ti	0	0	0	0	0	0
Zn	0	0	0	0	0	0
Total/ %:	100.03		100.01		100.03	

Table E49: Raw XRF data for the obverse of M821

Reverse

Element	Metal (248)		Brown (249)	
	Composition/ %	Error/ ± %	Composition/ %	Error/ ± %
Ag	95.2	0.2331	90.1	0.2319
Cu	2.62	0.0309	2.14	0.0293
Pd	0.742	0.0223	0.699	0.0228
Pb	0.497	0.0166	0.531	0.0178
Fe	0.739	0.033	6.31	0.0811
Au	0.169	0.0138	0.155	0.0139
Bi	0	0	0	0
Cd	0	0	0	0
Ru	0.0261	0.0061	0	0
Ti	0	0	0.0791	0.1238
Zn	0	0	0.0122	0.0064
Total/ %:	99.99		100.03	

Table E50: Raw XRF data for the reverse of M821

### Average and combined error for XRF data of M821

Average for metal areas

Element	Composition/ %	Error/ ± %
Ag	94.95	0.33
Cu	2.94	0.05
Pd	0.74	0.03
Fe	0.59	0.04
Pb	0.58	0.03
Au	0.18	0.02
Bi	0.03	0.01
Ru	0.01	0.01
Cd	0	0
Ti	0	0
Zn	0	0

Table E51: Average XRF elemental composition of metal areas on M821

Average for brown areas

Element	Composition/ %	Error/ ± %
Ag	90.05	0.33
Fe	5.29	0.11
Cu	2.42	0.04
Pd	0.72	0.03
Cd	0.69	0.04
Pb	0.58	0.03
Au	0.18	0.02
Bi	0.04	0.01
Ti	0.04	0.12
Zn	0.01	0.01
Ru	0	0

Table E52: Average XRF elemental composition of brown areas on M821

### E.17 Raw XRF data and average data for M333

#### Raw XRF data for M333

Obverse

Element	Metal (257)		Black (258)	
	Composition/ %	Error/ ± %	Composition/ %	Error/ ± %
Ag	89.4	0.2355	89.5	0.2457
Fe	6.51	0.0833	6.78	0.0885
Au	1.12	0.0276	1.11	0.0283
Cu	1.37	0.0242	1.06	0.0223
Pb	0.731	0.0205	0.625	0.0205
Pd	0.721	0.0236	0.719	0.0244
Bi	0.166	0.0116	0.162	0.0121
Zn	0	0	0.0068	0.0067
Total/%:	100.02		99.96	

Table E53: Raw XRF data for the obverse of M333

Reverse

Element	Orange (255)		Black (256)	
	Composition/ %	Error/ ± %	Composition/ %	Error/ ± %
Ag	83	0.221	81.3	0.2169
Fe	13.7	0.1158	15.3	0.12
Au	0.964	0.0257	1.05	0.0267
Cu	0.959	0.0208	1.01	0.0211
Pb	0.571	0.0191	0.618	0.0196
Pd	0.686	0.0226	0.647	0.0226
Bi	0.123	0.0111	0.141	0.0114
Zn	0	0	0	0
Total/%:	100		100.07	

Table E54: Raw XRF data for the reverse of M333

### Average and combined error for XRF data of M333

Average for black areas

Element	Composition/ %	Error/ ± %
Ag	85.40	0.30
Fe	11.04	0.15
Au	1.08	0.04
Cu	1.04	0.03
Pd	0.68	0.03
Pb	0.62	0.03
Bi	0.15	0.02
Zn	0.00	0.01

Table E55: Average XRF elemental composition of black areas on M333

## E.18 Raw XRF data and average data for V106

### Raw XRF data for V106

Obverse

Element	Metal (354)		Green (183)		Black (355)	
	Composition/ %	Error/ ± %	Composition/ %	Error/ ± %	Composition/ %	Error/ ± %
Ag	75.6	0.2205	65.90	0.1898	71.8	0.2003
Cu	20.2	0.087	28.80	0.0953	22.8	0.0868
Fe	1.79	0.0455	2.41	0.0454	3.09	0.0524
Zn	1.49	0.023	1.35	0.0208	1.23	0.0201
Pd	0.639	0.0237	0.57	0.0218	0.631	0.0221
Ni	0.209	0.0169	0.786	0.0224	0.323	0.0175
Pb	0.0754	0.0136	0.0876	0.0133	0.0671	0.0128
Ti	0	0	0.0703	0.0983	0.0202	0.1043
Sn	0	0	0.0642	0.1085	0	0
As	0	0	0.0062	0.0061	0.0064	0.0058
Total/%:	100.00		100.04		99.97	

Table E56: Raw XRF data for the obverse of V106

## Reverse

Element	Metal (359)		Green (357)		Orange tarnish (358)	
	Composition/ %	Error/ ± %	Composition/ %	Error/ ± %	Composition/ %	Error/ ± %
Ag	69.3	0.1957	64.2	0.1843	69.2	0.2051
Cu	26.2	0.0915	28.8	0.094	25.8	0.0952
Fe	1.7	0.0402	3.19	0.0495	2.49	0.0493
Zn	1.29	0.0204	1.75	0.0227	1.26	0.0212
Pd	0.671	0.0214	0.629	0.021	0.607	0.0229
Ni	0.656	0.0208	1.15	0.0249	0.535	0.0209
Mn	0.0703	0.031	0	0	0	0
Pb	0.0601	0.0125	0.0669	0.0126	0.0575	0.0132
As	0.0074	0.0058	0.0182	0.0059	0.0101	0.006
Se	0.0073	0.0038	0	0	0	0
Ti	0	0	0.202	0.0994	0	0
Ru	0	0	0.034	0.0066	0	0
Total/‰:	99.96		100.04		99.96	

Table E57: Raw XRF data for the reverse of V106

## Average and combined error for XRF data of V106

### Average for metal areas

Element	Composition/ %	Error/ ± %
Ag	72.45	0.29
Cu	23.20	0.13
Fe	1.75	0.06
Zn	1.39	0.03
Pd	0.66	0.03
Ni	0.43	0.03
Pb	0.07	0.02
Mn	0.04	0.03
As	0.00	0.01
Se	0	0
Ti	0	0
Sn	0	0
Ru	0	0

Table 6.16: Average XRF elemental composition of metal areas on V106

### Average for green areas

Element	Composition/ %	Error/ ± %
Ag	65.05	0.27
Cu	28.80	0.13
Fe	2.80	0.07
Zn	1.55	0.03
Ni	0.97	0.03
Pd	0.60	0.03
Ti	0.14	0.14
Pb	0.08	0.02
Sn	0.03	0.11
Ru	0.02	0.01
As	0.01	0.01
Mn	0	0
Se	0	0

Table 6.17: Average XRF elemental composition of green areas on V106



## Appendix F - Results pages

### F.1 Results for R294



Figure F1:  
Photograph of  
obverse of coin R294



Figure F2: OM image of  
obverse of coin R294, x30  
magnification

Element	Composition/ %	Error/ ± %
Fe	56.85	0.23
Cu	23.00	0.20
Pb	9.03	0.10
Sn	6.74	0.13
Ag	3.36	0.06
Rh	0.34	0.02
Pd	0.31	0.02
Zn	0.18	0.02
Cr	0.09	0.03
Ru	0.05	0.01
Ni	0.04	0.02
Au	0.01	0.02
Zr	0.01	0.00
Bi	0.00	0.02
Se	0.00	0.01

Table E7: Average XRF Elemental  
Composition of metal areas on R294

Element	Atomic Percentage/%
O	65.89
Fe	15.09
C	11.51
Si	2.57
Cu	2.03
P	1.73
Al	0.92
Pb	0.26

Table F1: SEM-EDS Elemental Composition of  
site 4 on area 2 of the obverse of R294

Element	Atomic Percentage/%
O	67.41
Fe	14.58
C	10.90
P	2.41
Cu	1.76
Si	1.37
Sn	0.82
Pb	0.40
Ca	0.35

Table F2: SEM-EDS Elemental Composition of  
site 2 on area 1 of the reverse of R294

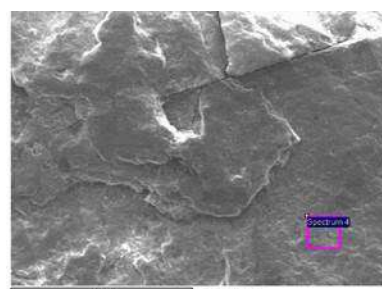


Figure F3: SEM image of site 4 on  
area 2 of the obverse of R294

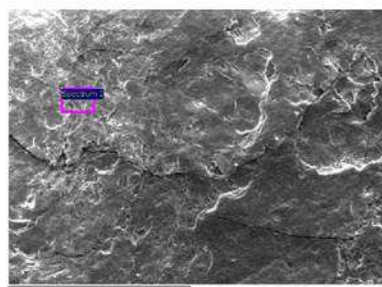


Figure F4: SEM image of site 2 on  
area 1 of the reverse of R294

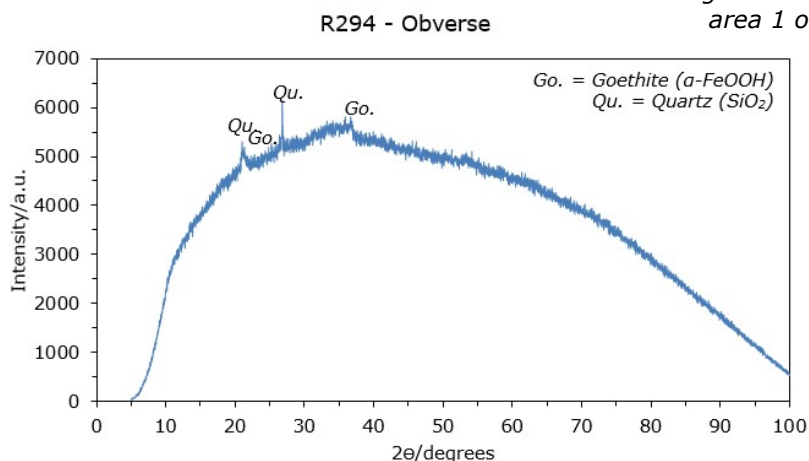


Figure F5: XRD pattern of the obverse of R294

Identification:  
Nummus, Roman era,  
AD 294–310.

Area of find:  
R294 was found in  
Lincolnshire ~1.9  
metres from the River  
Trent where there is  
documented evidence  
of Roman movement.

## F.2 Results for R253B



Figure F6:  
Photograph of  
obverse of coin  
R253B



Figure F7: OM image of  
obverse of coin R253B, x50  
magnification

Element	Atomic Percentage/%
O	68.15
C	13.46
Fe	5.38
P	3.68
Si	3.07
Al	2.58
Cu	1.59
Sn	1.40
Ca	0.69

Table F3: SEM-EDS Elemental Composition of  
site 1 on area 1 of the obverse of R253B

Element	Atomic Percentage/%
O	56.84
C	30.74
Si	3.30
P	2.25
Cu	2.14
Fe	1.49
Sn	1.40
Ca	0.88
Al	0.83
Cl	0.13

Table F4: SEM-EDS Elemental Composition of  
site 3 on area 2 of the reverse of R253B

Element	Composition/ %	Error/ ± %
Sn	43.80	0.30
Cu	28.40	0.20
Fe	24.45	0.19
Pb	1.10	0.04
Pd	0.73	0.02
Cd	0.70	0.02
Rh	0.41	0.02
Ag	0.14	0.03
Ti	0.11	0.11
Zn	0.05	0.02
As	0.04	0.01
Ni	0.02	0.01
Se	0.02	0.01
Mn	0.00	0.03

Table E12: Average XRF Elemental  
Composition of metal areas on R253B

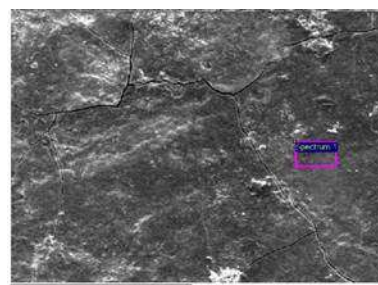


Figure F8: SEM image of site 1 on  
area 1 of the obverse of R253B

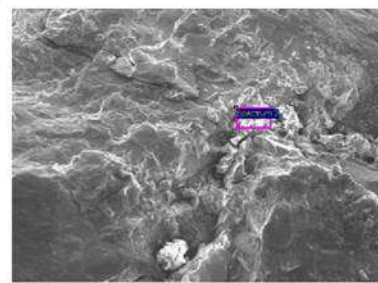


Figure F9: SEM image of site 3 on  
area 2 of the reverse of R253B

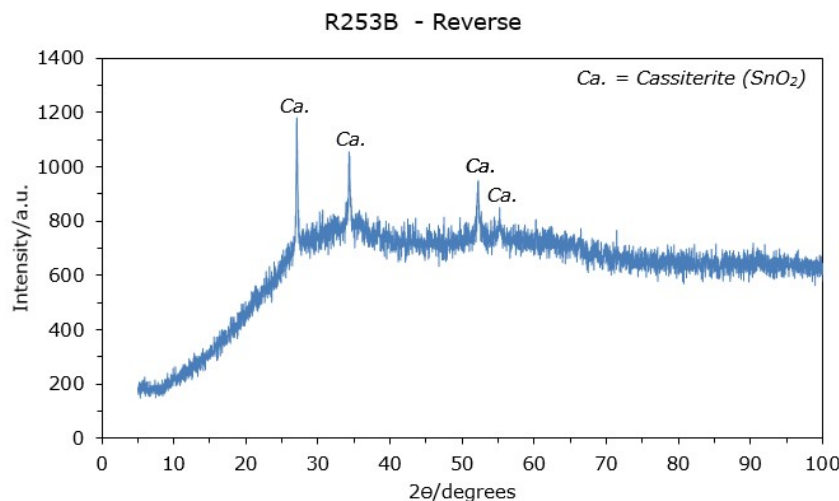


Figure F10: XRD pattern of the reverse of R253B

Identification:  
Barbarous radiate,  
Roman era, AD 275 –  
285.

Area of find:  
Found in the vicinity of  
the Fosse Way and the  
Roman town of  
Crococalana.

### F.3 Results for R03



Figure F11:  
Photograph of  
obverse of coin R03



Figure F12: OM image of  
obverse of coin R03, x30  
magnification

Element	Atomic Percentage/%
O	52.31
C	26.00
Cu	6.54
P	3.38
Sn	2.53
Si	2.30
Fe	1.94
Al	1.93
Pb	1.66
Ca	1.41

Table F5: SEM-EDS Elemental Composition of  
site 2 on area 2 of the obverse of R03

Element	Atomic Percentage/%
O	46.94
C	43.94
Cu	2.30
P	1.70
Sn	1.45
Si	0.94
Cl	0.89
Al	0.69
Ca	0.48
Fe	0.33
Pb	0.33

Table F6: SEM-EDS Elemental Composition of  
site 3 on area 2 of the obverse of R03

Element	Composition/ %	Error/ ± %
Cu	40.85	0.18
Sn	33.60	0.40
Pb	18.15	0.16
Fe	4.16	0.08
Zn	1.17	0.03
Pd	0.73	0.03
Rh	0.56	0.03
Ag	0.46	0.03
Ru	0.11	0.02
Re	0.04	0.03
Zr	0.03	0.01
Sb	0.15	0.07
Mn	0.02	0.03

Table E16: Average XRF Elemental  
Composition of green areas on R03

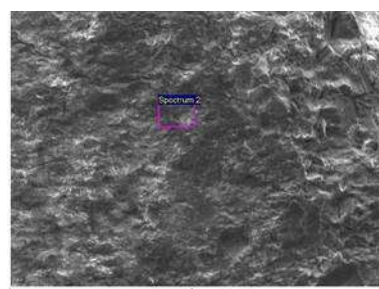


Figure F13: SEM image of site 2 on  
area 2 of the obverse of R03

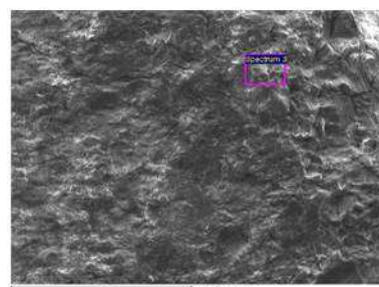


Figure F14: SEM image of site 3 on  
area 2 of the obverse of R03

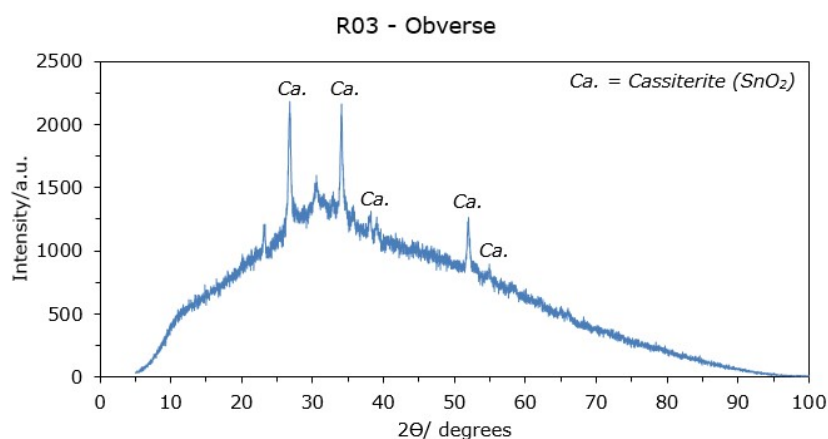


Figure F15: XRD pattern of the obverse of R03

Identification:  
Barbarous radiate,  
Roman era, AD 275 –  
285.

Area of find:  
Found in the vicinity of  
the Fosse Way and the  
Roman town of  
Crococalana.



## F.4 Results for V186



Figure F16:  
Photograph of  
obverse of V186



Figure F17: OM image of  
obverse of V186, X50  
magnification

Element	Atomic Percentage/%
O	63.11
C	21.70
Cu	4.26
Si	3.00
Fe	2.32
Sn	2.03
P	1.17
Al	1.08
Ca	0.63
Cl	0.48
S	0.23

Table F7: SEM-EDS Elemental Composition of  
site 2 on area 2 of the reverse of V186

Element	Atomic Percentage/%
O	73.83
Si	9.40
Cu	5.53
Cl	3.16
Al	3.09
Fe	2.11
P	1.17
Ca	0.68
Mg	0.65
K	0.38

Table F8: SEM-EDS Elemental Composition of  
site 3 on area 2 of the reverse of V186

Element	Composition/ %	Error/ ± %
Cu	73.53	0.27
Sn	13.47	0.24
Fe	6.85	0.09
Zn	1.92	0.05
As	1.57	0.06
Pb	1.02	0.06
Bi	0.66	0.04
Pd	0.41	0.03
Rh	0.40	0.03
Ag	0.06	0.03
Mn	0.06	0.04
Ru	0.02	0.01
Se	0.02	0.01

Table E21: Average XRF Elemental  
Composition of green/ brown areas on V186

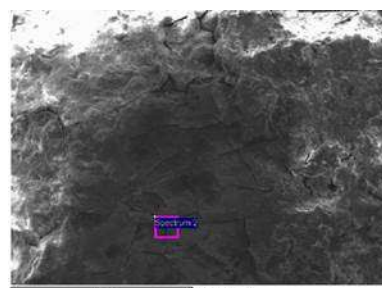


Figure F18: SEM image of site 2  
on area 2 of the reverse of V186

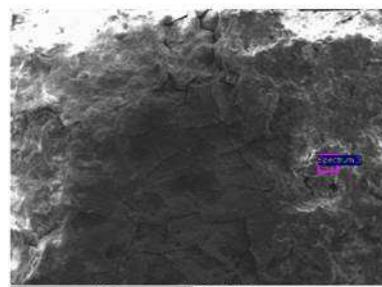


Figure F19: SEM image of site 3 on  
area 2 of the reverse of V186

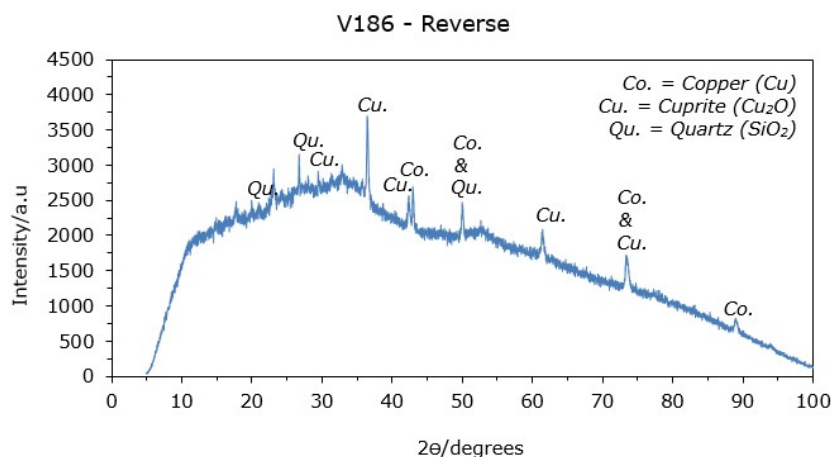


Figure F20: XRD pattern of the reverse of V186

Identification:  
Victoria Bun head  
farthing, Modern era,  
minted in 1860.

## F.5 Results for V112



Figure F21:  
Photograph of side  
A of coin V112



Figure F22: OM image of side  
A of coin V112, x50  
magnification

Element	Atomic Percentage/%
C	51.49
O	32.88
Cu	12.00
Si	1.59
P	0.87
Al	0.77
Ca	0.24
Cl	0.17

Table F9: SEM-EDS Elemental Composition of  
site 1 on area 2 of side A of V112

Element	Atomic Percentage/%
O	48.84
C	42.86
Cu	3.54
P	1.60
Fe	1.04
Si	0.66
Ca	0.48
Cl	0.31
Al	0.25
K	0.24
As	0.18

Table F10: SEM-EDS Elemental Composition of  
site 4 on area 2 of side A of V112

Element	Composition/ %	Error/ ± %
Cu	91.83	0.76
Pb	5.15	0.58
Si	1.16	0.26
Al	1.06	0.05
Fe	0.44	2.67
As	0.26	0.03
Sn	0.04	0.01
Bi	0.03	0.03
Ag	0.01	0.06
Sb	0.01	0.03
Zr	0.01	0.02
Ni	0	0

Table E24: Average XRF Elemental  
Composition of brown areas on V112

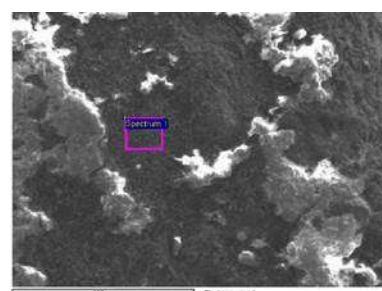


Figure F23: SEM image of site 1 on  
area 2 of side A of V112

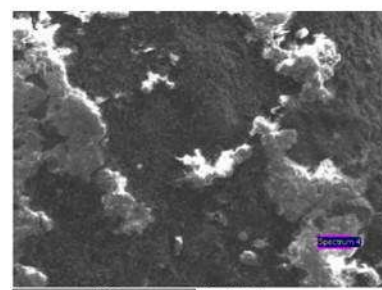


Figure F24: SEM image of site 4 on  
area 2 of side A of V112

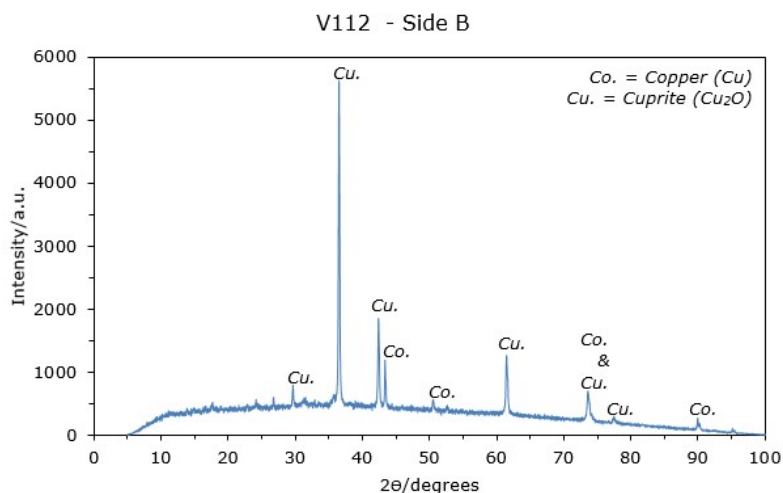


Figure F25: XRD pattern of side B of V112

Identification:  
Very severe corrosion  
almost impossible to  
identify, possible  
Victorian farthing.

Area of find:  
The majority of finds  
from this particular  
area are of Victorian  
items, and so it is  
possible to conclude  
that this find is of a  
Victorian item.

## F.6 Results for V114



Figure F26:  
Photograph of side  
A of coin V114



Figure F27: OM image of  
side A of coin V114, x50  
magnification

Element	Atomic Percentage/%
O	40.59
C	25.81
Cu	28.27
Ag	2.54
Si	1.34
Al	0.89
As	0.56

Table F11: SEM-EDS Elemental Composition of  
site 1 on area 3 of side B of V114

Element	Atomic Percentage/%
O	49.38
C	29.83
Cu	15.45
P	2.54
Si	1.27
Ca	0.85
As	0.40
Ag	0.29

Table F12: SEM-EDS Elemental Composition of  
site 2 on area 3 of side B of V114

Element	Composition/ %	Error/ ± %
Cu	93.59	0.31
Ag	2.16	0.11
Zn	1.80	0.05
As	1.28	0.05
Fe	0.32	0.03
Sn	0.30	0.06
Sb	0.07	0.04
Bi	0.03	0.02
Mn	0.01	0.01
Zr	0.01	0.01
Si	0.00	0.14

Table E27: Average XRF Elemental  
Composition of cream areas on V114

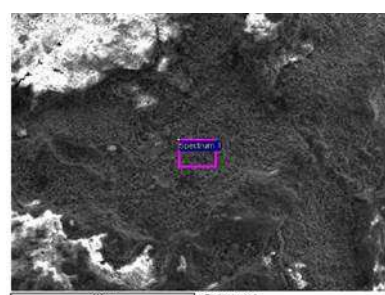


Figure F28: SEM image of site 1 on  
area 3 of side B of V114

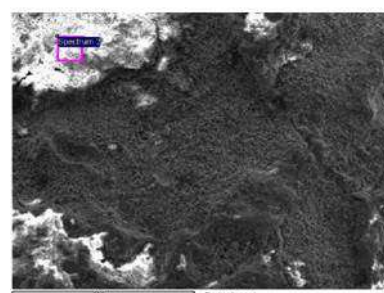


Figure F29: SEM image of site 2 on  
area 3 of side B of V114

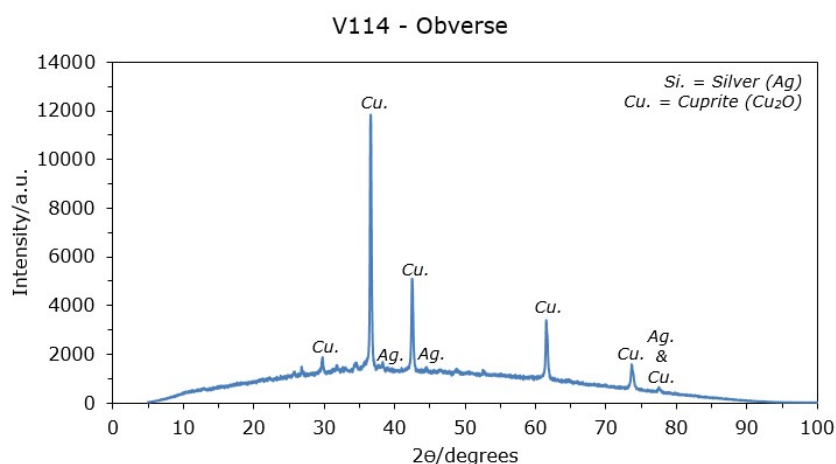


Figure F30: XRD pattern of the obverse of V114

### Identification:

The patina is so thick that no original detail present, no way to tell if this a coin or a button.

### Area of find:

The majority of finds from this particular area are of Victorian items, and so it is possible to conclude that this find is of a Victorian item.

## F.7 Results for Burial environment C

Soil	Colour	Texture
C	2.5Y 3/3	Loamy sand

Table F13: Visual analysis of soil C

pH test	Average	Error
Water	6.71	0.02
CaCl <sub>2</sub>	5.71	0.02

Table F14: pH measurements for soil C

Element	Composition/%	Error/± %
Si	70.70	1.60
Fe	15.40	0.40
Al	11.60	1.40
Ti	1.57	0.06
Zr	0.35	0.03
Cu	0.16	0.04
Cr	0.13	0.03
Zn	0.07	0.03
V	0.04	0.03
Ni	0.01	0.03

Table F15: XRF Elemental Composition of soil C

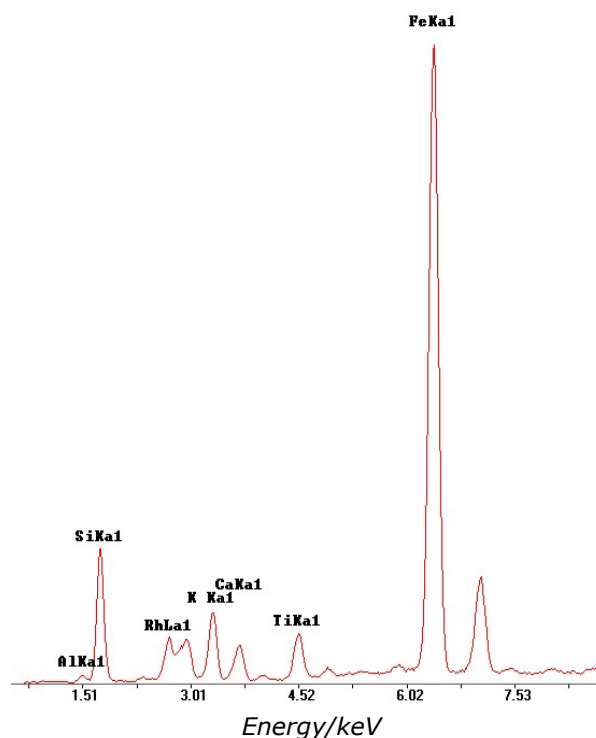


Figure F31: XRF pattern of soil C

Soil C

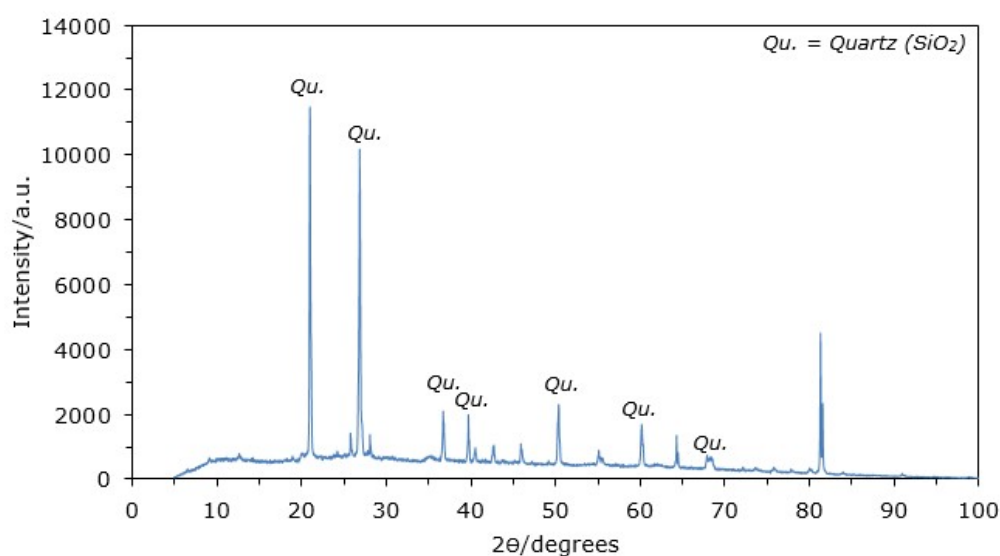


Figure F32: XRD pattern of soil C



## F.8 Results for Coin C



Figure F33:  
Photograph of  
reverse of coin C



Figure F34: OM image of  
reverse of coin C, x50  
magnification

Element	Atomic Percentage/%
C	44.75
O	42.72
Cu	4.33
Si	4.18
Al	1.19
Cl	0.88
K	0.76
Mg	0.40
Fe	0.30
Ca	0.28
Ti	0.20

Table F16: SEM-EDS Elemental Composition  
of site 2 on area 2 of the obverse of coin C

Element	Atomic Percentage/%
Cu	43.19
O	33.96
C	21.31
Si	1.53

Table F17: SEM-EDS Elemental Composition  
of site 3 on area 2 of the obverse of coin C

Element	Composition/ %	Error/ ± %
Cu	93.37	0.37
Si	4.01	3.99
Al	1.01	1.36
Bi	0.71	0.08
As	0.46	0.04
Ag	0.16	0.05
Zn	0.09	0.03
Sn	0.09	0.05
Fe	0.06	0.03
Sb	0.03	0.05
Mn	0.00	0.02
Zr	0.00	0.01

Table E32: Average XRF Elemental  
Composition of brown areas on Coin C

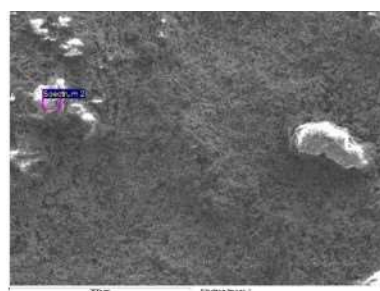


Figure F35: SEM image of site 2  
on area 2 of the obverse of coin C

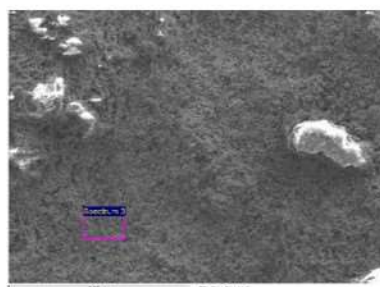


Figure F36: SEM image of site 3  
on area 2 of the obverse of coin C

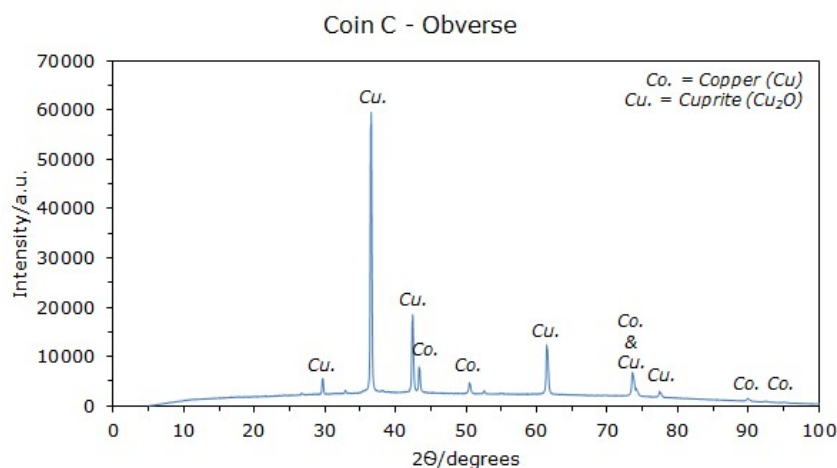


Figure F37: XRD pattern of the obverse of coin C

Identification:  
George III half penny,  
Modern era, minting  
date - 1806 or 1807.



## F.9 Results for Coin A



Figure F38:  
Photograph of  
obverse of coin A



Figure F39: OM image of obverse  
of coin A, x50 magnification

Element	Composition/ %	Error/ ± %
Ag	97.10	0.50
Pb	0.81	0.04
Pd	0.73	0.04
Cu	0.53	0.03
Fe	0.46	0.05
Au	0.19	0.03
Bi	0.19	0.02

Table E37: Average XRF Elemental  
Composition of dark grey areas on coin A

Element	Atomic Percentage/%
O	49.60
Ag	15.56
Cl	15.31
C	13.55
Si	3.89
Al	1.34
Fe	0.77

Table F18: SEM-EDS Elemental Composition of  
site 1 on area 2 of the obverse of coin A

Element	Atomic Percentage/%
O	66.56
Si	17.45
C	9.52
Ag	2.81
Cl	2.56
Al	0.79
Fe	0.30

Table F19: SEM-EDS Elemental Composition of  
site 4 on area 2 of the obverse of coin A

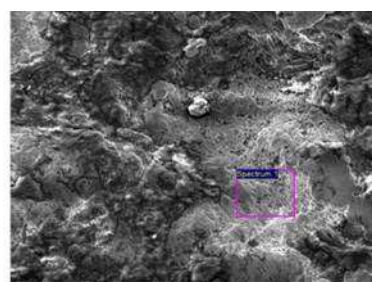


Figure F40: SEM image of site 1 on  
area 2 of the obverse of coin A

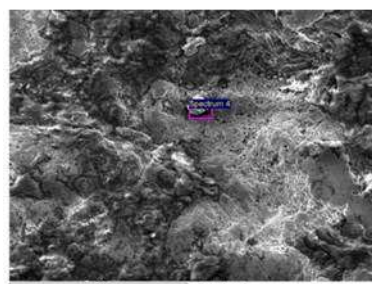


Figure F41: SEM image of site 4 on  
area 2 of the obverse of coin A

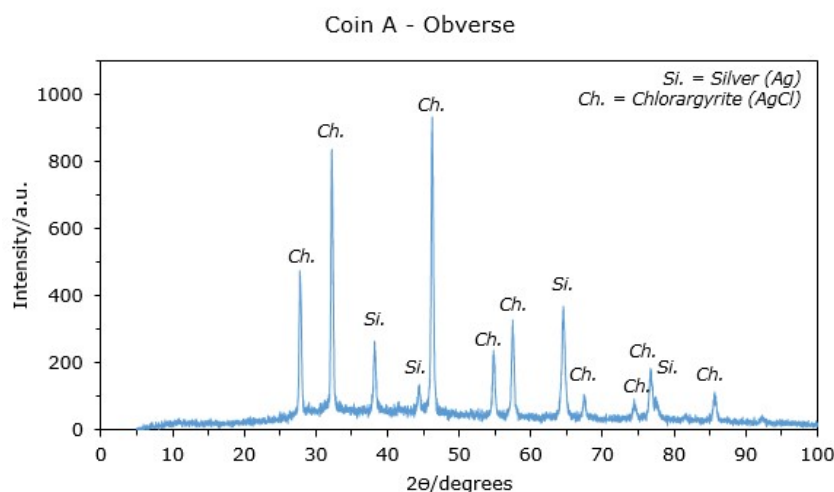


Figure F42: XRD pattern of the obverse of coin A

Identification:  
Silver denarius, Roman  
era, 212 BC and the 3<sup>rd</sup>  
century AD.

Area of find:  
Found in the vicinity of  
the Fosse Way and the  
Roman town of  
Crococalana.

## F.10 Results for M805



Figure F43:  
Photograph of  
reverse of M805



Figure F44: OM image of reverse  
of coin M805, x50 magnification

Element	Composition/ %	Error/ ± %
Ag	92.05	0.33
Fe	5.01	0.10
Cu	1.69	0.04
Pd	0.69	0.03
Pb	0.43	0.02
Au	0.09	0.02
Bi	0.05	0.01

Table E45: Average XRF Elemental  
Composition of brown areas on M805

Element	Atomic Percentage/%
O	46.11
C	33.33
Cl	7.02
Ag	6.82
Si	3.56
Al	2.18
Fe	0.59
Mg	0.38

Table F20: SEM-EDS Elemental Composition of  
site 1 on area 3 of the obverse of M805

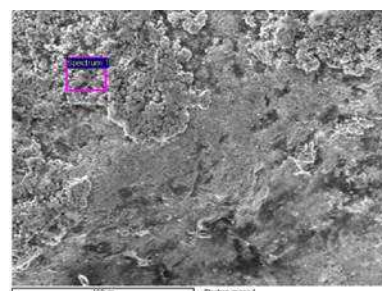


Figure F45: SEM image of site 1 on  
area 3 of the obverse of M805

Element	Atomic Percentage/%
O	60.19
Ag	22.76
C	11.30
Si	2.54
Al	1.60
Fe	1.15
S	0.46

Table F21: SEM-EDS Elemental Composition of  
site 3 on area 3 of the obverse of M805

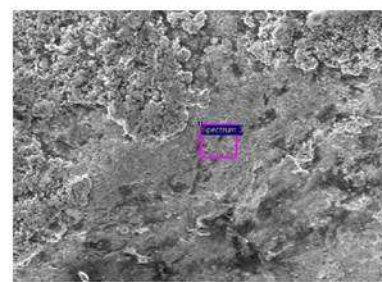


Figure F46: SEM image of site 3 on  
area 3 of the obverse of M805

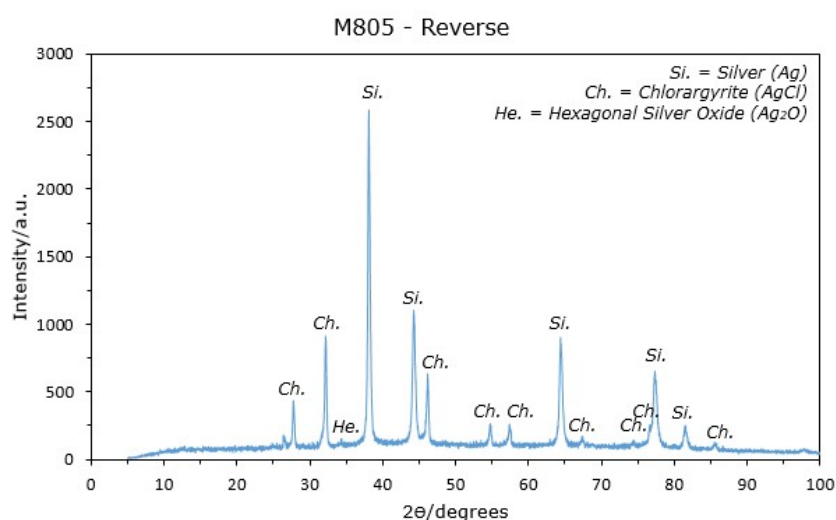


Figure F47: XRD pattern of the reverse of M805

**Identification:**  
Elizabeth I Half Groat,  
Elizabethan era,  
minted between 1558  
– 1603.

**Area of find:**  
M805 was discovered  
near to the River Trent  
and the Medieval  
village of Langford.

## F.11 Results for M804



Figure F48:  
Photograph of  
reverse of M804



Figure F49: OM image of reverse  
of coin M804, x50 magnification

Element	Composition/ %	Error/ ± %
Ag	93.80	0.35
Cu	2.23	0.04
Pb	1.52	0.04
Fe	1.35	0.06
Pd	0.74	0.03
Au	0.33	0.03
Bi	0.03	0.01

Table 7.2: Average XRF Elemental  
Composition of metal areas on M804

Element	Atomic Percentage/%
O	56.31
C	19.55
Ag	14.75
Si	2.77
Cl	2.48
Al	1.90
Fe	1.50
Mg	0.74

Table F22: SEM-EDS Elemental Composition of  
site 1 on area 3 of the obverse of M804

Element	Atomic Percentage/%
O	61.89
C	18.10
Ag	7.18
Si	4.80
Cl	3.07
Al	2.77
Fe	0.94
Mg	0.79
K	0.46

Table F23: SEM-EDS Elemental Composition of  
site 4 on area 2 of the obverse of M804

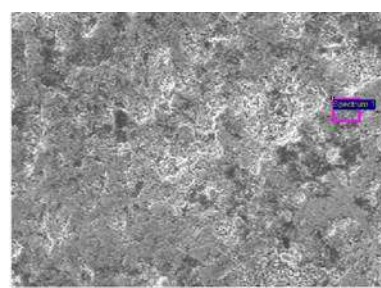


Figure F50: SEM image of site 1 on  
area 3 of the obverse of M804

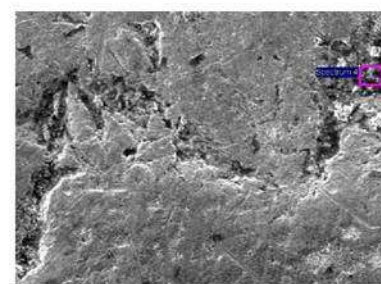


Figure F51: SEM image of site 4 on  
area 2 of the obverse of M804

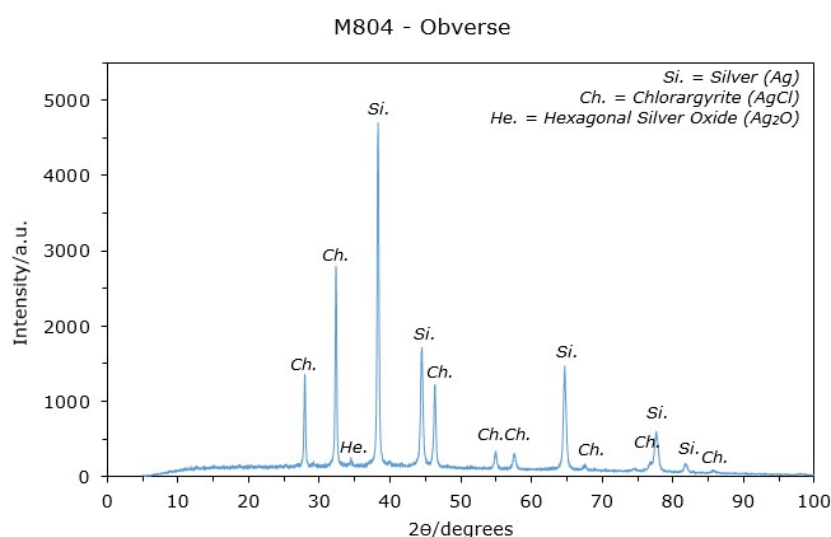


Figure F52: XRD pattern of the obverse of M804

Identification:  
Edward I penny,  
Medieval period, from  
1279 – 1327.

Area of find:  
M804 was found in  
close proximity to a  
medieval moated site  
where scattered brick  
and tiles indicated  
where a 16<sup>th</sup>/17<sup>th</sup>  
century building once  
stood that was  
preceded by a  
medieval timber  
building.



## F.12 Results for M821



Figure F53:  
Photograph of  
obverse of M821



Figure F54: OM image of  
obverse of coin M821, x50  
magnification

Element	Composition/ %	Error/ ± %
Ag	94.95	0.33
Cu	2.94	0.05
Pd	0.74	0.03
Fe	0.59	0.04
Pb	0.58	0.03
Au	0.18	0.02
Bi	0.03	0.01
Ru	0.01	0.01

Table E51: Average XRF Elemental  
Composition of metal areas on M821

Element	Atomic Percentage/%
C	34.20
O	29.49
Ag	24.14
Cl	8.23
Br	1.89
Si	1.33
Cu	0.72

Table F24: SEM-EDS Elemental Composition of  
site 1 on area 3 of the obverse of M821

Element	Atomic Percentage/%
O	30.99
Ag	25.87
C	24.96
Cl	12.84
Br	2.16
Al	1.61
Si	1.58

Table F25: SEM-EDS Elemental Composition of  
site 3 on area 3 of the obverse of M821

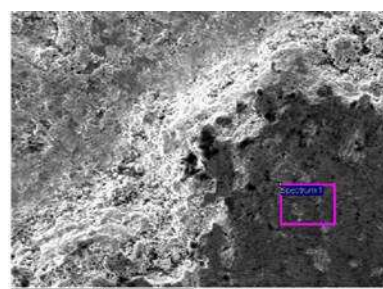


Figure F55: SEM image of site 1 on  
area 3 of the obverse of M821

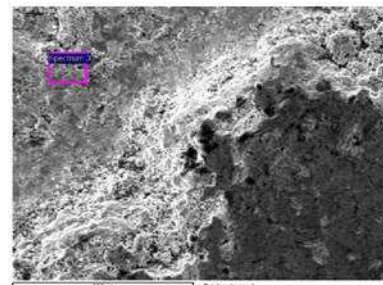


Figure F56: SEM image of site 3 on  
area 3 of the obverse of M821

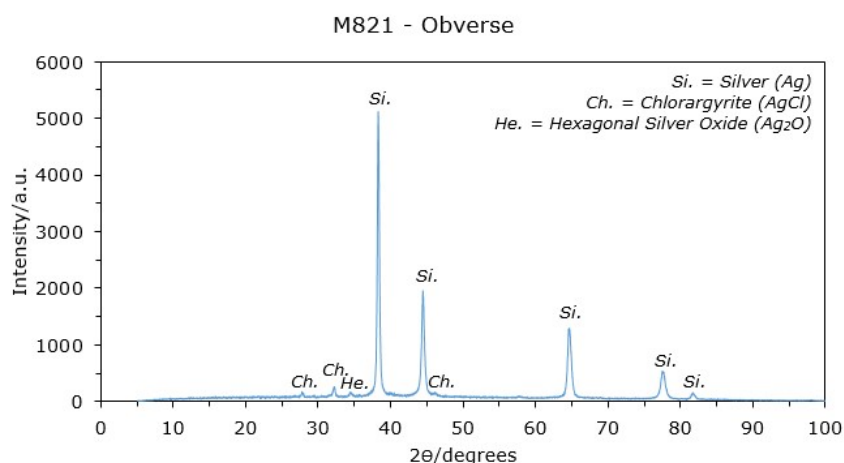


Figure F57: XRD pattern of the obverse of M821

Identification:  
Henry VII half groat,  
Medieval period, 1485  
– 1509.

Area of find:  
Found close to the  
Medieval village of  
Langford and near the  
church of St.  
Bartholomew that  
dates back to the 13<sup>th</sup>  
century.

## F.13 Results for M333



Figure F58:  
Photograph of  
reverse of M333



Figure F59: OM image of reverse  
of coin M333, x100 magnification

Element	Composition/ %	Error/ ± %
Ag	85.40	0.30
Fe	11.04	0.15
Au	1.08	0.04
Cu	1.04	0.03
Pd	0.68	0.03
Pb	0.62	0.03
Bi	0.15	0.02
Zn	0.00	0.01

Table E55: Average XRF Elemental  
Composition of black areas on M333

Element	Atomic Percentage/%
O	54.29
C	26.15
Ag	9.67
Fe	5.05
Al	1.66
Si	1.49
S	1.18
Ca	0.50

Table F26: SEM-EDS Elemental Composition of  
site 3 on area 2 of the obverse of M333

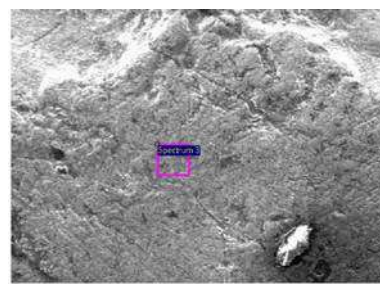


Figure F60: SEM image of site 3 on  
area 2 of the obverse of M333

Element	Atomic Percentage/%
O	50.60
C	27.91
Fe	11.26
Ag	5.90
S	1.24
Si	1.17
Al	1.10
Ca	0.82

Table F27: SEM-EDS Elemental Composition of  
site 3 on area 3 of the reverse of M333

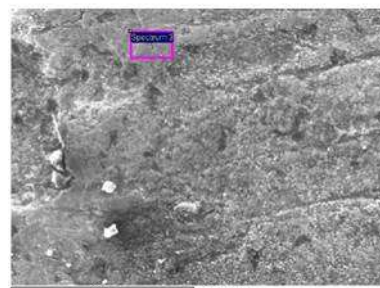


Figure F61: SEM image of site 3 on  
area 3 of the reverse of M333

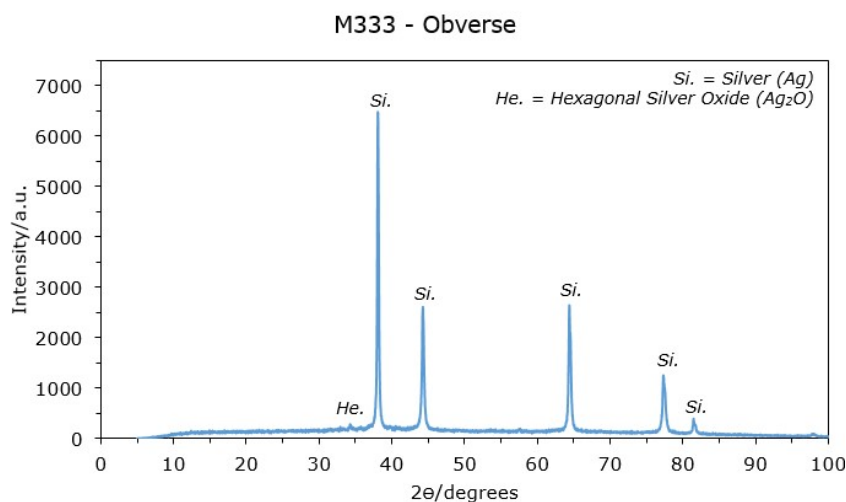


Figure F62: XRD pattern of the obverse of M333

Identification:  
Henry III voided long  
cross coin, Medieval  
period, 1247 – 1279.

Area of find:  
M333 was found  
relatively close to a  
Red lead mill, which  
originated in the 16<sup>th</sup>  
century as a lead smelt  
mill was converted to a  
red lead mill in the 17<sup>th</sup>  
century and finally a  
corn mill in the 19<sup>th</sup>  
century.